Measurements of Nonlinear Hall-Driven Reconnection in the Reversed Field Pinch

by

Timothy D. Tharp

A dissertation submitted in partial fulfillment of the

requirements for the degree of

Doctor of Philosophy

(Physics)

at the

University of Wisconsin – Madison

2010

Acknowledgements

I would like to acknowledge the many great people in my life who have made this thesis possible. This work was built on the contributions of many previous individuals, including professors, scientists, engineers, students, staff, and other helpers. Specifically, I'd like to thank Stewart Prager, John Sarff, Abdulgader Almagri, Vladimir Mirnov, Darren Craig, Matthew Miller, Caroline Ubing, and the entire MST group for their many contributions to this work.

This thesis reports the results of many iterations of the following process:

- Probe design and construction, with advice and guidance from Abdul Almagri.
- Measurement and data acquisition, with help from the many operators, hackers, engineers, and staff of MST.
- Development of the analysis method presented, with inspiration from Darren Craig, the fluctuation discussion group, and the many previous incarnations of correlation analysis techniques, recorded in the theses of J. Chapman, N. Crocker, D. Ennis, S. Choi, and others.
- Physics interpretation, with guidance from the inspiring intuition of Stewart Prager and John Sarff.
- Theory comparison, with patient explanations by Vladimir Mirnov.

Of course, I could never have made it this far without the love and support of my family. Mom and Dad, thanks for everything you have done for me these past years and the many before that. I would also like to thank my friends and family of Madison, specifically Rich Magee, Dan Clayton, Josh Reusch, Hillary Stephens, and Matt Miller, for being such great co-workers and friends.

Finally, to Karen: You have stuck with me since nearly day one of graduate school, and have made my life wonderful. Thanks for everything.

Contents

Chapter 1: Introduction

From astrophysics to nuclear physics, from the Earth's magnetic field to its polar aurorae, plasma science has changed the way we think of our universe. In addition to their scientific interest, plasmas have many technological applications such as semiconductor processing, medical product sterilization, hazardous waste removal, energy efficient light bulbs, and television screens [1]. One application, however, has eluded scientists for decades: the net generation of useful energy from controlled thermonuclear fusion. Often viewed as the only viable very-long-term energy solution for the human race, more scientific research into the nature of plasmas, material science, and reactor engineering is necessary before this application will contribute to the energy portfolio powering our world.

This thesis investigates measurements of natural plasma relaxation events in a laboratory fusion experiment. Though the experiment was designed to study the plasma physics associated with a specific controlled fusion concept, the physics exhibited offers a unique opportunity to study concepts and phenomena that are applicable to many plasmas, including naturally occuring astrophysical plasmas. One such phenomenon, magnetic reconnection, is a ubiquitous plasma process which is viewed by some as a bane to fusion science because the associated magnetic fluctuations reduce confinement properties, and in some cases reconnection will even cause a catastrophic plasma termination event. In reversed field pinch plasmas, reconnection occurs in the form of sawtooth oscillations—periodic events that rarely disrupt the plasma but rather seem determined to flaunt the configuration's global stability. Moreover, these reconnection events are an efficient ion heating mechanism, pouring a significant fraction of the energy released by magnetic field annihilation directly into the ion temperature. An understanding of reconnection dynamics may therefore lead fusion scientists to view this process as a tool for fusion rather than a hindrance: reconnection may someday turn out to be a fundamental ingredient to achieving economically viable fusion energy.

Regardless of the subject's terrestrial applications, the process of reconnection is a beautiful natural phenomenon that occurs all around us. On the surface of our Sun, solar flares have been identified as reconnection events that fling plasma far into space. In front of our planet (on the day side), the Earth's magnetic field protects us from the solar wind by deflecting plasma particles near a

steady state reconnection site known as the magnetopause. Behind us (on the night side), the Earth's magnetotail also undergoes magnetic reconnection, but in an impulsive manner which periodically accelerates plasma particles toward the poles of the earth, resulting in the polar aurorae. Everywhere we look, it seems, we can find a plasma. And in nearly every plasma we examine, we can find the process known as reconnection.

Whenever a process is found in such a variety of places, we expect it to exhibit itself in a variety of ways. Not surprisingly, there are a large number of theoretical models for reconnection which may or may not be applicable to any given situation. As such, it is the goal of this thesis to advance the understanding of the reconnection within our experiment, and to report measurements which will contribute to a better understanding of reconnection in general.

1.1 Background

The concept of magnetic reconnection–the often violent process by which magnetic fields are topologically rearranged into a new magnetic geometry–was first introduced in 1946 by R. G. Giovanelli to explain solar flares in the sun's chromosphere, which were observed to coincide with areas of high magnetic field known as sunspots [2]. Since then, reconnection has been identified in a variety of astrophysical and laboratory plasmas, and is thought to be a common, if not ubiquitous, ingredient in plasma dynamics. Sweet [4] and Parker [5] offered the first quantitative description of this process to explain astrophysical observations. Many theoretical variations have been proposed to describe reconnection more accurately, particularly focusing on the explanation of fast and impulsive reconnection. Models which treat the electron fluid and ion fluid independently allow for the inclusion of the Hall term in the applicable Ohm's law [3] and are a particularly promising way to explain the observed rates of fast reconnection. Models which result in impulsive reconnection typically invoke nonlinear or three-dimensional effects [6].

Reconnection appears in nature and in laboratory plasmas in two general forms: driven and spontaneous. Driven reconnection occurs only because of external forcing, whereas spontaneous reconnection results from the development of a local instability which allows the plasma to reach a lower energy state [3]. A classic form of spontaneous reconnection, known as a tearing instability, will

occur in a toroidal plasma when two conditions are met: First, if the geometry permits a quantized wave vector with no parallel component ($\vec{k}\cdot\vec{B}=0$), the mode will be resonant. Commonly, a toroidal plasma is approximated by a periodic cylinder. In such a system, the resonance condition can be written in terms of the safety factor, $q=\frac{rB_\phi}{RB_\theta}$, of the plasma. Any surface on which the safety factor is a rational number, $q=\frac{m}{n}$, a tearing mode with wave vector $\vec{k}=\frac{m}{r}\hat{\theta}-\frac{n}{R}\hat{\phi}$ is resonant. Second, depending on the details of the plasma equilibrium, the mode may also be unstable [7]. In particular, instability can be induced by a strong gradient in the plasma current density such that the associated gradient length scale is shorter then k^{-1} [3]. If the mode is both resonant and unstable it is called a spontaneous tearing mode.

The reversed field pinch (RFP) [8], depicted in Figure 1.1, is a toroidal plasma equilibrium configuration with strong magnetic shear which is particularly prone to the development of tearing modes. Typically, an RFP displays a periodic sawtooth cycle which is characterized by a slow peaking of the current profile followed by a sudden, global plasma relaxation event. It has been previously shown that during these sawtooth events multiple reconnecting Fourier modes develop: core modes are predicted to be linearly unstable and measured to be spontaneous, while edge modes are linearly stable and have been inferred to develop from nonlinear drive [9] [10].

The Madison Symmetric Torus (MST) [11] is an RFP at the University of Wisconsin-Madison. Figure 1.2 lists typical machine parameters used for this work, though MST is capable of running in many modes of operation and with a wide range of plasma parameters. A typical safety factor profile for MST has $q\sim 0.2$ on axis and negative in the edge, as seen in Figure 1.3.

1.2 Overview of the Thesis Results

This thesis reports detailed magnetic field measurements of the reconnection associated with the $n=1$ Fourier mode in the edge of MST. The goal of this work was initially to investigate the presence or absence of Hall effects with regard to the reconnection in the edge. The plasma parameters of MST indicate that this is a collisionless plasma, in which we expect to see significant Hall physics associated with the reconnection on scales below the ion inertial length, $c/\omega_{pi}\approx 8$cm. Previously, the Hall dynamo was observed to contribute significantly to the mean-field Ohm's law in both the core [12]

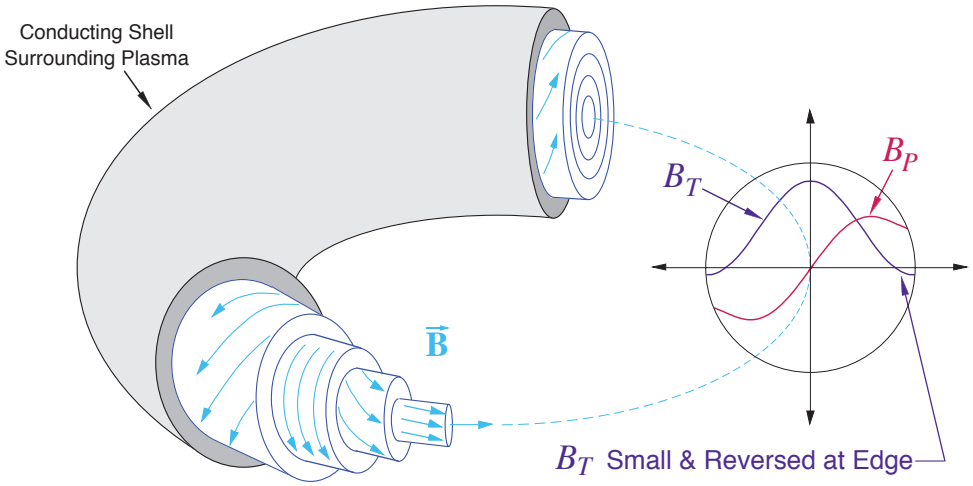

Figure 1.1: Depiction of the magnetic field configuration of the Reversed Field Pinch.

Quantity	Symbol	Value
Major Radius	R	1.5 m
Minor Radius	a	0.52 m
Electron Density	n_e	1×10^{19} cm^{-3}
Plasma Current	I_p	225 kA

Figure 1.2: Machine and plasma parameters for typical MST plasmas in this study.

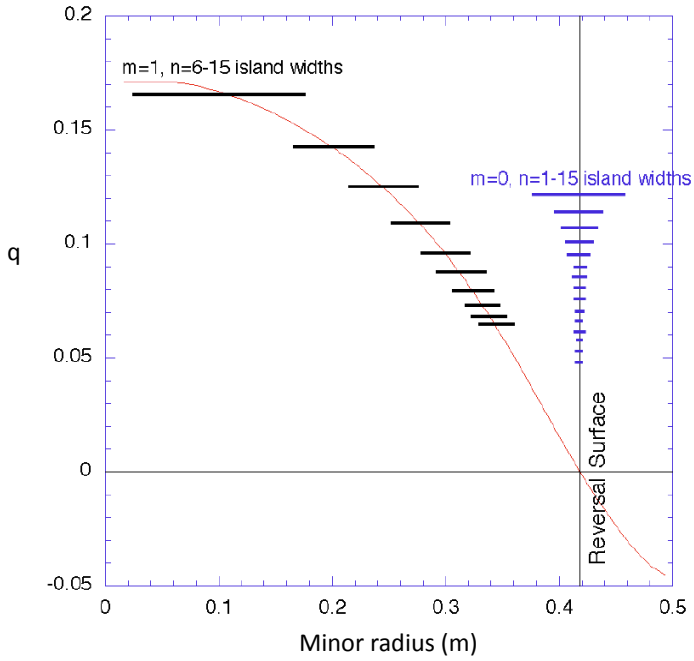

Figure 1.3: A typical q-profile for MST. Locations of resonant modes and their typical saturated island widths are indicated.

and edge [13] of MST. Here, we study the Ohm's law governing fluctuations by measuring the terms which which are accessible through an assortment of magnetic diagnostics. We find that the Hall term is indeed large compared to both the electric field and the resistive term ($\frac{1}{ne}J \times B >> E > \eta J$), indicating that two fluid effects are important in the physics governing this reconnection.

The large-scale radial structure of the reconnection magnetic field is found to agree with resistive magnetohydrodynamic (MHD) tearing mode calculations. Although the large-scale radial structure agrees with MHD, the dynamics of the reconnection layer and drive do not. Understanding the role of Hall physics in Ohm's law at the reconnection X-point requires an understanding of nonlinear mode coupling physics.

The study of the nonlinear physics of tearing modes in the RFP has a rich history in Madison as well as in the broader community. Nonlinear physics which couples plasma fluctuations to the plasma equilibrium has been studied in great detail [14]: the RFP equilibrium would not be possible without the MHD dynamo, a process by which fluctuations modify the mean field of the plasma [15], and experimental modification of the plasma equilibrium has been used to directly reduce the level of plasma fluctuations [16]. Investigation of fluctuation induced transport of heat, particles, momentum, and energy highlights the variety of effects these nonlinear processes can cause (see, e.g., [17] [18]). Nonlinear three-wave coupling has also been previously studied [9]. A cascade of three-wave couplings (or higher order correlations) has been identified as a primary mechanism for the development of small scale turbulent fluctuations: when $m = 0$ modes are removed from the plasma, large scale three-wave interactions are reduced and the consequences can be observed in the reduced fluctuation levels at all scales.

The term "Hall reconnection" is usually used to describe a scenario in which a reconnection process can achieve faster reconnection rates by the inclusion of the Hall term in the relevant Ohm's law. It has been previously observed that these two fluid effects, rather than the mechanism which decouples the electrons from the magnetic field and allows the frozen flux condition to be broken, are the primary feature necessary to achieve fast reconnection [19]. This Hall effect modifies the outflow region of the reconnection, which in our case is toroidally displaced from the X-point, but provides zero contribution to the parallel (out-of-plane with respect to the reconnection field) Ohm's law at

the reconnection X-point. In contrast, the plasmas observed in this work exhibit reconnection with a nonlinear Hall term measured directly at the reconnection X-point. This contribution to Ohm's law is large compared to the relevant electric field and ηJ, and we conclude that this reconnection is driven by the nonlinear two-fluid Hall term. Therefore, we adopt the phrase "Hall-driven reconnection" to describe our observations. This does not imply that the more conventional roles of Hall reconnection are not at play, but they are difficult to interpret in the RFP using present methods. In other experiments, Hall reconnection effects have been indirectly observed by measuring the signature "quadrupole field" that is present between the ion and electron dynamic scales [20], but in the RFP this effect is reduced by the presence of a strong guide field and a strong current gradient across the asymmetric reconnection layer.

We measure that the nonlinear Hall term provides significant drive for the $n = 1$ edge mode reconnection, and the strongest contributions come from three-wave coupling to unstable modes which are resonant elsewhere in the plasma. Three wave effects have been previously reported in MST plasmas [21], and have been inferred to drive edge mode reconnection [10], though the mechanism was previously unidentified. Here, we observe one mechanism through which these couplings come into play in the physics of edge mode reconnection. We conclude that spontaneous $n = 6-8$ tearing modes, developing in the core of the plasma, provide the "external" forcing necessary to drive this stable but resonant edge mode. The measured forcing is produced through nonlinear coupling of the modes in the form of three wave interactions mediated by the Hall term of Ohm's law. This observation is seemingly at odds with reconnection intuition because it is well known that a Hall term cannot break the frozen flux theorem, and therefore isn't expected to contribute to Ohm's law at the X-point of reconnection. However, like the $v \times B$ terms in resistive MHD simulations of the RFP, our plasma manages to get around this issue, perhaps because of the nonlinear coupling of $m = 0$ edge mode effects. At the reversal surface, the magnetic island fieldline structure is significantly distorted by the presence of $n = 2 - 4$ modes. This distortion may allow $n = 1$ flux to freely move about in ways that frozen flux conditions would otherwise prohibit in a linear model.

This research highlights the need to understand toroidal effects, Hall physics, and nonlinear interactions in order to understand the reconnection processes of the RFP.

1.3 Coordinate systems

There are two commonly used coordinate systems on MST. The first, illustrated in Figure 1.4, is used for physics applications, and is right handed in the coordinates $\hat{r}, \hat{\theta}, \hat{\phi}$. Notice that θ is measured from the inboard edge, starting in the upward direction.

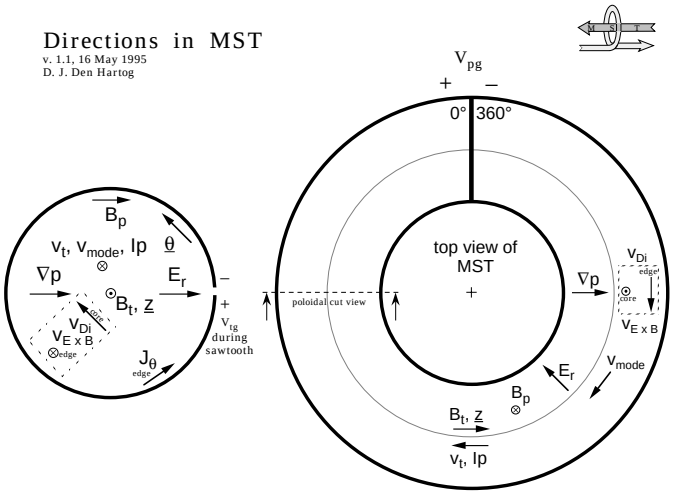

Figure 1.4: The right handed coordinate system used for most of this thesis.

The second commonly used coordinate system is identical to the system above except the $\hat{\theta}$ direction is reversed, with θ measured from the outboard edge, starting in the upward direction. The left handed coordinate system was used to create the MST porthole map, and is currently used to identify the location of hardware on MST.

In this thesis, I will refer to these as the "right-handed coordinate system" and the "left-handed coordinate system" respectively. If no coordinate system is indicated, the right-handed coordinate system is assumed.

1.4 References

[1] C. Suplee, *The Plasma Universe*. Cambridge University Press, 2009.

[2] R. G. Giovanelli, "A theory of chromospheric flares," *Nature*, vol. 158, pp. 81–82, July 1946.

[3] E. G. Zweibel and M. Yamada, "Magnetic reconnection in astrophysical and laboratory plasmas," *Annu. Rev. Astron. and Astrophys.*, vol. 47, pp. 291–332, 2009.

[4] P. Sweet, "Electromagnetic phenomena in cosmical physics," *International Astronomical Union Symposium*, vol. 6, 1958.

[5] E. N. Parker, "Sweet's mechanism for merging magnetic fields in conducting fluids," *J. Geophys. Res.*, vol. 62, pp. 509–520, December 1957.

[6] A. Bhattacharjee, "Impulsive magnetic reconnection in the earth's magnetotail and solar corona," *Annu. Rev. Astron. and Astrophys.*, vol. 42, pp. 365–384, 2004.

[7] H. Furth, J. Killeen, and M. Rosenbluth, "Finite resistivity instabilities of a sheet pinch," *The Physics of Fluids*, vol. 6, pp. 459–484, April 1963.

[8] H. A. B. Bodin and A. A. Newton, "Reversed-field-pinch research," *Nuclear Fusion*, vol. 20, no. 10, pp. 1255–1324, 1980.

[9] Y. L. Ho and G. G. Craddock, "Nonlinear dynamics of field maintenance and quasiperiodic relaxation in reversed-field pinches," *Physics of Fluids B: Plasma Physics*, vol. 3, no. 3, pp. 721–734, 1991.

[10] S.-H. Choi, D. Craig, F. Ebrahimi, and S. C. Prager, "Cause of sudden magnetic reconnection in a laboratory plasma," *Phys. Rev. Lett.*, vol. 96, no. 145004, 2006.

[11] R. N. Dexter, D. W. Kerst, T. W. Lovell, and S. C. Prager, "The madison symmetric torus," *Fusion Technology*, vol. 19, pp. 131–139, January 1991.

[12] W. Ding, D. L. Brower, D. Craig, B. Deng, G. Fiksel, V. Mirnov, S. C. Prager, J. S. Sarff, and V. Svidzinski, "Measurement of the hall dynamo effect during magnetic reconnection in a high-temperature plasma," *Phys. Rev. Lett.*, vol. 93, p. 045002, July 2004.

[13] A. Kuritsyn, G. Fiksel, A. Almagri, S. Prager, J. S. Sarff, and T. Tharp, "Measurements of the hall dynamo in the reversed field pinch edge during reconnection events," *16th IEEE International Pulsed Power Conference*, vol. 1, pp. 20–23, 2007.

[14] S. Ortolani and D. D. Schnack, *Magnetohydrodynamics of Plasma Relaxation.* World Scientific, Singapore, 1993.

[15] R. G. Watt and R. A. Nebel, "Sawteeth, magnetic disturbances, and magnetic flux regeneration in the reversed-field pinch," *Phys. Fluids*, vol. 26, pp. 1168–1170, May 1983.

[16] J. Sarff *et al.*, "Transport reduction by current profile control in the reversed-field pinch," *Phys. Plasmas*, vol. 2, pp. 2440–2446, June 1995.

[17] F. Ebrahimi, V. Mirnov, and S. Prager, "Momentum transport from tearing modes with shear flow," *Phys. Plasmas*, no. 15, p. 055701, 2008.

[18] G. Serianni, A. Murari, G. Fiksel, V. Antoni, M. Bagatin, D. Desideri, E. Martines, and L. Tramontin, "Magnetic fluctuations and energy transport in rfx," *Plasma Phys. Control. Fusion*, no. 43, pp. 919–927, 2001.

[19] J. Birn, J. Drake, M. A. Shay, B. N. Rogers, R. E. Denton, M. Hesse, M. Kuznetsova, Z. Ma, A. Bhattacharjee, A. Otto, and P. Pritchett, "Gem magnetic reconnection challenge," *Journal of Geophysical Research*, vol. 106, pp. 3737–3750, March 2001.

[20] Y. Ren, M. Yamada, S. Gerhardt, H. Ji, R. Kulsrud, and A. Kuritsyn, "Experimental verification of the hall effect during magnetic reconnection in a laboratory plasma," *Phys. Rev. Lett.*, no. 95, p. 055003, 2005.

[21] J. S. Sarff, "Nonlinear coupling of tearing fluctuations in the madison symmetric torus," *Phys. Fluids B*, vol. 5, no. 2540, 1993.

Chapter 2: Magnetic Probes

2.1 Probe Design

One of the simplest, most robust, and most useful diagnostics on MST, or any plasma physics experiment, is the magnetic pickup coil. Nearly every measurement in this thesis was performed using magnetic "b-dot" pickup coils embedded in an insertable probe. These take advantage of magnetic induction to reproduce reliable measurements of magnetic field [1].

Each probe consists of wire wrapped around a boron nitride core, which is placed in a precisely machined boron nitride housing to control relative alignment. The housing is covered with a conducting silver paint to prevent electrostatic pickup, and the entire probe is encased in a boron nitride protective particle shield. Boron nitride is a ceramic with good thermal shock properties, and has proven to be a robust material in the harsh environment of MST plasmas. Additionally, this material is easy to machine (it has a consistency similar to chalk), safe to handle, and vacuum compatible.

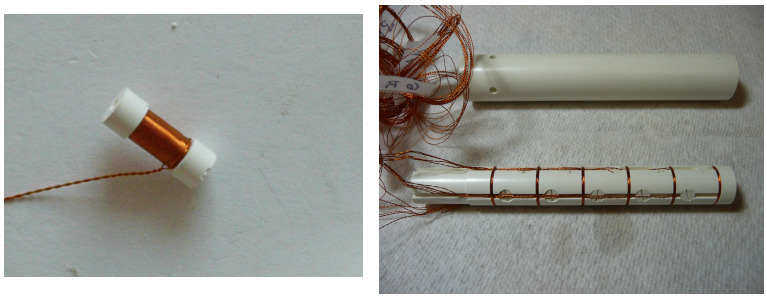

Figure 2.1: Insertable magnetic probe. This probe consists of 16 coils: 5 for B_ϕ, 5 for B_θ, and 6 coils wound directly on the probe housing to measure B_r.

The induced voltage on the wire (which is proportional to $\partial B/\partial t$) is integrated using a low-drift active analog integrator, and recorded using a commercial digitizer. In this study, we have used a digitization rate of 20 kHz. The probe coils are approximately 1 cm long, with an effective area (number of turns times the average area of a single turn) of about 10 cm^2, as measured using the method of Appendix C.1.

2.2 Probe Calibration

Probe calibration is accomplished in two steps: The probe's effective area is measured on the bench (see Appendix C.1), then *in situ* measurements are used to orthogonalize the alignment of the coils before each run (see Appendix C.2).

We can do a similar correction to orthogonalize the radial coil; however, even with this correction the radial coil signal will usually be significantly contaminated by poloidal field. The probe cannot always be pointed in a direction perpendicular to the equilibrium flux surface of the plasma– even the location of the magnetic axis will shift significantly during a sawtooth crash, so it is difficult to make a measurement that is even approximately a purely radial field. Instead we subtract from the radial coil's signal a time-dependent fraction of the poloidal field. The fraction of poloidal pickup is determined by requiring that the ensemble-averaged ($n = 0$ component) radial field is zero, a condition which must be true at each time point as a direct consequence of $\nabla \cdot \vec{B} = 0$.

2.3 Probe Perturbations

The presence of a probe will, of course, perturb the plasma. In particular, the probe blocks the flow of plasma current, diverting this current around the edges of the probe. A very simple model treats this diverted current as a pair of wires, diverting a total current of JA where J is the plasma current density and A is the effective surface area of the probe as seen from the $\hat{J}$ direction. The magnetic field perturbation inside the cylindrical probe resulting from this diverted current can be calculated from this wire model, depicted in Figure 2.2. Interestingly, if we use a model consisting of two sheets of current diverted symmetrically around an infinite cylinder, the resulting internal field is zero [2]; a more appropriate model may be something between wire-like currents and sheet-like currents such as a half-infinite cylinder.

This wire current model results in a spatially dependent radial field

$$B_r(x=0) = \frac{\mu_0 I_0/2}{2\pi}\left(\frac{1}{R-y} - \frac{1}{R+y}\right)$$

where R is the radius of the probe, and I_0 is the total current interrupted by the probe body. This can

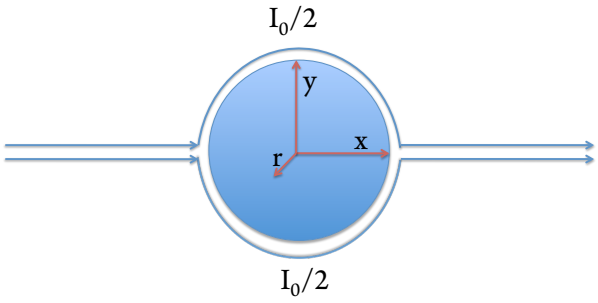

Figure 2.2: Simple model of a probe perturbation.

be used to calculate appropriate tolerances for radial coil magnetic probe design. A coil of diameter d offset from center by a distance δ inside a probe of radius R will measure a perturbation field

$$B_r = \frac{\mu_0 I_0/2}{2\pi d} \ln\left(\frac{R^2 - (\frac{d}{2} + \delta)^2}{R^2 - (\frac{d}{2} - \delta)^2}\right).$$

In the final measurement iteration, we designed a probe with tolerances tight enough to measure the expected 2-5 Gauss non-perturbed fluctuation field, but the specifications of the probe were not sufficient to detect the actual magnetic field of the $n = 1$ mode on the outboard edge, which turned out to have a strength of only 0.5 Gauss. Because of this, we will use $\nabla \cdot B = 0$ to determine B_r for this thesis. The lower than expected magnetic field strength has been accounted for by stronger than previously expected toroidal effects.

The model shown here is nearly consistent with measurements taken using radial coils that were deliberately placed off-center within a probe body. Off center coils may be used in the future, together with a more sophisticated model, as a new method to measure plasma current. (Currently a mapping of the full magnetic field structure, as done in this thesis, or the use of a more complex Rogowskii probe is required to measure currents in MST).

2.4 References

[1] I. H. Hutchinson, *Principles of Plasma Diagnostics*. Cambridge University Press, 2 ed., 2002.

[2] J. D. Jackson, *Classical Electrodynamics*. John Wiley and Sons Inc, 3 ed., 1999.

Chapter 3: Pseudospectrum

A significant part of my thesis project was the development and implementation of the correlation analysis of fluctuations. Correlation analyses have been done before by many previous graduate students and scientists on MST, yet nearly each instance of this was done in a different manner, often with surprisingly little documentation on the individual method used or how it could be related to previous work. For this reason, I have dedicated a fairly long Chapter to what I call pseudospectral analysis. For the reader interested only in adapting this method to his or her own measurements, a User's Guide to Pseudospectra can be found in Appendix A.

Fluctuations are defined to be non-axisymmetric plasma perturbations. Therefore, it is natural to use a spatial Fourier basis set to describe the fluctuations of a toroidal plasma. Here, the Fourier decomposition is developed for a periodic cylinder. In a true torus, poloidal mode numbers are not "good" quantum numbers, requiring modification of the periodic cylinder treatment which will be discussed in Chapter 4. For the remainder of this Chapter, MST is presumed to be a periodic cylinder with good quantum numbers in both symmetry directions.

Here, we develop a method to extract the mode spectrum of a given signal. Typically, one must have $2n_{\max} \times 2m_{\max}$ measurements in order to resolve mode numbers $n_{\max}$ and $m_{\max}$. However, using this method one can resolve the n and m spectrum of a single point measurement. This is done by correlating the measurement with the toroidal array of magnetic pickup coils, using a mathematical technique that I call pseudospectral analysis.

3.1 Spatial Fourier Decomposition in MST

MST is treated as a periodic cylinder, so that any signal, X, that is measured everywhere in the plasma can be decomposed by a 2-D fourier transform:

$$X(\theta,\phi) \quad = \quad \sum_m \sum_n a_{mn} \cos(m\theta + n\phi - \delta_{mn})$$

Here, θ and ϕ are defined (as usual) to be the poloidal and toroidal angles, respectively. The

third spatial coordinate is implied: X, a_{mn}, and δ_{mn} are all functions of radius, r. Therefore, pseudospectral analysis must be performed on each flux surface (surface of constant r) of the equilibrium separately.

For the rest of this Chapter, a capital letter (such as X above) represents something that is a function of θ and ϕ. Lowercase letters are constants in space (but may vary from shot to shot).

The first step to simplify the analysis is to reduce the m-spectrum. MST is most sensitive to $(m = 0, n = 1 - 4)$ and $(m = 1, n = 5 - 8)$ modes. So, we will assume that if we find the n-spectrum of our signal, we know the m-spectrum as well. For example, if we have an $n = 6$ mode, we can be pretty certain it is $m = 1$, and similarly for other modes. (If this were not the case, we could still take a pseudospectrum, but we would need a poloidal array of magnetic pickup coils in addition to the toroidal array.) This is discussed in more detail in section 3.7.

Just to reiterate, $m = (0 \text{ or } 1)$ is treated a function of n, so we can drop the m subscript on our coefficients. We rewrite X as

$$X(\theta, \phi) = \sum_{n=0}^{\infty} a_n \cos(m\theta + n\phi - \delta_n) \tag{3.1.1}$$

Complex notation can be employed to make the math easier to follow. However, we want to be explicit about our notation so there is no confusion about how to interpret the final expressions (i.e. Do I take the real part in the end? What does the imaginary part mean?). To avoid this confusion, we will require that X be a real number. This is achieved by expanding X in terms of a complex number plus its complex conjugate.

$$X(\theta, \phi) = \frac{x_0}{2} + \sum_{n=1}^{\infty} \frac{1}{2} \left(x_n e^{i(m\theta + n\phi)} + x_n^* e^{-i(m\theta + n\phi)} \right)$$

Notation can be greatly simplified by defining $x_{-n} \equiv x_n^*$, and $m(-n) = -m(n)$, so that

$$X(\theta, \phi) = \frac{1}{2} \sum_{n=-\infty}^{\infty} x_n e^{i(m\theta + n\phi)}. \tag{3.1.2}$$

Note that these expressions are a mathematical description of a mode's spatial variation at

a given time point. In this presentation, *the sign of n is not related to the rotation direction of the nth mode.* Also note that, since m is a function of n, we are not considering the possibility of the coexistence of (m, n) and $(-m, n)$ modes.

A third equivalent representation is given by

$$X = \sum_{n=0}^{\infty} \alpha_n \cos(n\phi) + \beta_n \sin(n\phi). \tag{3.1.3}$$

This presentation (3.1.3) is used in the MST data acquisition routines, then converted into amplitude and phase notation (3.1.1) for storage in the MST database. This thesis will be working primarily with the complex notation (3.1.2), because it is more convenient for derivations. A fourth presentation can be found by explicitly splitting the complex number x_n into its amplitude and phase, $x_n = |x_n| e^{i\delta_{x_n}}$. Conversion between these four presentations is summarized in Figure 3.1.

Presentation	Amplitude	Phase	α	β	Eq.
$a_n \cos(n\phi - \delta_n)$	a_n	δ_n	$a_n \cos(\delta_n)$	$-a_n \sin(\delta_n)$	a_0
$\alpha_n \cos(n\phi) + \beta_n \sin(n\phi)$	$\sqrt{\alpha_n^2 + \beta_n^2}$	$\tan^{-1}\left(\frac{\beta_n}{\alpha_n}\right)$	α_n	β_n	α_0
$\frac{1}{2}\left(x_n e^{in\phi} + x_n^* e^{-in\phi}\right)$	$\lvert x_n \rvert$	$\tan^{-1}\left(\frac{-\operatorname{Im}(x_n)}{\operatorname{Re}(x_n)}\right)$	$\operatorname{Re}(x_n)$	$-\operatorname{Im}(x_n)$	$\frac{x_0}{2}$
$\frac{1}{2}\left(\lvert x_n \rvert e^{-i\delta_{x_n}} e^{in\phi} + \lvert x_n \rvert e^{i\delta_{x_n}} e^{-in\phi}\right)$	$\lvert x_n \rvert$	δ_{x_n}	$\lvert x_n \rvert \cos(\delta_{x_n})$	$-\lvert x_n \rvert \sin(\delta_{x_n})$	$\frac{x_0}{2}$

Figure 3.1: Fourier Presentation Transformations. The $\tan^{-1}$ function always refers to a two-argument inverse tangent with output range $(-\pi, \pi)$. All entries in the same column are equivalent. The first column is equal to the real-valued physical field. The final column indicates the value of the mean (equilibrium) field.

3.2 Discrete Spatial Fourier Decomposition with the Toroidal Array

The toroidal array measures B_ϕ and B_θ at 64 toroidal locations. The array is fixed at $r \approx a$ and at $\theta = 119$ degrees using the standard right handed MST coordinate system ($\theta = 241$ degrees in the left handed coordinate system). The set of magnetic signals is decomposed into the Fourier basis functions

$$B(\phi) = \sum_{n=0}^{\infty} \alpha_n \cos(n\phi) + \beta_n \sin(n\phi).$$

So, a single coil (the ith toroidal array pickup coil) sees

$$B(\phi_i) = \sum_{n=0}^{\infty} \alpha_n \cos(n\phi_i) + \beta_n \sin(n\phi_i). \tag{3.2.1}$$

In a 64-coil discreet decomposition, we can determine only α_{0-31} and β_{1-32}. The inverse transform (equation 3.2.1) can be written in matrix form:

$$\begin{pmatrix} B(\phi_1) \\ B(\phi_2) \\ B(\phi_3) \\ B(\phi_4) \\ B(\phi_5) \\ B(\phi_6) \\ \\ \\ \vdots \\ \\ \\ B(\phi_{32}) \end{pmatrix} = \begin{pmatrix} 1 & \sin(\phi_1) & \cos(\phi_1) & \sin(2\phi_1) & \cos(2\phi_1) & \cdots & \sin(31\phi_1) & \cos(32\phi_1) \\ 1 & \sin(\phi_2) & \cos(\phi_2) & \sin(2\phi_2) & \cos(2\phi_2) & \cdots & \sin(31\phi_2) & \cos(32\phi_2) \\ 1 & \sin(\phi_3) & \cos(\phi_3) & \sin(2\phi_3) & \cos(2\phi_3) & \cdots & \sin(31\phi_3) & \cos(32\phi_3) \\ 1 & \sin(\phi_4) & \cos(\phi_4) & \sin(2\phi_4) & \cos(2\phi_4) & \cdots & \sin(31\phi_4) & \cos(32\phi_4) \\ 1 & \sin(\phi_5) & \cos(\phi_5) & \sin(2\phi_5) & \cos(2\phi_5) & \cdots & \sin(31\phi_5) & \cos(32\phi_5) \\ 1 & \sin(\phi_6) & \cos(\phi_6) & \sin(2\phi_6) & \cos(2\phi_6) & \cdots & \sin(31\phi_6) & \cos(32\phi_6) \\ & & & & & & & \\ & & & & & & & \\ \vdots & \vdots & \vdots & \vdots & & \ddots & & \\ & & & & & & & \\ & & & & & & & \\ 1 & \sin(\phi_{32}) & \cos(\phi_{32}) & \sin(2\phi_{32}) & \cos(2\phi_{32}) & \cdots & \sin(31\phi_{32}) & \cos(32\phi_{32}) \end{pmatrix} \begin{pmatrix} \alpha_0 \\ \beta_1 \\ \alpha_1 \\ \beta_2 \\ \alpha_2 \\ \beta_3 \\ \\ \\ \vdots \\ \\ \beta_{31} \\ \alpha_{32} \end{pmatrix}$$

The above is a 32×32 invertible matrix, which has values between ± 1. Designating this matrix $\mathbf{A}$,

$$\mathbf{B}_{\text{coils}} = \mathbf{A} \cdot \mathbf{B}_{\text{mode}}$$

Therefore

$$\mathbf{B}_{\text{mode}} = \mathbf{A}^{-1} \cdot \mathbf{B}_{\text{coils}}$$

So, to perform the Fourier decomposition of the toroidal array signals, we need only to take the inversion of the **A** matrix, using the angles of the physical coils $(\phi_1, \phi_2, ...)$, and multiply by their signals. This is the method that is used by the standard MST software to find the toroidal array mode quantities. These values are converted to the amplitude and phase notation of equation 3.1.1 before they are stored in the MST database, using the relations (which are also found in Figure 3.1)

$$\begin{aligned} a_n &= \sqrt{\alpha_n^2 + \beta_n^2} \\ \delta_n &= \tan^{-1}(\alpha_n, \beta_n) \end{aligned}$$

where $\tan^{-1}$ is the two argument inverse tangent function, which has an output range of $(-\pi, \pi)$.

3.3 The Random Phase Approximation

The ability to take a pseudospectrum relies heavily on the assumption that we can take a large number of shots in lieu of a large number of measurements. We will start by defining a somewhat abstract quantity: Suppose we had taken a global measurement of the quantity of interest (that is, suppose instead of a point measurement, we had an infinite number of measurements spread around in space). It is then simple to take an average over a single flux surface:

$$< X >= \frac{\oint X dA}{\oint dA}$$

where $\oint dA$ represents an integration over the flux surface.[1]

The total quantity, $X(\theta, \phi)$, can be decomposed into an average part plus a fluctuation, $\widetilde{X}$, defined by

[1] Under the other assumptions of this method (cylindrical plasma with $m = m(n)$), an average over the flux surface is equivalent to an average over toroidal angle. Strictly speaking, the random phase approximation only relates a toroidal average to an ensemble average.

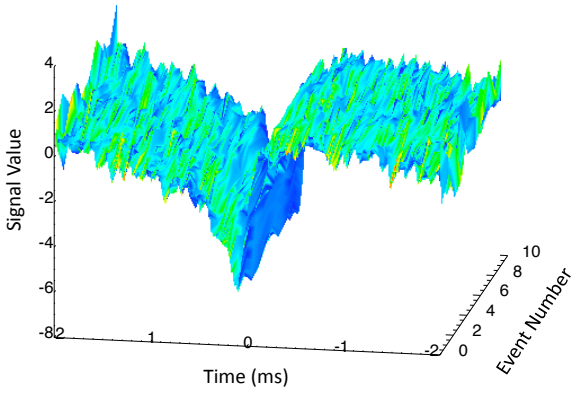

Figure 3.2: Cartoon of a typical sawtooth signal. We can find $< X >$ by averaging across the ensemble (into the page) without losing time resolution.

$$\widetilde{X} \equiv X - < X >$$

Note that $< \widetilde{X} >= 0$. That is, the fluctuations have a flux surface average of zero by definition. Using the complex Fourier notation of 3.1.2, $< X >= \frac{x_0}{2}$ and $\widetilde{X} = \sum_{n=1}^{\infty} X_n$, where $X_n \equiv \frac{1}{2}\left(x_n e^{i(m\theta+n\phi)} + x_n^* e^{-i(m\theta+n\phi)}\right)$.

To measure something that approximates $< X >$, we can take many shots and do a sawtooth ensemble instead of measuring the entire flux surface. This will be done at each time point (relative to the sawtooth crash) separately. The average over many similar sawtooth events is approximately equal to the flux surface average of a single event, $< X >$, but only if the phase of the fluctuating component, $\widetilde{X}$, is sufficiently random from shot to shot (this is ill defined at the moment, but will be clarified later).

Mathematically speaking, we approximate

$$< X(\theta, \phi) > \approx [x(\text{point})]$$

where [ ] represents an average over realizations of the sawtooth and <> still represents an actual flux surface average in space. This principle will be called the *random phase approximation*.

3.4 Products of fluctuations

Although fluctuations of a single quantity average to zero by definition, products of fluctuations may not.

$$< XY >=< X >< Y > + < \widetilde{X} >< Y > + < X >< \widetilde{Y} > + < \widetilde{X}\widetilde{Y} >$$

$$=< X >< Y > + < \widetilde{X}\widetilde{Y} >$$

If the modes are Fourier decomposed, they will obey the familiar orthogonality relationships between sine waves,

$$\begin{aligned} \oint \sin(kx)dx &= 0 \\ \text{and } \oint \sin(kx)\sin(lx)dx &= 0 \\ \text{but } \oint \sin(kx)\sin(kx)dx &\neq 0 \end{aligned}$$

where $\oint$ means the integral over an integer number of periods. Indeed, this orthogonality is precisely the reason why a Fourier basis set is convenient for describing our signals.

3.5 Solving the Pseudospectrum

We have established the notation

$$X =< X > + \sum_{n=1}^{\infty} X_n = \sum_{n=0}^{\infty} |x_n| \cos(m\theta + n\phi - \delta_{x_n}) = \sum_{n=-\infty}^{\infty} \frac{1}{2} x_n e^{im\theta + in\phi} = \sum_{n=-\infty}^{\infty} \frac{1}{2} |x_n| e^{i(m\theta + n\phi - \delta_{x_n})}$$

Let us apply the same notation to our magnetic field at the wall, B.

$$B =< B > + \sum_{n=1}^{\infty} B_n = \sum_{n=0}^{\infty} |b_n| \cos(m\theta + n\phi - \delta_{b_n}) = \sum_{n=-\infty}^{\infty} \frac{1}{2} b_n e^{im\theta + in\phi} = \sum_{n=-\infty}^{\infty} \frac{1}{2} |b_n| e^{i(m\theta + n\phi - \delta_{b_n})}$$

To find the pseudospectrum of our signal, X, we must first make the basic assumption that X

is strongly coupled to the magnetic field at the wall. Namely, our assumption is that for each mode,

$$x_n e^{i(m\theta+n\phi)} = c_n b_n e^{i(m\theta+n\phi)}$$

so

$$c_n = \frac{|x_n|}{|b_n|} e^{i(\delta_b - \delta_x)}$$

where c_n is a complex constant of proportionality and is deterministic (i.e. c_n is the same for every realization of the sawtooth)

This, of course, is a major assumption–we are saying that the X_n's are always phase-locked to the B_n's. This assumption is very reasonable for magnetic fields since magnetic structures are radially broad in MST plasmas, but application of this argument to other measurements, for example temperature or density, may be a bit more subtle. Notice that X_n will have a different (random) phase for each sawtooth realization, but we assume it will always have a deterministic *relative* phase to B_n. Further, since each time point is processed independently, this relative phase will be allowed to vary in time with respect to the sawtooth crash time.

So, instead of finding the x_n's (which appear at a random phase for each realization), we will find the quantity

$$\mathbf{x}_n = |x_n| e^{i(\delta_{bn} - \delta_{xn})} = c_n |b_n|$$

This is a more meaningful number: The amplitude of X_n is $|\mathbf{x}_n|$, and the phase of $\mathbf{x}_n$ tells us whether X_n is in phase or out of phase with B_n. Additionally recognizing that the random phase approximation will eventually be utilized, we define the *pseudospectrum* of X to be

$$\{X\} = \begin{pmatrix} \mathbf{x}_0 \\ \mathbf{x}_1 \\ \mathbf{x}_2 \\ \mathbf{x}_3 \\ \vdots \end{pmatrix}.$$

The pseudospectrum is intended to represent the amplitude and phase of the nth mode of X. To maintain this intuition, we want to define $\mathbf{x}_0$ so that it also represents the "amplitude and phase of

the $n = 0$ mode", which we know to simply be the real value $\mathbf{x}_0 = [X]$.

Now that we have defined what a pseudospectrum is, we wish to calculate it in terms of measured values. We start by defining three quantities:

$$X = \sum_{n'=-\infty}^{\infty} \frac{1}{2} x_{n'} e^{i(m'\theta + n'\phi)}$$

$$B_n \equiv |b_n| \cos(m\theta + n\phi - \delta_{b_n}) = \frac{\left(b_n e^{i(m\theta+n\phi)} + b_n^* e^{-i(m\theta+n\phi)}\right)}{2}$$

$$B_n^\dagger \equiv |b_n| \sin(m\theta + n\phi - \delta_{b_n}) = \frac{\left(b_n e^{i(m\theta+n\phi)} - b_n^* e^{-i(m\theta+n\phi)}\right)}{2i}$$

As a quick aside, note that B_n is physically the nth mode of the plasma, while $B^\dagger$ is the magnetic mode in a toroidally shifted reference frame.

We construct two flux surface averages:

$$
\begin{aligned}
< XB_n > &= < \left(\sum_{n'=-\infty}^{\infty} \frac{1}{2} x_{n'} e^{i(m'\theta + n'\phi)} \right) \frac{1}{2} \left(b_n e^{i(m\theta + n\phi)} + b_n^* e^{-i(m\theta + n\phi)} \right) > \\
&= \frac{1}{4}(x_n b_n^* + x_n^* b_n) \\
&= \frac{1}{4}(c_n b_n b_n^* + c_n^* b_n^* b_n) \\
&= \frac{1}{4}|b_n|^2 (c_n + c_n^*) \\
&= \frac{1}{4}(\mathbf{x}_n + \mathbf{x}_n^*)|b_n| \\
< XB_n^\dagger > &= < \left(\sum_{n'=-\infty}^{\infty} \frac{1}{2} x_{n'} e^{i(m'\theta + n'\phi)} \right) \frac{1}{2i} \left(b_n e^{i(m\theta + n\phi)} - b_n^* e^{-i(m\theta + n\phi)} \right) > \\
&= \frac{1}{4i}(-x_n b_n^* + x_n^* b_n) \\
&= \cdots \\
&= \frac{1}{4i}(-\mathbf{x}_n + \mathbf{x}_n^*)|b_n|
\end{aligned}
$$

Solving for $\mathbf{x}_n$,

$$
\mathbf{x}_n = \frac{2 < XB_n > -2i < XB_n^\dagger >}{|b_n|}
$$

We apply the random phase approximation: Instead of a flux surface average, we take an ensemble average of data at a single point.

$$\mathbf{x}_n = \frac{2 < XB_n > -2i < XB_n^\dagger >}{|b_n|} \approx \frac{2[X(point)B_n(point)] - 2i[X(point)B_n^\dagger(point)]}{[|b_n|]} \tag{3.5.1}$$

Here, we have made the substitution $|b_n| = [|b_n|]$. The pseudospectrum method relies on the assumption that the sawtooth events are similar to one another, so that each event will measure the same quantity, but at a different phase. If this assumption holds, it must also be true that $|b_n|$ does not significantly vary across the ensemble. Mostly, however, we expect the pseudospectrum to be an ensemble average quantity, not a rigidly defined relationship that is meant to be applied on a shot to shot basis, and therefore it should be constructed of only ensemble average quantities.

We can calculate the local B_n and $B_n^\dagger$ from the toroidal array signals.

$$\begin{aligned} B_n(point) &= |b_n| \cos(m\theta|_{point} + n\phi|_{point} - \delta_{b_n}) \\ &= |b_n| \cos(\Delta_n - \delta_{b_n}) \\ B_n^\dagger(point) &= |b_n| \sin(\Delta_n - \delta_{b_n}) \end{aligned}$$

Here we have defined $\Delta_n = (m\theta|_{point} + n\phi|_{point})$ which is just a geometric factor determined by the location of the point at which $X(point)$ is measured. In other words Δ_n represents the relative phase difference due to the space between the measurement that is made and the "zero" point used in the Fourier decomposition of the magnetic array measurements. For the MST toroidal array mode analysis, this zero point is at $(\phi = 0, \theta = 241)$ in the left handed coordinate system, located at the lower inboard side of the poloidal gap. In practice, we use

$$\Delta_n = n\phi_{probe} + m\left(\theta_{probe} - 241\right).$$

with m and n both positive. This form is used in conjunction with the left handed coordinate system, and accounts for the toroidal array's physical θ position. This is discussed in more detail in section 3.6.1.

In terms of measured quantities,

$$\mathrm{Re}(\mathbf{x}_n) = \frac{2[X(point)|b_n|\cos(\Delta_n - \delta_{b_n})]}{[|b_n|]} \tag{3.5.2}$$

$$\mathrm{Im}(\mathbf{x}_n) = \frac{-2[X(point)|b_n|\sin(\Delta_n - \delta_{b_n})]}{[|b_n|]}$$

Where $|b_n|$ is the amplitude of the nth magnetic mode, stored in the database under the names Bt_n01_amp, Bt_n02_amp, Bt_n03_amp, Bt_n04_amp, Bp_n05_amp, Bp_n06_amp, Bp_n07_amp, Bp_n08_amp. Similarly, δ_{b_n} are stored as Bt_n01_phs, etc.. We sometimes use B_ϕ and sometimes B_θ for reasons discussed in section 3.7.

The physical fields can be found from the pseudospectral values using the conversions listed in Figure 3.1. In particular, the physical field is

$$X_n(\phi) = |\mathbf{x}_n|\cos(n\phi + m\theta - \mathrm{phs}(\mathbf{x}_n) - \delta_{b_n}),$$

while the pseudospectral values directly indicate the field in a frame rotating with the magnetic field at the wall,

$$X_n(\phi) = |\mathbf{x}_n|\cos(n\phi + m\theta - \mathrm{phs}(\mathbf{x}_n)).$$

Here, $\mathrm{phs}(\mathbf{x}_n) = \tan^{-1}\left(\frac{-\mathrm{Im}(\mathbf{x}_n)}{\mathrm{Re}(\mathbf{x}_n)}\right) = \delta_{x_n} - \delta_{b_n}$.

3.6 The Sign of m and n

One common point of confusion is the correct identification of the sign of m and n. The relative sign of these two wave numbers is not arbitrary, but rather is strictly set by a combination of plasma physics, coordinate system choice, and analysis method.

First, let us assume that these are resonant tearing modes with the expected (right- or left-handed) helicity. This, of course, must be *measured*, and has been done so in the past for standard plasmas. Since this thesis only deals with standard plasmas, we simply assume that the mode which appears in the plasma is of the expected helicity.

The theoretical derivation of tearing modes [1] shows that the unstable mode has a spatial structure which satisfies the condition

$$\left(\vec{B}\cdot\nabla\right)\psi = 0$$

on the rational surface. In a periodic cylinder, with a right handed coordinate system, this is

$$\left(\vec{B}\cdot\nabla\right)\psi = \left(B_\theta\frac{1}{r}\frac{\partial}{\partial\theta} + B_\phi\frac{1}{R}\frac{\partial}{\partial\phi}\right)\psi$$

and is satisfied by

$$\psi = \psi(r)e^{i(n\phi+m\theta)}$$

when

$$\frac{B_\theta}{r}(im) + \frac{B_\phi}{R}(in) = 0$$

or

$$q = -\frac{rB_\phi}{RB_\theta} = \frac{m}{n}.$$

Though this is an odd sign-convention for q, it is consistent with $q > 0$ in the core of MST (in the right handed coordinate system) because $B_\phi > 0$ and $B_\theta < 0$. This definition becomes necessary since MST is typically operated with the toroidal field and plasma current in opposite directions.

For a core mode (any mode resonant inside the reversal surface) to satisfy the resonance condition, m/n must also be positive. (Note, however, that if we are using the left handed coordinate system, described in section 1.4, then both B_θ and B_ϕ are positive, and $m/n < 0$.)

The condition

$$\frac{m}{n} > 0$$

depends solely on the helicity of the mode (set by plasma physics) and the coordinate system chosen. The next step is to solidify the notation by choosing (rather artificially) a sign for n.

The sign of n is chosen to be positive. This choice has intuitive appeal since we are basically "counting" the nodes on a measured toroidal structure. This may seem to be an arbitrary choice, but it has the benefit that it is consistent with the convention used by the toroidal array in its Fourier

basis set (equation 3.1.1).

The phase shift, δ, can be found from the toroidal array data, and the direction of wave propagation (or at least the $\pm\hat{\phi}$ component) can be identified from the sign of $\partial\delta/\partial t$. Any good wave vector should, of course, have an overall sign that reflects the direction of wave propagation, so for physics purposes, we must re-introduce this overall sign to the wave vector,

$$\vec{k} = \text{sign}\left(\frac{\partial\delta}{\partial t}\right)\left(\frac{m}{r}\hat{\theta} + \frac{n}{R}\hat{\phi}\right)$$

with $n > 0$ and the sign of m (which happens to be positive) determined by the mode's expected helicity.

A second method allows the sign of n to vary. This is discussed further in section A.

3.6.1 Implications for Pseudospectral Analysis

The sign of m and n must be known to perform pseudospectral analysis, since it is required for the calculation of Δ_n. The toroidal array uses the left handed coordinate system, so we usually perform pseudospectral analysis in this coordinate system. The toroidal array records the mode's amplitude and phase in the form

$$B = |b_n|\cos(n\phi - \delta_{1\text{D}}).$$

We would prefer, however, to rewrite this into the two dimensional helical form

$$B = |b_n|\cos(n\phi + m\theta - \delta_{2\text{D}}).$$

For the two to be equivalent, we need

$$m\theta - \delta_{2\text{D}} = -\delta_{1\text{D}}$$

to be true at the poloidal location of the toroidal array. Or,

$$\delta_{2\text{D}} = m\theta|_{241} + \delta_{1\text{D}}.$$

Therefore, the physical mode must be

$$B = |b_n| \cos(n\phi + m\theta - (m\theta|_{241} + \delta_{1\mathrm{D}}))$$

And so, to evaluate the mode at a different point (i.e. the location of the probe), we use

$$B(\text{point}) = |b_n| \cos(\Delta_n - \delta_n) = |b_n| \cos(n\phi|_{\text{point}} + m\theta|_{\text{point}} - (m\theta|_{241} + \delta_{1D}))$$

Therefore, we must have

$$\Delta_n = n\phi|_{\text{point}} + m(\theta|_{\text{point}} - \theta|_{241}).$$

We are evaluating this in the left handed coordinate system (the toroidal array's native coordinates), so we should be using $m < 0$ and $n > 0$.

3.7 Modes

A Current Free Boundary

Since MST has a plasma limiter, it is often claimed that there is a vacuum region between the plasma and the wall, and therefore the plasma current density is zero near the wall. This leads to some conclusions about the structure of the modes [2], which we can test against measurement. In particular,

$$\begin{aligned} \mu_0 j_r &= \hat{r} \cdot \left(\nabla \times \widetilde{b} \right)_{r=a} \\ 0 &= \frac{1}{a} \frac{\partial \widetilde{b}_\phi}{\partial \theta} - \frac{1}{R} \frac{\partial \widetilde{b}_\theta}{\partial \phi} \end{aligned}$$

$$\text{Letting} \quad \widetilde{b} = |b| \cos(n\phi + m\theta - \delta_b),$$

$$0 = \frac{n|b_\theta|}{R} \sin(m\theta + n\phi - \delta_{b_\theta}) - \frac{m|b_\phi|}{a} \sin(m\theta + n\phi - \delta_{b_\phi}) \tag{3.7.1}$$

This directly leads to three conclusions:

1. if $m = 0$, then $b_\theta = 0$
2. if $m \neq 0$, then for a right handed coordinate system (in which m and n have the same sign), $\delta_{b_\theta} = \delta_{b_\phi}$. This phase matching condition is required if equation 3.7.1 is to be valid for all angles θ and ϕ.
3. Furthermore, if $m \neq 0$, then $\frac{|b_\phi|}{|b_\theta|} = \frac{na}{mR}$

We can check these results for a single shot (#1090101100):

1) Figure 3.3 shows that the $n = 1$ mode (which is presumably $m = 0$) has an amplitude dominated by B_ϕ. Although we don't see $B_\theta = 0$ strictly, we can see that even during a sawtooth crash $B_\phi >> B_\theta$.

2) In Figure 3.4, the recorded phase of the $n = 6$ mode is plotted between sawtooth, at a time when the plasma is rotating. Notice that this deviates from the predicted behavior—the magnetic field components are out of phase by π—because the toroidal array uses the left handed coordinate system in which $m/n < 0$.

3) Figure 3.5 shows both the amplitude and phase of the $n = 6$ mode. To guide your eye, I have plotted in green quantities related to the conclusions predicted by a vacuum layer: In the first plot we have shown $\frac{na}{mR} B_\theta$, using $R = 1.26$, the major radial location of the toroidal array. In the second plot, the green points should be zero if the expected phase relationship is satisfied.

These Figures seem to indicate that the predictions of $j_r = 0$ hold away from this sawtooth, but aren't too convincing at the time of the crash. The reason for this discrepancy may be partly due to plasma breaching the vacuum layer boundary, producing a finite radial plasma current (j_r) at the wall; or, the $n = 6$ component could be significantly polluted by an $m = 0$ mode. Though we we don't have a direct measurement of the mode amplitude of this $(0, 6)$ mode, we can estimate its expected value by extrapolating from the $n = 1 - 4$ modes. Figure 3.6 shows that it would not be too surprising to find a $(0, 6)$ mode with a B_ϕ value that is comparable to the 20 Gauss $(1, 6)$ mode amplitude we would expect from the $(1, 6)$ B_θ value. There may even be a hint of this effect in the lower plot of Figure 3.5, where the phase difference appears to have a rotation frequency. This could be arise from the "beat frequency" between the $(1, 6)$ and $(0, 6)$ modes, which may not be propagating coherently.

Though the $j_r = 0$ predictions are a bit shaky for this single shot, in a sawtooth ensemble average the predictions hold more strongly. Figure 3.7 shows the average mode amplitude of B_ϕ and the adjusted amplitude $\frac{na}{mR} B_\theta$ assuming $m = 1$. The poloidal field value is an indicator of the modes $m = 1$ content, while the difference between poloidal and toroidal curves indicates the mode's $m = 0$ content.

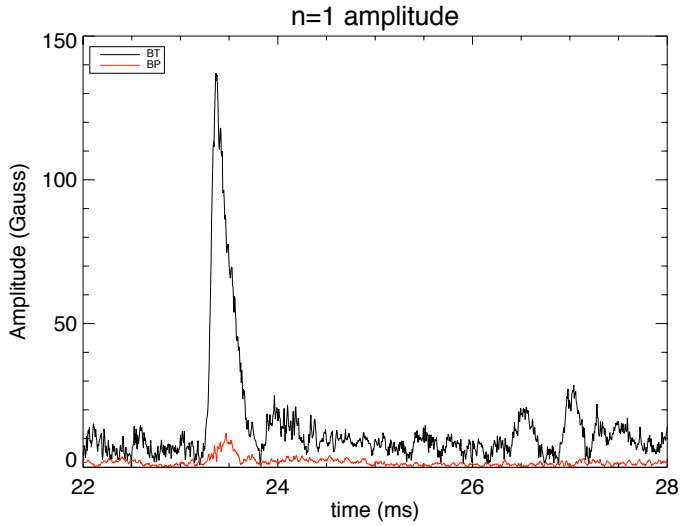

Figure 3.3: Single shot comparison of B_ϕ and B_θ $n = 1$ amplitude.

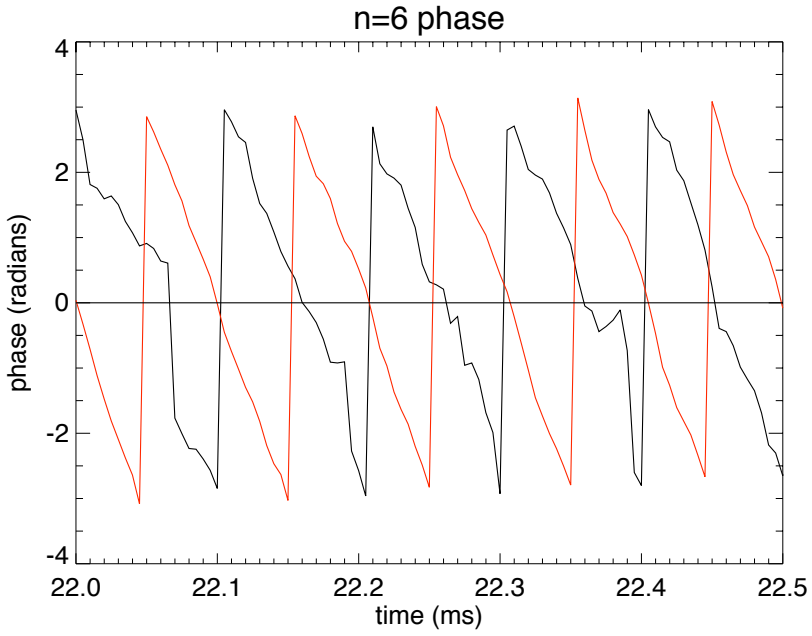

Figure 3.4: Single shot comparison of B_ϕ and B_θ phases for $n = 6$ away from sawtooth.

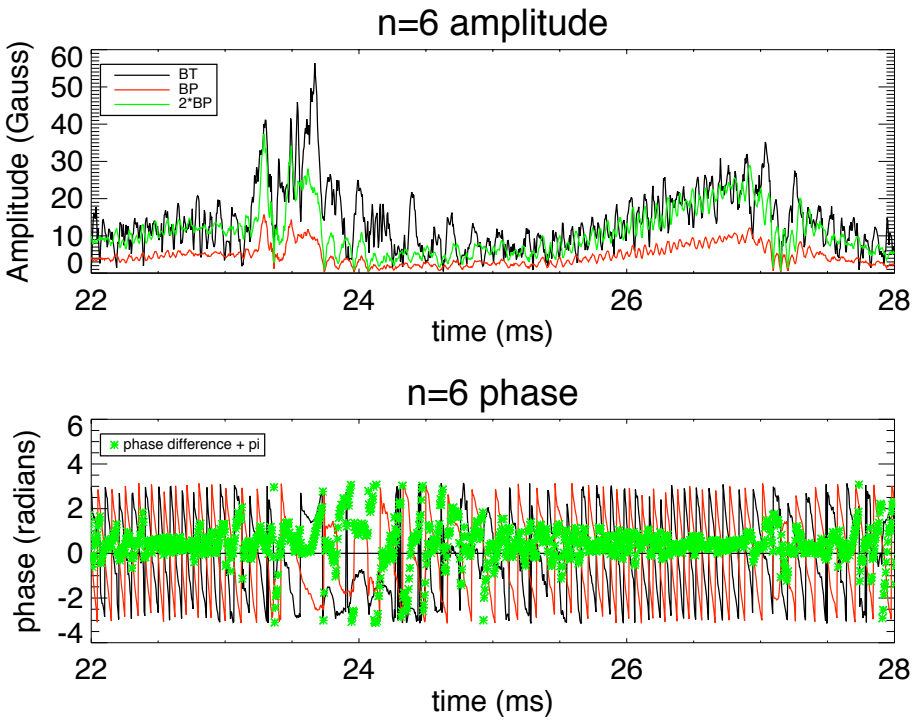

Figure 3.5: Single shot comparison of B_ϕ and B_θ mode amplitude and phase for $n = 6$.

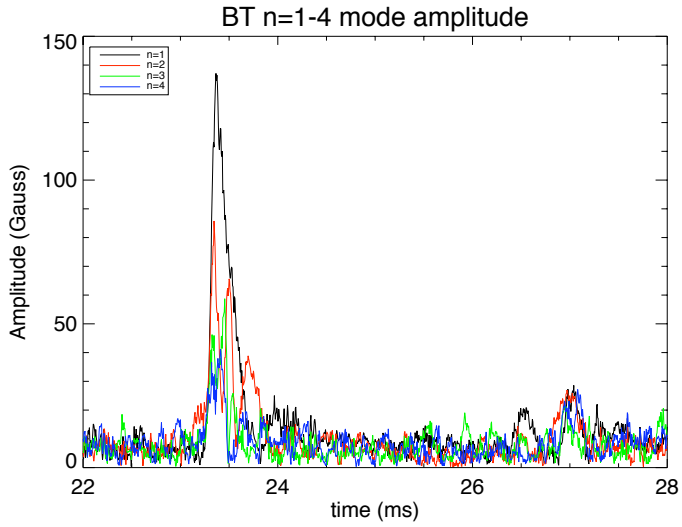

Figure 3.6: Single shot comparison of B_ϕ for $n = 1 - 4$.

3.7.1 Implications for Pseudospectral Analysis

If we assume that the boundary is current free, we are led to the following conclusions: We must use B_ϕ to calculate the amplitude and phase of the $m = 0$ modes, because we expect that any B_θ component is either an experimental error, an $m = 1$ mode, or some unaccounted for effect (i.e. toroidal effects, field errors, etc.). The $m = 1$ modes, however, must use B_θ for correlation because this is the only way to ensure that the mode amplitude is not significantly polluted by the $m = 0$ modes.

If we need to compare the phase of an $m = 1$ mode with the phase of an $m = 0$ mode, such as in the calculation of a three wave nonlinear interaction term, we must again take these behaviors into account. The best procedure to do this is to measure the $m = 1$ mode using B_θ, and convert this to the phase relative to B_ϕ by assuming a phase difference of exactly π.

3.8 Checking the Random Phase Approximation

It was mentioned that the random phase approximation must be valid for us to legitimately talk about a pseudospectrum. To check this, we must check the randomness of δ_{x_n}: if this value samples

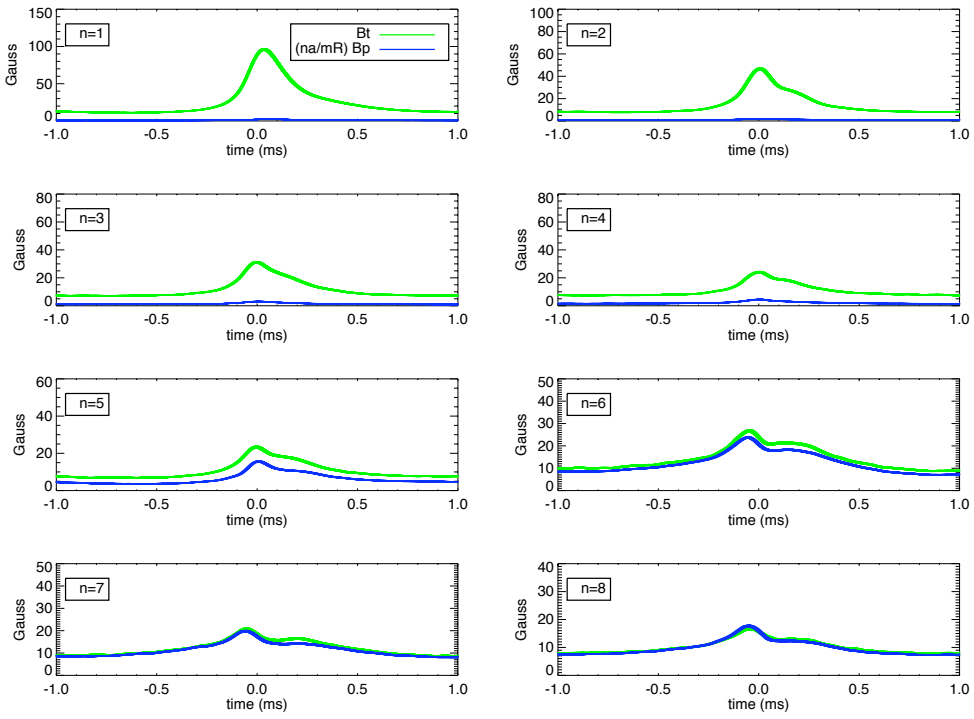

Figure 3.7: Ensemble averaged mode amplitudes of B_ϕ and $\frac{na}{mR}B_\theta$ assuming $m = 1$.

all phases evenly (for each time point relative to the sawtooth crash), then the conditions of the random phase approximation have been satisfied.

Recall that the phase of the pseudospectrum, $\text{phs}(\mathbf{x}_n) = \tan^{-1}\left(\frac{-\text{Im}(\mathbf{x}_n)}{\text{Re}(\mathbf{x}_n)}\right)$, is constant across the ensemble, while the notation δ_{x_n} refers to the actual phase of the quantity X_n, which is usually rotating in time and random between ensemble events. After we have calculated the pseudospectrum, δ_{x_n} can be found:

$$\mathbf{x}_n = |x_n| e^{i(\delta_{x_n} - \delta_{b_n})}$$

$$\therefore \delta_{x_n} = \tan^{-1}\left(\frac{-\text{Im}(\mathbf{x}_n)}{\text{Re}(\mathbf{x}_n)}\right) - \tan^{-1}\left(\frac{-\text{Im}(b_n)}{\text{Re}(b_n)}\right)$$

So, the random phase approximation is valid if and only if a histogram of δ_{xn}, or equivalently a histogram of δ_{bn}, looks flat (is evenly sampled) for all time points of interest.

3.9 Error of the Pseudospectrum

Error calculations can be performed by the error propagation of ensemble variation[3]. This event-to-event variation can be assumed to be random and follow a Gauss distribution. When performing error propagation, however, we must be careful to use methods associated with dependent variables (i.e. not quadratic sums) since separate measurements (such as probe measurements and toroidal array measurements) are correlated.

To calculate error, we begin with the ensemble quantities of a signal. Suppose we have measured x using a probe, and we calculate

$$\begin{aligned} \bar{x} &= \frac{\sum x_i}{N} \\ \sigma_x &= \sqrt{\frac{\sum (x_i - \bar{x})^2}{N}} \end{aligned}$$

Here, $\bar{x}$ is the average value of the measurement, and σ_x is the standard deviation, or error, of that signal. (Both of these quantities are outputs of the standard MST sawtooth ensemble software, discussed further in Appendix A) Defined in this way, note that σ_x always has the same units as x.

This error can be interpreted as a confidence level, such that we are 68% confident that any given measurement will have a value

$$x_i = \bar{x} \pm \sigma_x$$

and we are 95% confident that each measurement will be within 2σ. The error associated with the value $\bar{x}$ is much smaller, and is given by the standard deviation of the mean,

$$\sigma_{\bar{x}} = \frac{\sigma_x}{\sqrt{N}}$$

Each individual measurement, however, is still stuck with an error of σ_x.

Recall that the pseudospectrum is given by

$$\mathrm{Re}(\mathbf{x}_n) = \frac{2[X(point)|b_n|\cos(\Delta_n - \delta_{bn})]}{[|b_n|]}$$

$$\mathrm{Im}(\mathbf{x}_n) = \frac{-2[X(point)|b_n|\sin(\Delta_n - \delta_{bn})]}{[|b_n|]}$$

The spread in $\mathrm{Re}(\mathbf{x}_n)$ is maximized if the $\cos(\Delta_n - \delta_{bn}) = \pm 1$ and always conspires to have the same sign as X. So, for purposes of error analysis, we will find the error associated with the quantity

$$q = \frac{[|X(point)||b_n|]}{[|b_n|]}$$

and to simplify notation, $X(point) = X$, $b_n = b$

One could argue that the spread in $|b_n|$ tends to cancel since it appears in the numerator and denominator of q, in which case we would simply have gotten

$$\sigma_q = \frac{\sigma_{|X|}}{\sqrt{N}}.$$

This is equivalent to saying that $< AB > \approx < A >< B >$, which we know isn't quite true. To take it one step higher in sophistication,

$$\begin{aligned}
\frac{\sigma_q}{q} &= \frac{\sigma_{[|Xb|]}}{[|Xb|]} + \frac{\sigma_{[|b|]}}{[|b|]} \\
\frac{\sigma_{|Xb|}}{|Xb|} &= \frac{\sigma_{[|X|]}}{[|X|]} + \frac{\sigma_{[|b|]}}{[|b|]} \\
&= \frac{\sigma_{[|X|]}}{[|X|]} + \frac{2\sigma_{[|b|]}}{[|b|]} \\
&= \frac{\sigma_{|X|}}{\sqrt{N}[|X|]} + \frac{2\sigma_{|b|}}{\sqrt{N}[|b|]} \\
\sigma_q &= \frac{1}{\sqrt{N}} \left(\frac{\sigma_{|X|}[|Xb|]}{[|X|][|b|]} + \frac{2\sigma_{|b|}[|Xb|]}{[|b|]^2} \right)
\end{aligned}$$

Next, we calculate the quantities of interest:

$$\begin{aligned}
\sigma_{\mathrm{Re}(\mathbf{x}_n)} &\leq 2\sigma_q \\
\sigma_{\mathrm{Im}(\mathbf{x}_n)} &\leq 2\sigma_q
\end{aligned}$$

3.10 Pseudospectrum Performance

The pseudospectral method can be verified by calculating an autocorrelation function using a single toroidal array coil (i.e. using one coil of the toroidal array as the "probe"). Figures 3.8 and 3.9 show that the pseudospectral method correctly reproduces the average mode amplitude for modes $n = 1-8$ for a typical ensemble. The relative phases of each mode are also correctly reproduced, as shown in Figure 3.10. In particular, this ensemble reproduces the $n = 1$ mode amplitude well. Furthermore, the width of the lines, which represent one standard deviation in the ensemble statistics, produce a

reasonable representation of the error in the measurement. Discrepancies between the true amplitude and the pseudospectral reproduction can usually be attributed to a peaked phase distributions for the mode in question. These errors can be reduced by increasing the ensemble size and ensuring even phase sampling. The discrepancy of error size in toroidal versus poloidal fields could be reduced by enforcing tighter constraints on the ensemble (this ensemble was tightly constrained in total plasma current, which likely reduces the spread in poloidal field).

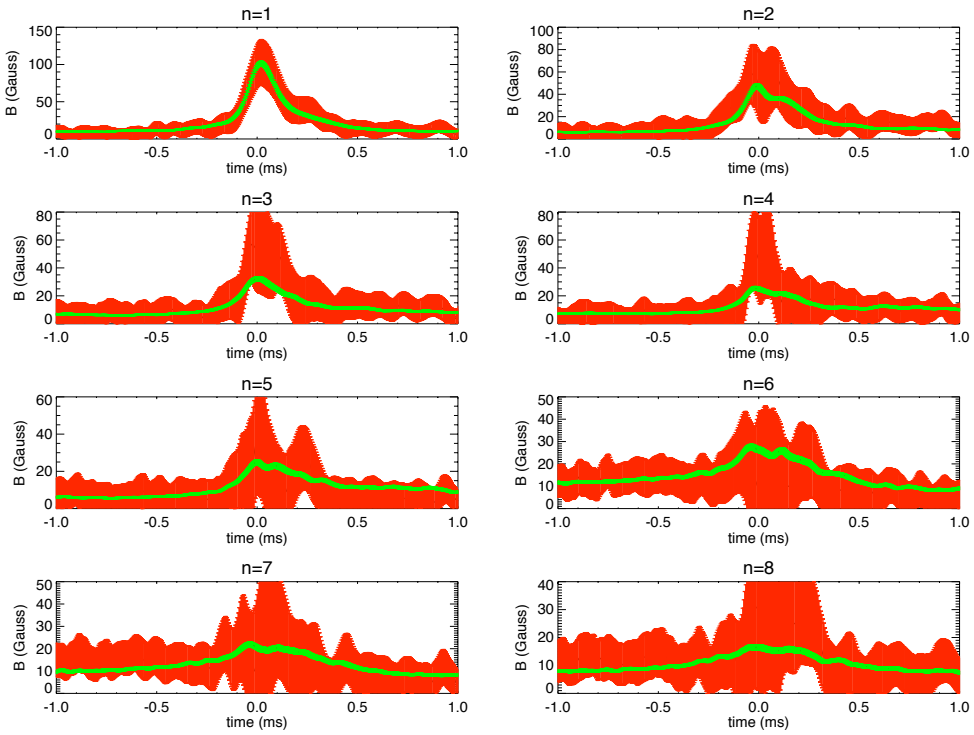

Figure 3.8: Pseudospectral reproduction of B_ϕ mode amplitudes: The pseudospectrum (red) of a toroidal array coil and the average mode amplitude (green) for $n = 1 - 8$.

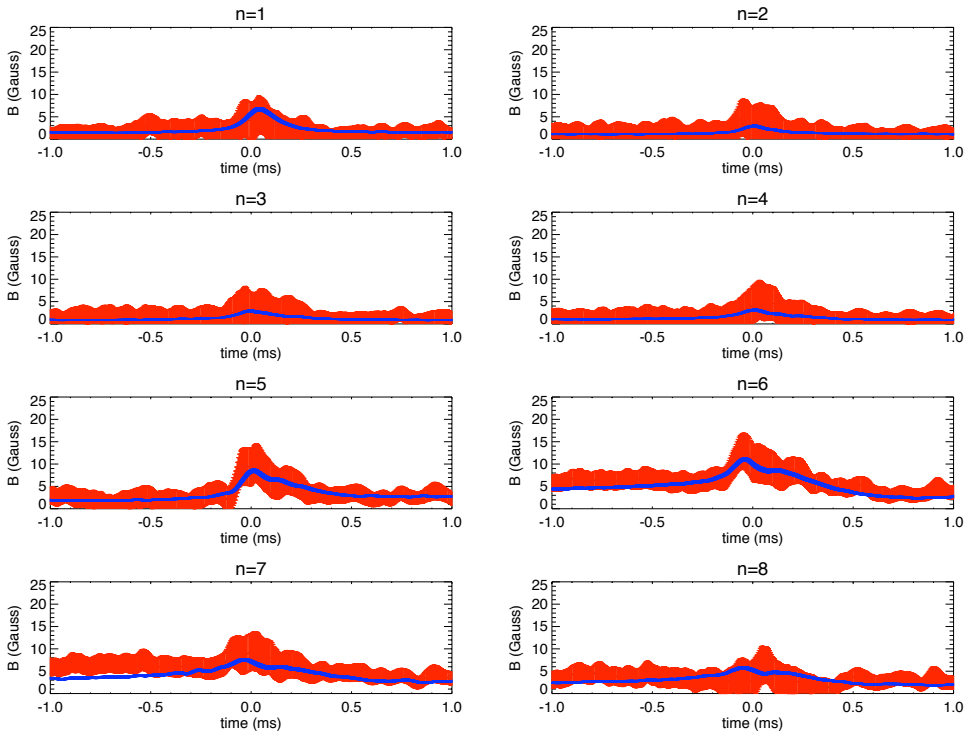

Figure 3.9: Pseudospectral reproduction of B_θ mode amplitudes: The pseudospectrum (red) of a toroidal array coil and the average mode amplitude (blue) for $n = 1 - 8$.

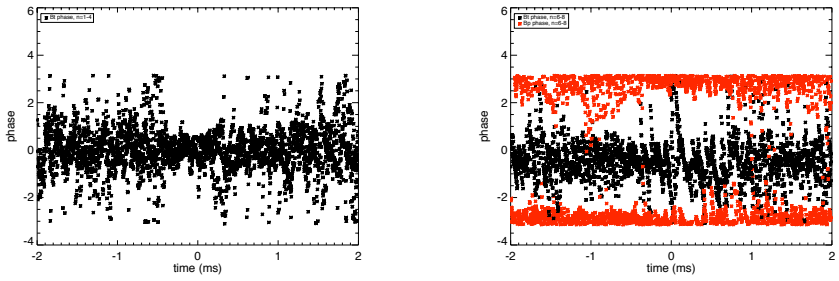

Figure 3.10: Pseudospectrum phase plots: Phase reconstructions of (left) B_ϕ for $n = 1 - 4$ modes; and (right) B_ϕ and B_θ $n = 6 - 8$ modes. The pseudospectrum is calculated relative to B_ϕ for $n < 5$ and relative to B_θ then phase adjusted by π for $n > 5$ modes. These are evaluated in the left handed coordinate system, so we expect $B_\phi = 0$ for all modes, and $B_\theta = \pm\pi$ for $m = 1$ modes.

3.11 References

[1] H. Furth, J. Killeen, and M. Rosenbluth, "Finite resistivity instabilities of a sheet pinch," *The Physics of Fluids*, vol. 6, pp. 459–484, April 1963.

[2] J. T. Chapman, *Spectroscopic Measurements of the MHD Dynamo in the MST Reversed Field Pinch*. PhD thesis, September 1998. pp. 100 - 127.

[3] J. R. Taylor, *An Introduction to Error Analysis*. University Science Books, 2 ed., 1997.

Chapter 4: Magnetic Field Measurements

We have used the magnetic probes discussed in Chapter 2, and the pseudospectral method developed in Chapter 3 to make detailed measurements of fluctuations in the edge of MST. This produces measured profiles of three components of magnetic field (with B_r inferred from $\nabla \cdot B = 0$; see section 6.2.1). This work focuses primarily on the physics of the $n = 1$ mode, though the pseudospectral method results in information about all modes which are detected by the toroidal array and analyzed. For reference, I have included plots of the other measured modes ($n \leq 8$) in Appendix B, though only the $n = 1$ mode measurement has been subject to deep scrutiny.

The analysis methods thus far have been derived assuming a periodic cylinder rather than a true toroidal geometry. In a torus, m is not a "good" quantum number. This means that, though a quantity may still be decomposed into modes, $X = \sum x_n e^{i(m\theta + n\phi)}$), the Fourier coefficients, x_n, are no longer necessarily functions of r [1]. So, while a cylindrical model can calculate (m, n) modes, the same mode in a torus shall here be identified only by its n number. Further, it is important to recognize that the experimental method actually measures only the n spectrum of the probe measurements, without measuring anything of the m spectrum. Nevertheless, as discussed in Chapter 3, derivatives are calculated using the assumed m spectrum from a cylindrical approximation. The results of Section 4.1 may suggest a path to improve this technique in the future.

4.1 Theory comparison of the (0,1) mode

The $n = 1$ mode is known to be linearly stable for the experimentally realized MST equilibrium; however, from a computation standpoint, it is much easier to calculate properties of a linearly unstable mode. Though this mode is nonlinearly driven in the experiment, the comparison with linear theory is justified by noting that slowly varying magnetic perturbations have robust global spatial structures. Since the timescales of the sawtooth cycle are much longer than the Alfvenic timescale, the magnetic components are described by the universal Newcomb-like system of quasi-static equations and are relatively insensitive to the mechanism—linear or nonlinear—of the mode excitation [2].

It has been shown recently [3] that there is a wide class of equilibrium current profiles for which

this mode is spontaneously unstable, some of which are very close (in terms of global parameters) to the experimentally realized equilibrium. One of these profiles, which supports an unstable $n = 1$ mode but has an equilibrium close to that of the experiment, was chosen for evaluation. The cylindrical $(m, n) = (0, 1)$ magnetic eigenmodes were calculated using a resistive MHD eigenvalue code [4]. Here, we used the force-free condition $j = \frac{\lambda(r)}{\mu_0 a} B$, with

$$\mu_0 a \lambda(r, d, w, \alpha) = \lambda_0 \frac{(e^{\frac{r^\alpha - d^\alpha}{w}} + 1)^{-1} - (e^{\frac{1-d^\alpha}{w}} + 1)^{-1}}{(e^{\frac{-d^\alpha}{w}} + 1)^{-1} - (e^{\frac{1-d^\alpha}{w}} + 1)^{-1}}.$$

The equilibrium with $\lambda_0 = -3.35, \alpha = 3, w = 0.08, d = 0.76$ was examined in cylindrical geometry with an aspect ratio of 3 (as the experiment). This profile has realistic values of the pinch and reversal parameters ($\Theta = 1.8$, $F = -0.22$) and a realistic position of the reversal surface ($r_s/a = 0.78$). In this specific case, the edge $m = 0, n = 1$ mode is spontaneously unstable, allowing the code to detect its eigenmode structure.

This same profile was used to run a linear initial value single-fluid simulation using NIMROD [5]. This was run with Lundquist number $S = 10^4$ in a toroidal geometry. Here, the $n = 1$ mode was again observed to be unstable. By incrementally increasing the aspect ratio, convergence of this eigenmode's shape with the shape of the cylindrical $(m, n) = (0, 1)$ eigenmode was observed. At all aspect ratios, the magnetic structure of the toroidal calculation observed along the $R = R_0$ vertical axis closely matches the cylindrical result; this matching is shown for the B_r compenent in Figure 4.1. Due to these observations, it is believed that these modes represent the same instability. The horizontal eigenmode shows a significant B_r contribution at $r = 0$, indicating that this mode has a significant $m \neq 0$ content. Though quantitative investigation is still underway, this can likely be accounted for by the coupling of the $m = 0$ mode to the $(m, n) = (1, 0)$ effect of toroidicity.

In Figure 4.2, we compare the measured $n = 1$ mode with the two linear theoretical calculations. The comparison illustrates substantial differences between the cylindrical and toroidal computations (using $\theta = 15$ degrees in the left-handed coordinate system, as the experiment), and shows strong agreement between experimental profiles and toroidal computation. Comparison with full nonlinear modeling of the RFP in toroidal geometry is yet to be accomplished.

Future work should prioritize verification of these toroidal eigenfunctions at different θ posi-

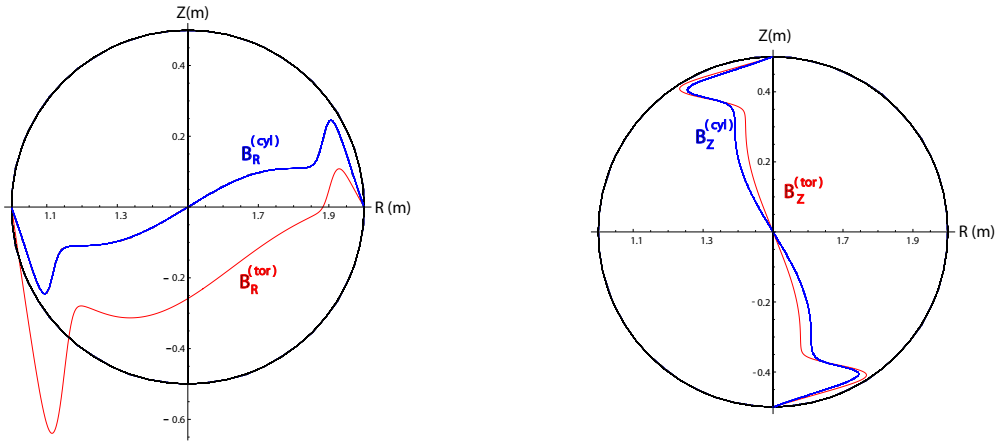

(a) Horizontal

(b) Vertical

Figure 4.1: Eigenmodes calculated in cylindrical (blue) and toroidal (red) for the radial field, B_r (arbitrary units). The two cases match along the vertical axis ($R = R_0$), while significant deformations are observed in the horizontal field.

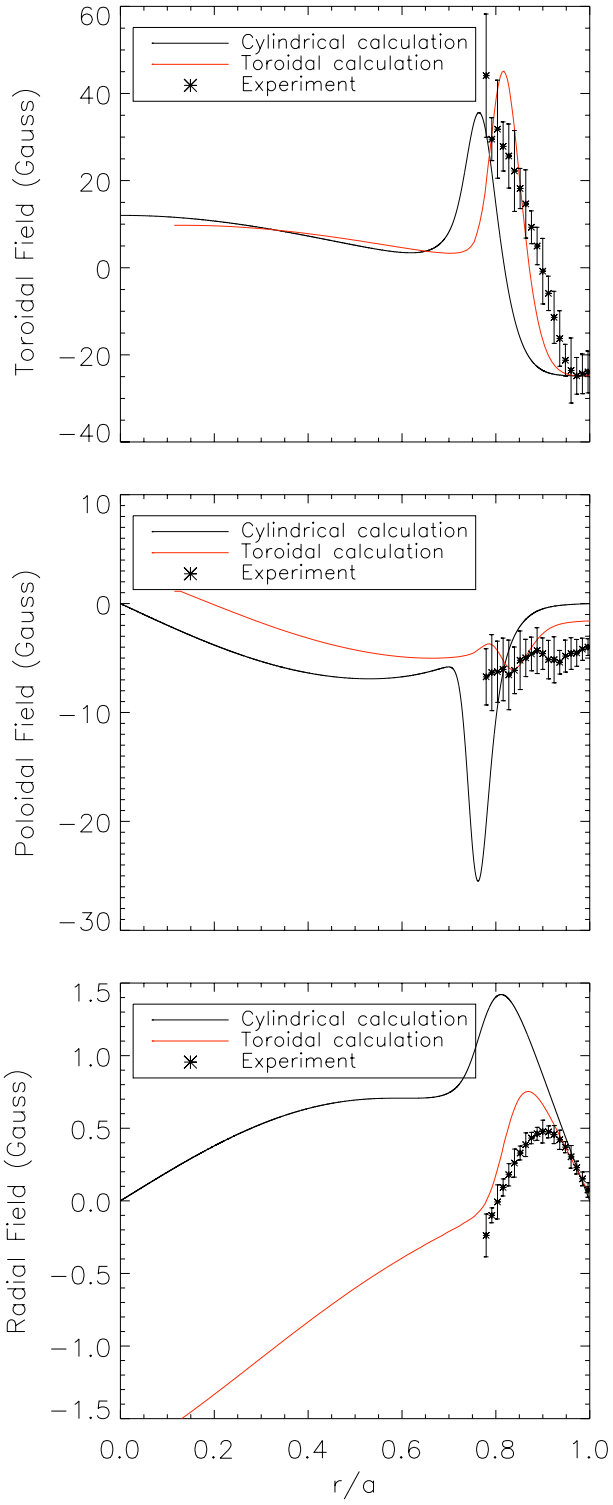

Figure 4.2: Comparison of magnetic field profiles. The magnetic field profiles plotted are the dominant part (real or imaginary) of the magnetic field component (B_t, B_p, or B_r). Since the complimentary part (imaginary or real) is small, these can be interpreted as the mode's amplitude with relative sign information included. The experiment's radial magnetic field, B_r, is inferred from $\nabla \cdot \vec{B} = 0$. Measurements of B_r are consistent with the inferred values but have much larger error bars.

tions. In particular, the theoretical profiles indicate that magnetic field measurements near $\theta = 90$ degrees will agree with cylindrical calculations, while measurements at inboard poloidal angles will have a substantially larger signal, and measurements at outboard poloidal angles will have a substantially smaller signal.

4.2 Summation of Modes

The pseudospectral method of Chapter 3 calculates each mode's phase with respect to $B_n(a)$, effectively removing information about the relative phase between two different n modes. In order to sum the mode structures of modes $n = 1 - 4$ and preserve their relative phases, we must recover this information. We wish to add

$$\begin{aligned} B_n &= b_n \cos(n\phi - \delta_n) \\ &\text{and} \\ B_{n'} &= b_{n'} \cos(n'\phi - \delta_{n'}). \end{aligned}$$

Taking $\phi \rightarrow \phi + \frac{\delta_n}{n}$ will move to the rotating reference frame of the nth mode. Then

$$B_n = b_n \cos(n\phi)$$

and

$$B_{n'} = b_{n'} \cos(n'\phi + \frac{n'}{n}\delta_n - \delta_{n'}) = b_{n'} \cos(n'\phi - \delta_{\text{rel}}),$$

with

$$\delta_{\text{rel}} \equiv \delta_{n'} - \frac{n'}{n}\delta_n.$$

It is interesting to note that, for a rigidly rotating plasma—or, more specifically, a plasma which has all modes locked relative to one another—this combination, $\delta_{\text{rel}} = \delta_{n'} - \frac{n'}{n}\delta_n$ is a constant in time. Considering a sawtooth ensemble, it is seen experimentally that δ_{rel} is a constant of the ensemble, as can be seen from Figure 4.3.

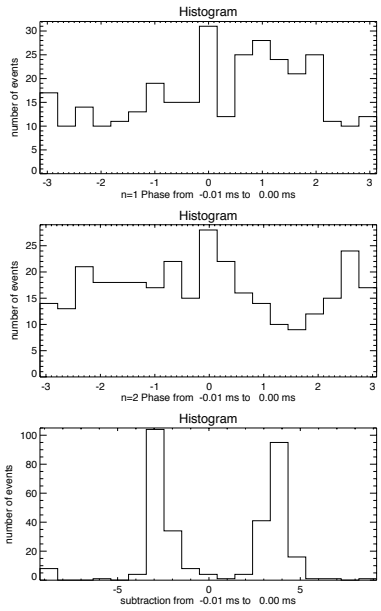

Figure 4.3: The phase distributions for a test ensemble, δ_1, δ_2, and $\delta_{\text{rel}} \equiv \delta_2 - 2\delta_1$. It is seen that while δ_1 and δ_2 have random phases (a flat histogram), the relative phase, δ_{rel} is strongly peaked. Note that the two peaks are separated by 2π and can therefore be thought of as a single peak, indicating that this number is a constant of the ensemble.

So, choosing $n = 1$ and $n' = 2 - 4$, we can sum the individual modes using

$$\begin{aligned} B_{\text{total}} &= B_1 + \sum_{n=2}^{4} B_n \\ &= b_1 \cos(\phi) + \sum_{n=2}^{4} b_n \cos\left(n\phi - (\delta_n - \frac{n}{1}\delta_1)\right). \end{aligned}$$

Of course, this is all applicable at the wall. To find the appropriate phase shift between the wall measurement and the probe location, we must also include the pseudospectral phase shift:

$$B_{\text{total}} = \sum_{n=1}^{4} b_n \cos\left(n\phi - (\delta_n - n\delta_1) - \text{phase}(\mathbf{x}_n)\right).$$

This is the form used for Figure 4.4.

Calculation of an "average phase" must be done correctly to get a meaningful δ_{rel}. To avoid averaging problems with this potentially periodic quantity, this is accomplished by finding the ensemble

average of the sine and cosine of the phase:

$$< \delta_{\rm rel} > \equiv \tan^{-1}\left(\frac{< \sin(\delta_{\rm rel}) >}{< \cos(\delta_{\rm rel}) >}\right). \tag{4.2.1}$$

4.3 Reconnection Structure

With measurement of the mode-resolved magnetic field in hand, the reconnection field structure can be visualized by plotting contours of toroidal flux. Integration of the measured toroidal field from the wall using the equilibrium field plus the $n = 1$ component results in the toroidal flux associated with the $n = 1$ reconnection, and contours of this flux yield a visualization of the associated 2-dimensional field lines, shown in Figure 4.4 (Upper). The addition of the mode contributions from $n = 2, 3, 4$ provide a more complete visualization of the magnetic field, seen in Figure 4.4 (Lower). In particular, the addition of these modes does not destroy the overall shape of the $n = 1$ island, indicating that a coherent $m = 0$ dominated structure likely exists in these plasmas. Though the mode content with $n > 4$ is measured, it is not possible to include them in this picture since these modes have a different m content and therefore a different direction of symmetry. Without the same symmetry direction, a scalar flux cannot be used to describe field lines and a fully 3-D description is required.

The adjustment in the shape of the X-line due to $n > 1$ modes (including the unknown adjustment for $n > 4$) would be a critical consideration for a Sweet-Parker like analysis of reconnection rates. However, if we restrict ourselves to considering the contributions to Ohm's law, the analysis can be evaluated in a Fourier mode basis.

Simulation using DEBS [6] also shows a coherent structure in the edge when plotting contours of toroidal flux. DEBS—a single fluid, 3D, nonlinear resistive MHD simulation in a periodic cylinder—was run using Lundquist number $S = 5 \times 10^5$, resistivity profile $\eta = (1 + 9(\frac{r}{a})^{20})^2$, and Prandtl number of about 100. The plasma equilibrium was initialized with a paramagnetic pinch equilibrium profile and self-consistently evolved. An ideal wall and force free plasma conditions were used.

Figure 4.5 shows a similar "squashing" of the magnetic structure in the analogous plots. In DEBS, the island width is about twice that of the experiment, which is a direct consequence of the large mode amplitudes produced by DEBS. These large modes have typically been observed in DEBS

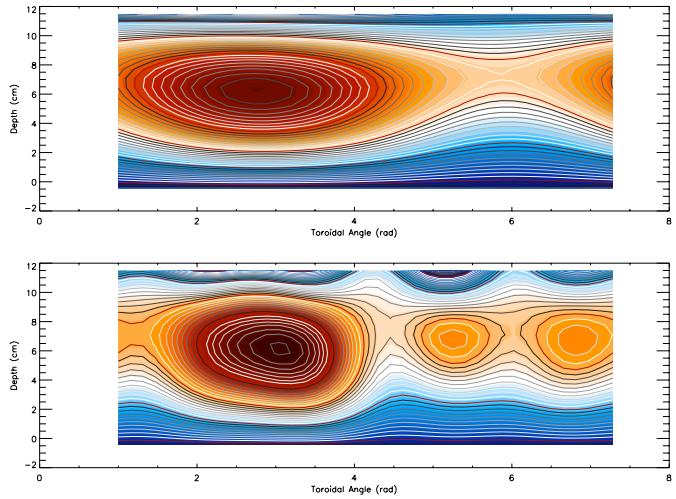

Figure 4.4: Coherent structure in experiment: Contours of constant toroidal flux are shown including the equilibrium and (Upper) $n = 1$ (Lower) $n = 1 - 4$.

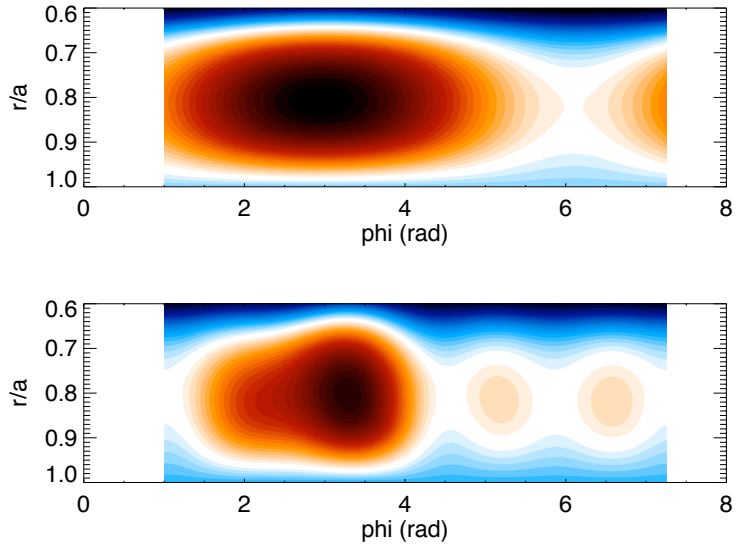

Figure 4.5: Coherent structure in simulation (DEBS): Contours of constant toroidal flux are shown including the equilibrium and (Upper) $n = 1$ (Lower) $n = 1 - 4$.

but the discrepancy with experiment is not yet understood.

Though an obvious comparison to make here would be to recent studies of plasmoid-mediated reconnection [7] [8], it is not possible to conclude from these measurements that the smaller "islands" in the Figure are related to the existence of plasmoids in our experiment. The toroidal resolution available for the experimental plots is limited to $n \leq 4$ (the $m = 0$ modes), which results in these artificial features. Using DEBS we can observe the simulated structure in more detail (since the m content is identifiable) where these features are broken up into even smaller fragments, but the main squashed O-point structure remains intact.

4.4 References

[1] A. H. Boozer *Phys. Fluids*, vol. 24, no. 1999, 1981.

[2] P. Zanca and D. Terranova, "Reconstruction of the magnetic perturbation in a toroidal reversed field pinch," *Plasma Phys. Control. Fusion*, vol. 46, pp. 1115–1141, 2004.

[3] V. Mirnov, C. Hegna, S. Prager, C. Sovinec, and H. Tian, "Two fluid dynamo and edge- resonant m=0 tearing instability in reversed field pinch," *Proc. of the 21th IAEA Fusion Energy Conference (IAEA-CN-149)*, vol. TH, pp. 3–18, 2006.

[4] V. A. Svidzinski, G. Fiksel, V. V. Mirnov, and S. C. Prager, "Modeling of ion heating from viscous damping of reconnection flows in the rfp," *Phys. Plasmas*, vol. 15, no. 062511, 2008.

[5] C. R. Sovinec *et al.*, "Nonlinear magnetohydrodynamics simulation using high-order finite elements," *Journal of Computational Physics*, vol. 195, no. 355, 2004.

[6] D. D. Schnack *et al. Computer Physics Communications*, vol. 43, no. 17, 1986.

[7] N. Loureiro, A. Schekochihin, and S. C. Cowley, "Instability of current sheets and formation of plasmoid chains," *Phys. Plasmas*, vol. 14, no. 100703, 2007.

[8] W. Daughton, V. Roytershteyn, B. J. Albright, H. Karimabadi, L. Yin, and K. J. Bowers, "Transition from collisional to kinetic regimes in large-scale reconnection layers," *Physical Review Letters*, vol. 103, August 2009.

Chapter 5: Dynamo

The equilibrium that exists in the RFP would not be possible without another prevalent feature of plasma dynamics known as the dynamo [1]. A dynamo is a process by which magnetic field is self-generated by the plasma through an inverse cascade of fluctuation quantities. Here, we will use the word a little more loosely to mean any mean field quantity that arises from fluctuation interactions. In particular, we will consider the Hall dynamo term of the equilibrium Ohm's law,

$$< E > + < v_0 \times B_0 > + < \widetilde{v} \times \widetilde{B} >=< \eta J > + \frac{1}{ne}\left(< J_0 \times B_0 > + \underline{< \widetilde{J} \times \widetilde{B} >}\right) + \cdots$$

where the Hall dynamo (the underlined term) is calculated as the average product of fluctuating quantities (as discussed in Chapter 3.4). Ohm's law will be discussed in more detail in Chapter 6.

5.1 Total Dynamo

Previously, the total Hall dynamo has been measured in MST. It can be shown that the total Hall dynamo is given by

$$< \widetilde{J} \times \widetilde{B} >_\theta = \frac{1}{\mu_0}\left(\frac{\partial}{\partial r} + \frac{2}{r}\right) < (\widetilde{B}_\theta \widetilde{B}_r) > . \tag{5.1.1}$$

This well known result is derived in Appendix C.3, and includes contributions from all modes in the plasma. A previously published measurement of this term is presented in Figure 5.1.

5.2 Modal dynamo

A new way to measure the Hall Dynamo uses the pseudospectral method to measure the individual nonlinear dynamo contribution from each mode:

$$\begin{aligned} < J \times B > &= < \left(\sum_{n=-\infty}^{\infty} J_n \right) \times \left(\sum_{n'=-\infty}^{\infty} B_{n'} \right) > \\ &\quad \text{since } < J_n \times B_{n'} > \propto \delta_{nn'} \\ &= < \sum_{n=-\infty}^{\infty} J_n \times B_n > . \end{aligned}$$

This measurement is the same as that of Equation 5.1.1, but now it is mode-resolved: here it is possible to identify the contribution of each n mode to the overall dynamo.

$$< J \times B > = < J_0 \times B_0 > + < J_1 \times B_1 > + < J_2 \times B_2 > + ...$$

The Dynamo contribution by each term is

$$\begin{aligned} (\text{Dynamo})_n &= < X_n \cos(m\theta + n\phi + \delta_x) Y_n \cos(m\theta + n\phi + \delta_y) > \\ &= < |x_n||y_n| \frac{1}{2} \left(\cos(\delta_x - \delta_y) + \cos(2m\theta + 2n\phi + \delta_x + \delta_y) \right) > \\ &= |x_n||y_n| \frac{1}{2} \cos(\delta_x - \delta_y) \end{aligned}$$

where $|x_n|$ and $|y_n|$ are the amplitudes associated with the m, n fourier component of the signals, as usual.

Recall the pseudospectrum was defined as

$$\mathbf{x}_n = |x_n| e^{i(\delta_{xn} - \delta_{bn})}$$

and therefore,

$$\text{Dynamo } = \sum_n |\mathbf{x}_n||\mathbf{y}_n| \frac{1}{2} \cos(\text{phase}(\mathbf{x}_n) - \text{phase}(\mathbf{y}_n)). \tag{5.2.1}$$

5.3 Comparison

Comparison of Figures 5.1 and 5.2 shows the agreement between these two methods. Figure 5.1 shows a published result using the total dynamo measurement of equation 5.1.1. Figure 5.2 is done using the pseudospectral technique and calculating the contributions of individual modes, as in equation 5.2.1. It is noteworthy that these measurements were taken by different probes, in different plasmas, and at different poloidal angles.

The decomposition into modes shows that the contribution from $m = 0$ modes is small, while the $m = 1$ modes contribute nearly the entire poloidal Hall dynamo EMF. This result was previously unexpected since these modes are not resonant in the edge. In contrast, DEBS simulation shows that the $v \times B$ dynamo in this region is dominated by $m = 0$ modes.

Note that these measurements were optimized for m=0 modes (in terms of phase histograms, etc.), and are only analyzed up through $n = 8$, so this modal dynamo measurement may be incomplete. The main motivation for this comparison has been to benchmark these measurements with a previous result, lending some confidence to the method.

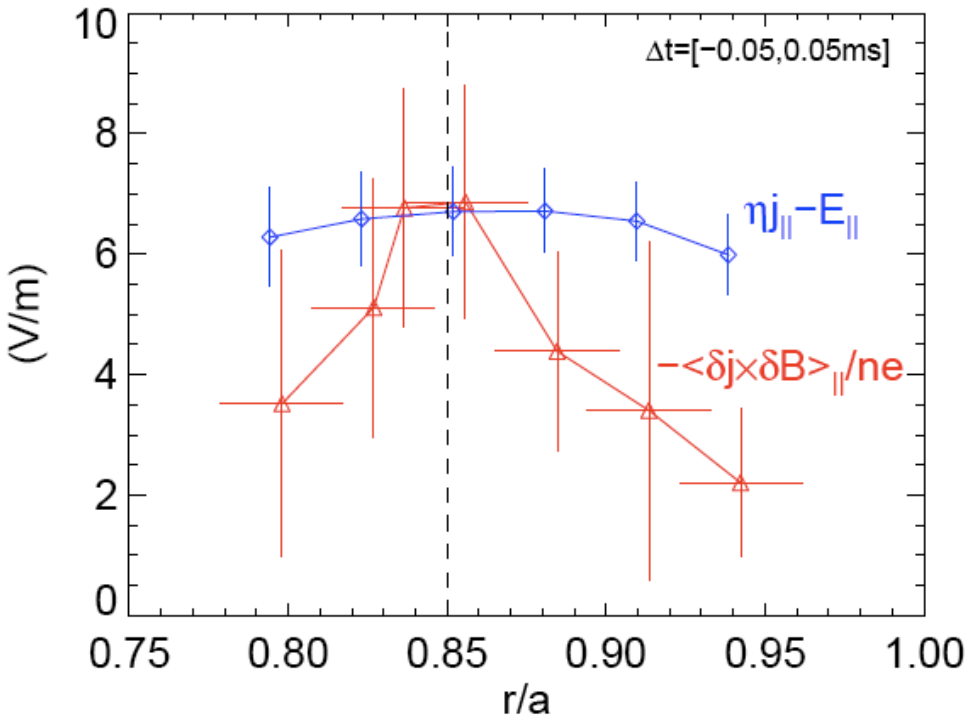

Figure 5.1: Total dynamo published by Kuritsyn et. al.[2] using the method of Equation 5.1.1. The direction of the Hall dynamo, $J \times B$, is negative in the right handed coordinate system (or upward at the outboard edge).

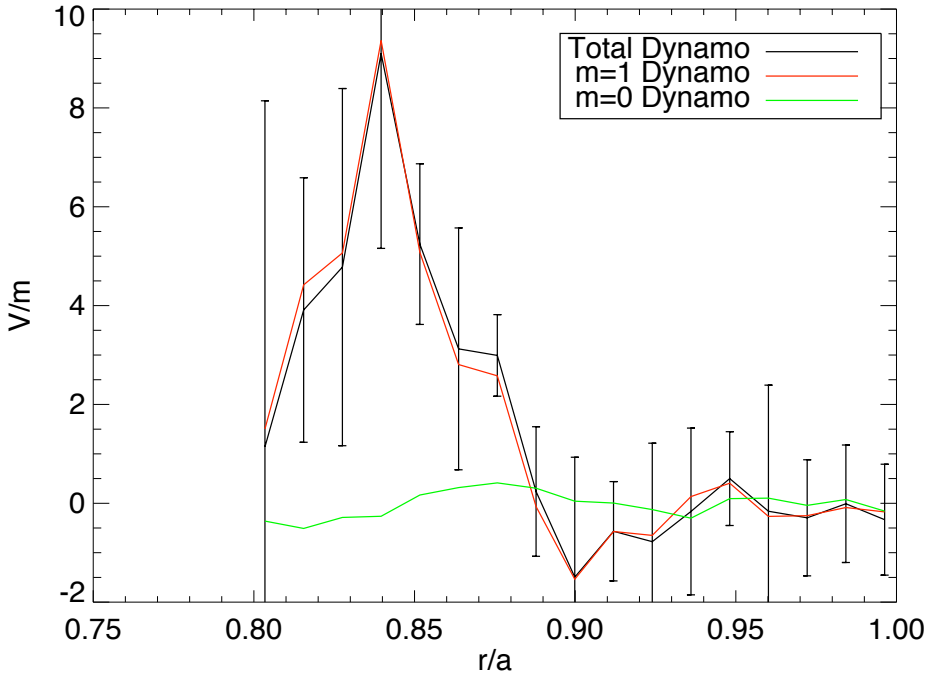

Figure 5.2: Hall dynamo calculated on a mode-by-mode basis using the pseudospectrum of Equation 3.5.1. This method clearly indicates that the dynamo terms are dominated by the $n = 5 - 8$ modes (which are assumed to be $m = 1$). This measurement is reported as $-(J \times B)$ in the right handed coordinate system, to be consistent with Figure 5.1.

5.4 References

[1] H. A. B. Bodin and A. A. Newton, "Reversed-field-pinch research," *Nuclear Fusion*, vol. 20, no. 10, pp. 1255–1324, 1980.

[2] A. Kuritsyn, G. Fiksel, A. Almagri, S. Prager, J. S. Sarff, and T. Tharp, "Measurements of the hall dynamo in the reversed field pinch edge during reconnection events," *16th IEEE International Pulsed Power Conference*, vol. 1, pp. 20–23, 2007.

Chapter 6: Ohm's Law

Magnetic reconnection is governed by Faraday's law of induction, $\partial B/\partial t = -\nabla \times E$, which relates the amount of reconnecting flux to the presence of an electric field. This, in turn, is governed by Ohm's law, which determines the value of the electric field. In resistive MHD, Ohm's law takes the form $E = \eta J - v \times B$, which allows reconnection on a resistive time scale.

A more sophisticated Ohm's law can be derived from the electron and ion equations of motion. Roughly speaking, addition of these two equations will produce the plasma momentum balance equation, while subtraction results in the generalized Ohm's law,

$$E + v \times B - \eta J - \frac{1}{ne} J \times B + \frac{1}{ne} \nabla \cdot P - \frac{m_e m_i}{\rho_M e^2} \frac{\partial J}{\partial t} = 0,$$

where v is the ion velocity, n is the electron density, and P is the pressure tensor (see, for example, reference [1] for details). Since this form is derived from treating ions and electrons independently, it is referred to as the two-fluid generalized Ohm's law.

In this Chapter, several terms of the generalized Ohm's law are examined. In section 6.1, I show that Ohm's law can be treated on a mode-by-mode basis; section 6.2 explains how I calculate terms using magnetic probe measurements; section 6.3 discusses nonlinear contributions; and section 6.4 discusses measurement results, which show that the Hall term is large, and therefore a two-fluid description is needed to describe reconnection in MST plasmas.

Some notational difficulties arise in this Chapter, so I want to introduce a new variable to represent magnetic field at the wall. In this Chapter, the nth magnetic mode at the wall will be described by

$$\text{Magnetic field at the wall } = |\b_n| \cos(m\theta + n\phi - \delta_{\b_n}).$$

6.1 Generalized Ohms Law for a Single Mode

The generalized Ohm's law can be evaluated for a single mode. This single mode behavior can be extracted using toroidal array data. We define the complex quantity

$$\mathfrak{B}_n \equiv B_n - iB_n^\dagger = |\mathfrak{b}_n| e^{-i(m\theta + n\phi - \delta_{\mathfrak{b}})}$$

where $|\mathfrak{b}_n|$ and $\delta_{\mathfrak{b}_n}$ are the amplitude and phase of the nth magnetic mode at the wall. We multiply and integrate over θ and ϕ (i.e. a flux surface) to pick out a single mode.

$$\oint \mathfrak{B}_n (E + v \times B - \eta J + \cdots) dA = 0$$

For notational convenience we will rewrite Ohm's law as a sum of generic terms,

$$\oint \mathfrak{B}_n (R + S + T + \cdots) dA = 0$$

The first term is

$$\oint \mathfrak{B}_n(R) dA = \oint \left(|\mathfrak{b}_{n'}| e^{-i(m'\theta + n'\phi - \delta_{\mathfrak{b}})} \right) \left(\sum_n \frac{1}{2} |r_n| e^{i(m\theta + n\phi - \delta_r)} \right) dA$$

$$= \frac{1}{2} \sum_n \delta(n', n) |\mathfrak{b}_{n'}| |r_n| e^{i(\delta_{\mathfrak{b}_{n'}} - \delta_{r_n})}$$

$$= \frac{1}{2} |\mathfrak{b}_n| |r_n| e^{i(\delta_{\mathfrak{b}} - \delta_r)},$$

and other terms are treated similarly. Therefore

$$\frac{|\mathfrak{b}_n|}{2} \left(|r_n| e^{-i(\delta_{r_n} - \delta_{\mathfrak{b}_n})} + |s_n| e^{-i(\delta_{s_n} - \delta_{\mathfrak{b}_n})} + |t_n| e^{-i(\delta_{t_n} - \delta_{\mathfrak{b}_n})} + \cdots \right) = 0. \tag{6.1.1}$$

This procedure picks out the nth mode of each term; thus, we can legitimately talk about satisfying the Generalized Ohm's Law for a single mode. Furthermore, we can divide by $|\not{b}_n|/2$ to reduce this to

$$\mathbf{r}_n + \mathbf{s}_n + \mathbf{t}_n + \cdots = 0 \tag{6.1.2}$$

in which each term is simply the pseudospectrum of the quantity of interest.

6.2 Calculation of Ohm's Law Terms

Using only measurements of the magnetic field, we can calculate many of the terms in Ohm's Law. We start with a single-mode measurement the magnetic field, $\vec{B}_{m,n}$, and thus we know it's derivatives:

$$\frac{1}{r}\frac{\partial B}{\partial \theta} = \frac{1}{r}\frac{\partial}{\partial \theta}|b_n|e^{i(m\theta+n\phi)}e^{-i\delta_{b_n}} = \frac{im}{r}B$$

$$\frac{\partial B}{\partial z} = \frac{1}{R}\frac{\partial}{\partial \phi}|b_n|e^{i(m\theta+n\phi)}e^{-i\delta_{b_n}} = \frac{in}{R}B$$

A radial profile of magnetic measurements is required to find radial derivatives (and radial integrals) of B.

6.2.1 Br

Measurement of B_r has proven to be difficult, due to its small amplitude and high susceptibility to noise. However, we can use the more reliable measurements of B_t and B_p in conjunction with $\nabla \cdot B = 0$ to accurately calculate B_r.

$$\nabla \cdot \vec{B} = \frac{1}{r}\frac{\partial}{\partial r}rB_r + \frac{1}{r}\frac{\partial B_\theta}{\partial \theta} + \frac{1}{R}\frac{\partial B_\phi}{\partial \phi} = 0$$

$$B_r = -\frac{1}{r}\int r\left(\frac{im}{r}B_\theta + \frac{in}{R}B_\phi\right)dr$$

Since $B_r = 0$ at the conducting wall,

$$B_r(r) = -\frac{1}{r}\int_a^r r'\left(\frac{im}{r'}B_\theta + \frac{in}{R}B_\phi\right)dr'$$

6.2.2 η J

To calculate the resistive term, ηJ, we use the Spitzer resistivity,

$$\eta = \frac{\pi e^2 m^{\frac{1}{2}} \ln \Lambda}{(4\pi\epsilon_0)^2 (kT_e)^{\frac{3}{2}}}$$

For the data presented, we have used $\eta_{||} = 4.25 \times 10^{-6} \Omega m$, corresponding to $Z_{\text{eff}} = 3$, $n_e = 10^{19} m^{-3}$, and $T_e \approx 60eV$ as measured by a Langmuir probe near the reversal surface.

J is calculated directly from the curl of B.

$$\nabla \times B = \mu_0 J$$

$$J = \begin{pmatrix} \frac{1}{\mu_0} \frac{im}{r} B_\phi - \frac{1}{\mu_0} \frac{in}{R} B_\theta \\ \frac{1}{\mu_0} (\frac{in}{R} B_r - \frac{\partial}{\partial r} B_\phi) \\ \frac{1}{\mu_0} \left(\frac{1}{r} \frac{\partial}{\partial r} (r B_\theta) - \frac{im}{r} B_r \right) \end{pmatrix} \begin{matrix} \hat{r} \\ \hat{\theta} \\ \hat{\phi} \end{matrix}$$

6.2.3 $\frac{\partial}{\partial t}$J

The electron inertia term

$$\frac{m_e m_i}{\rho_M e^2} \frac{\partial J}{\partial t} \approx 3.5 \times 10^{-12} \frac{\partial J_\theta}{\partial t},$$

has also been calculated, but is experimentally seen to be negligibly small compared to other Ohm's Law terms and will be neglected from now on.

6.2.4 J $\times$ B

The Hall term can now be calculated.

$$J \times B = \begin{vmatrix} \hat{r} & \hat{\theta} & \hat{\phi} \\ J_r & J_\theta & J_\phi \\ B_r & B_\theta & B_\phi \end{vmatrix} = \begin{pmatrix} J_\theta B_\phi - J_\phi B_\theta \\ J_\phi B_r - J_r B_\phi \\ J_r B_\theta - J_\theta B_r \end{pmatrix} \begin{matrix} \hat{r} \\ \hat{\theta} \\ \hat{\phi} \end{matrix}$$

This is discussed further in section 6.3.

6.2.5 $\nabla\cdot\mathbf{P}$

For the diagonal components of the pressure tensor, we are interested in pressure gradients in the poloidal direction with $m = 0$,

$$\left(-\frac{m_i}{2\rho_M e}\nabla P\right)_\theta = \left(\frac{m}{R}\right)\left(-\frac{m_i}{2\rho_M e}P\right)_\theta = 0.$$

If off diagonal pressure tensor terms are important, then it is possible to have a significant contribution to the parallel Ohm's Law from pressure. Unfortunately, these effects are not currently possible to measure.

6.2.6 E

To calculate the electric field, we must rely heavily upon the assumption that $m = m(n)$. In particular, we assume that the $n = 1$ mode is purely $m = 0$. Then, any electrostatic field is

$$E_{\text{electrostatic}} = \nabla\Phi = \frac{im}{r}\Phi = 0$$

The remaining electromagnetic field can be calculated from Faraday's Law.

$$-\frac{\partial\vec{B}}{\partial t} = \nabla\times\vec{E}$$

$$-\frac{\partial\vec{B}}{\partial t} = \begin{pmatrix} \frac{im}{r}E_\phi - \frac{in}{R}E_\theta \\ \\ \frac{in}{R}E_r - \frac{\partial}{\partial r}E_\phi \\ \\ \frac{1}{r}\frac{\partial}{\partial r}(rE_\theta) - \frac{im}{r}E_r \end{pmatrix} \begin{matrix} \hat{r} \\ \\ \hat{\theta} \\ \\ \hat{\phi} \end{matrix}$$

Since m = 0,

$$E_\theta = -\frac{iR}{n}\frac{\partial B_r}{\partial t}.$$

There is a sticky point to consider here, though. We are using a measurement of B, and applying a pseudospectrum correlation technique to extract the $n = 1$ mode of this measurement (designated by $\{B\}$). This correlation does not commute with $\partial/\partial t$, so we must decide whether to calculate E using

$$E = \left\{ \frac{\partial}{\partial t} B \right\} \text{ or } E = \frac{\partial}{\partial t} \{B\} .$$

In the lab frame, the n=1 Ohm's Law is satisfied by the first definition; however, we believe that the physics of reconnection is best described by the second, which represents Ohm's Law in the frame of the rotating n=1 island. Since we are interested in studying the physics of island formation, we have chosen to use the second option,

$$E = \frac{\partial}{\partial t} \{B\} .$$

This choice brings with it the implication that the equilibrium v_ϕ is approximately zero in our chosen reference frame. This is important when considering the $v \times B$ terms in Ohm's law.

6.2.7 Error in Ohm's Law

Section 3.9 gives the error, $\sigma(\mathbf{x}_n)$, of the measured pseudospectral quantities. The error for the Ohm's Law quantities can be found through error propagation formulae:

$$\begin{aligned}\sigma(B_r) &= \frac{in}{R}\sigma\left(\int_a^r B_\phi dr\right) = \frac{in}{R}\sigma\left(\sum_{i=1}^{i_{max}} B_\phi \delta r\right) = \frac{in}{R\sqrt{i_{max}}}\sum_{i=1}^{i_{max}} \sigma\left(B_\phi\right)\delta r \\ &\approx \frac{in}{R\sqrt{i_{max}}}(i_{max})\sigma\left(B_\phi\right)\left(\frac{a-r}{i_{max}}\right) = \frac{in}{\sqrt{i_{max}}}\left(\frac{10}{200}\right)\sigma(B_\phi)\end{aligned}$$

$$\sigma(E) = \frac{iR}{n}\sigma\left(\frac{\partial B_r}{\partial t}\right) = \frac{iR}{n}2\sigma\left(B_r\right)$$

$$\sigma\left(\vec{J}\right) = \begin{pmatrix} \frac{1}{\mu_0}\frac{im}{r}\sigma(B_\phi) - \frac{1}{\mu_0}\frac{in}{R}\sigma(B_\theta) & \hat{r} \\ \frac{1}{\mu_0}(\frac{in}{R})\sigma(B_r) - \frac{1}{\mu_0}\sigma(\frac{\partial}{\partial r}B_\phi) & \hat{\theta} \\ \frac{1}{\mu_0}\sigma(\frac{\partial}{\partial r}B_\theta) - \frac{im}{r}\sigma(B_r) & \hat{\phi} \end{pmatrix}$$

$$\text{where } \sigma(\frac{\partial}{\partial r}B) = \frac{\sqrt{\sigma^2(B)|_{r1} + \sigma^2(B)|_{r2}}}{\Delta r} \approx \frac{\sqrt{2}}{.1}\sigma(B)$$

$$\sigma(\eta) = \sigma(\alpha_0 T^{-\frac{3}{2}}) = \alpha_0 \frac{3eV}{2}\sigma(T)^{-\frac{5}{2}} \text{ where } \alpha_0 = 5\times 10^{-4}\Omega m(eV^{3/2})$$

$$\sigma(J\times B) = (J\times B)\left(\frac{\sigma(J)}{J} + \frac{\sigma(B)}{B}\right)$$

6.3 Nonlinear contributions to a mode

Directly measured quantities that appear in the single mode Ohm's law can be calculated using the pseudospectrum; however, we do not always start with a measurement of the term of interest. In particular, multiplicative terms such as $(J\times B)_n$ present an interesting case. When J and B are separately measured, then multiplied for comparison in the single mode Ohm's law, we must consider all modes in the system to find the correct contribution.

The nth mode of the Hall term is itself formed from two terms, the linear and nonlinear contributions. The linear contribution is formed from the product of an equilibrium term and a

fluctuation term.

$$\begin{aligned} \text{linear } (J \times B)_{\theta,n} &= (J_{\phi,0}B_{r,n} + J_{\phi,n}B_{r,0}) - (J_{r,0}B_{\phi,n} + J_{r,n}B_{\phi,0}) \\ &= J_{\phi,0}B_{r,n} - J_{r,n}B_{\phi,0} \end{aligned}$$

In these measurements, the linear Hall term has been measured to be nonzero (5 V/m) but out-of-phase with the $n = 1$ mode X-point.

The nonlinear contribution to the Hall term is formed from a 3-wave interaction. For example, the $(m, n) = (0, 1)$ mode can have a Hall term contribution formed from the "beat frequency" of the (1,6) mode and the (1,7) mode.

$$\begin{aligned} J_6 \times B_7 &= |J_6|\cos(\theta + 6\phi - \delta_{J6}) \times |B_7|\cos(\theta + 7\phi - \delta_{B7}) \\ &= \frac{1}{2}|J_6||B_7|\left(\underline{\cos(1\phi + \delta_{J6} - \delta_{B7})} + \cos(2\theta + 13\phi - \delta_{B7} - \delta_{J6})\right) \end{aligned}$$

The underlined term has the spatial form of a (0,1) mode, but only a portion of this wave couples to the (0,1) mode of the plasma. This coupling is determined by a fraction, γ, called the bicoherence of the three waves, so that

$$\left(J_{(1,6)} \times B_{(1,7)}\right)_{(0,1)} = \frac{\gamma}{2}|J_6||B_7|\cos(\phi + \delta_{J6} - \delta_{B7}) \tag{6.3.1}$$

where γ (a complex number with magnitude less than unity) will be called the pseudospectral bicoherence. To correctly account for the Hall contribution, we must sum the linear Hall terms as well as all the possible nonlinear Hall terms.

6.3.1 Pseudospectral Bicoherence

In section 6.1, we calculated the pseudospectral Ohm's Law, using

$$\mathfrak{B}_n \equiv |\mathfrak{b}_n| e^{-i(m\theta + n\phi - \delta_{\mathfrak{b}})}$$

$$\left(\mathbf{r}_n + \mathbf{s}_n + \mathbf{t}_n + \cdots\right) = \frac{\oint \mathfrak{B}_n \left(R + S + T + \cdots\right) dA}{|\mathfrak{b}_n|/2}$$

We now explicitly apply this operation to the nonlinear Hall Term:

$$\text{pseudo}\left(\widetilde{J} \times \widetilde{B}\right)_n = \frac{\oint \mathfrak{B}_n (\widetilde{J} \times \widetilde{B}) dA}{|\mathfrak{b}_n|/2}.$$

Specifically, we consider the contribution of $J_{1,6} \times B_{1,7}$ to the $(0,1)$ mode, which we then generalize to include all modes. We start with the single mode contributions of J and B. We assume that these are known quantities, found by measuring J and B and calculating their individual pseudospectra.

$$J_6 = \frac{1}{2}|j_6|\left(e^{i(1\theta+6\phi-\delta_{j_6})} + e^{-i(1\theta+6\phi-\delta_{j_6})}\right)$$

$$B_7 = \frac{1}{2}|b_7|\left(e^{i(1\theta+7\phi-\delta_{b_7})} + e^{-i(1\theta+7\phi-\delta_{b_7})}\right)$$

$$J_6 \times B_7 = \frac{|j_6||b_7|}{4}\left(e^{i(2\theta+13\phi-\delta_{j_6}-\delta_{b_7})} + e^{i(-1\phi-\delta_{j_6}+\delta_{b_7})} + e^{i(1\phi+\delta_{j_6}-\delta_{b_7})} + e^{i(-2\theta-13\phi+\delta_{j_6}+\delta_{b_7})}\right)$$

As before, averaging picks out the $n = 1$ contribution and removes the spatial dependence:

$$\text{pseudo}\left(\widetilde{J} \times \widetilde{B}\right)_{(0,1)} = \frac{< |\mathfrak{b}_1| e^{-i(1\phi-\delta_{\mathfrak{b}_1})} |j_6||b_7| \left(e^{i(2\theta+13\phi-\delta_{j_6}-\delta_{b_7})} + \cdots\right) >}{2|\mathfrak{b}_1|}$$

$$= \frac{< |\mathfrak{b}_1||j_6||b_7| e^{-i(1\phi-\delta_{\mathfrak{b}_1})} \left(e^{i(-1\phi-\delta_{j_6}+\delta_{b_7})} + e^{i(1\phi+\delta_{j_6}-\delta_{b_7})}\right) >}{2|\mathfrak{b}_1|}$$

$$= \frac{< |\mathfrak{b}_1||j_6||b_7| e^{i(\delta_{\mathfrak{b}_1}+\delta_{j_6}-\delta_{b_7})} >}{2|\mathfrak{b}_1|}$$

Next, we take advantage of certain ensemble constants: Recall that a basic assumption of

the pseudospectral method is that any pseudospectral quantity is proportional to its corresponding magnetic mode at the wall. Therefore, J_6 is proportional to $\mathscr{b}_6$, and $[|j_6|]/[|\mathscr{b}_6|]$ is a constant of the ensemble, which can be pulled out of the flux surface average; similarly $[|b_7|]/[|\mathscr{b}_7|]$ is an ensemble constant. Finally, we recognize (as we did in the derivation of the pseudospectrum) that this expression is supposed to represent typical ensemble behavior, not be applied to every shot, so we replace the quantity $|\mathscr{b}_1|$ with its ensemble average, $[|\mathscr{b}_1|]$.

$$\begin{aligned}\text{pseudo}\left(\widetilde{J}\times\widetilde{B}\right)_{(0,1)} &= \frac{<|\mathscr{b}_1||j_6||b_7|e^{i(\delta_{\mathscr{b}_1}+\delta_{j_6}-\delta_{b_7})}>}{2|\mathscr{b}_1|}\\ &= \frac{[|j_6|][|b_7|]\left[|\mathscr{b}_1||\mathscr{b}_6||\mathscr{b}_7|\left(e^{i(\delta_{\mathscr{b}_1}+\delta_{j_6}-\delta_{b_7})}\right)\right]}{2[|\mathscr{b}_1|][|\mathscr{b}_6|][|\mathscr{b}_7|]}\end{aligned}$$

We can also pull out the pseudospectral phase (another ensemble constant) using the identity

$$e^{i(\delta_{\mathscr{b}_1}+\delta_{j_6}-\delta_{b_7})}=e^{i(\delta_{j_6}-\delta_{\mathscr{b}_6})}e^{-i(\delta_{b_7}-\delta_{\mathscr{b}_7})}e^{i(\delta_{\mathscr{b}_1}+\delta_{\mathscr{b}_6}-\delta_{\mathscr{b}_7})}.$$

Then, we are left with

$$\begin{aligned}\text{pseudo}\left(\widetilde{J}\times\widetilde{B}\right)_{(0,1)} &= \frac{|j_6||b_7|e^{i(\delta_{j_6}-\delta_{\mathscr{b}_6})}e^{-i(\delta_{b_7}-\delta_{\mathscr{b}_7})}\left[|\mathscr{b}_1||\mathscr{b}_6||\mathscr{b}_7|\left(e^{i(\delta_{\mathscr{b}_1}+\delta_{\mathscr{b}_6}-\delta_{\mathscr{b}_7})}\right)\right]}{2[|\mathscr{b}_1|][|\mathscr{b}_6|][|\mathscr{b}_7|]}\\ &= \frac{\mathbf{j}_6^*\mathbf{b}_7\left[|\mathscr{b}_1||\mathscr{b}_6||\mathscr{b}_7|\left(e^{i(\delta_{\mathscr{b}_1}+\delta_{\mathscr{b}_6}-\delta_{\mathscr{b}_7})}\right)\right]}{2[|\mathscr{b}_1|][|\mathscr{b}_6|][|\mathscr{b}_7|]}\end{aligned}$$

Comparing to the intuitively derived form of the nonlinear Hall term (equation 6.3.1), we find

that the bicoherence is apparently given by

$$\gamma = \frac{\left[|\not{b}_1||\not{b}_6||\not{b}_7|\left(e^{i(\delta_{\not{b}_1}+\delta_{\not{b}_6}-\delta_{\not{b}_7})}\right)\right]}{[|\not{b}_1|][|\not{b}_6|][|\not{b}_7|]}$$

or

$$\mathrm{Re}\,(\gamma) = \frac{\left[|\not{b}_1||\not{b}_6||\not{b}_7|\cos\left(\delta_{\not{b}_1}+\delta_{\not{b}_6}-\delta_{\not{b}_7}\right)\right]}{[|\not{b}_1|][|\not{b}_6|][|\not{b}_7|]}$$

$$\mathrm{Im}\,(\gamma) = \frac{\left[|\not{b}_1||\not{b}_6||\not{b}_7|\sin\left(\delta_{\not{b}_1}+\delta_{\not{b}_6}-\delta_{\not{b}_7}\right)\right]}{[|\not{b}_1|][|\not{b}_6|][|\not{b}_7|]}$$

which is to be used in conjunction with

$$\mathbf{j}_6^*\mathbf{b}_7 = |j_6|e^{i\delta_{\mathbf{j}_6}}|b_6|e^{-i\delta_{\mathbf{b}_7}} = |j_6||b_7|\left(\cos(\delta_{\mathbf{j}_6}-\delta_{\mathbf{b}_7})+i\sin(\delta_{\mathbf{j}_6}-\delta_{\mathbf{b}_7})\right)$$

This *pseudospectral bicoherence* has a similar form to bicoherence found in the literature [2], which was previously used to calculate three wave interaction coupling coefficients in MST [3].

Finally, we remember to include contributions from all appropriate modes:

$$\mathrm{pseudo}\left(\widetilde{J}\times\widetilde{B}\right)_{(0,1)} = \sum_{p,q}\left(\mathbf{j}_p^*\mathbf{b}_q+\mathbf{j}_p\mathbf{b}_q^*\right)\gamma(1,p,q)$$

where only modes which satisfy the selection criteria $p-q=1$ are considered.

6.4 Measurement Results

Figures 6.1 and 6.2 show the values of the measured $n=1$ Ohm's law terms versus time and radius respectively, using the sign convention $E=\eta J+J\times B+$ (unmeasured terms). Without measurement

of the remaining terms ($v \times B$ and the off-diagonal elements of $\nabla \cdot P$), experimental verification of the balance of Ohm's law is not available; however, we may still draw significant physics conclusions from the available terms.

The measured electric field is bipolar in time. It can be observed in Figure 6.6 that island growth and decay is associated with positive and negative electric field, respectively. This is consistent with the interpretation that the poloidal electric field may be taken as a measurement of the reconnection rate. The positive sign of the Hall term at this location therefore indicates that it is a driver for the mode, while the negative sign of ηJ indicates this term is a mode damping term.

The measured ordering, $J \times B >> E > \eta J$ implies that two fluid effects are an important contributor to the dynamics of this reconnection. The Hall term is dominated by the contributions from the (1,6) and (1,7) coupling and the (1,7) and (1,8) coupling, indicating that it is the nonlinear coupling of these unstable core modes which provides the nonlinear Hall drive.

The observation of nonlinear terms driving a bipolar electric field is also supported by nonlinear simulation. In linear single-fluid tearing mode theory, the reconnection electric field is balanced by ηJ; but in single-fluid nonlinear calculation using DEBS [4], we have observed large, positive nonlinear $v \times B$ contributions analogous to the nonlinear Hall term seen in the experiment. Since DEBS is a single fluid code, the Hall term is not included in Ohm's law. Nonetheless, we see some interesting similarities between DEBS nonlinear sawtooth behavior and the measured results. Figure 6.3 shows Ohm's law versus time for DEBS, analogous to Figure 6.1 of the data. Figure 6.4 shows the magnetic mode amplitude superimposed on the same Ohm's law electric field. From these Figures, it can be seen that the nonlinear $v \times B$ term dominates the mode growth phase of the sawtooth, while ηJ–smaller in amplitude, but with a longer duration–is responsible for mode decay. Figure 6.5 shows the radial profile of these Ohm's law terms at a time of peak electric field, in analogy to the data presented in Figure 6.2.

A parallel can be drawn between this mode-driving nonlinear Hall term and the Hall dynamo term, which contributes to the plasma equilibrium. Indeed, we could describe the measured nonlinear Hall term as the $n = 1$ component of the total Hall effect, while the Hall dynamo is the $n = 0$ component of the same effect. Perhaps it is not surprising, then, that the large mode-driving

Hall contribution to the $n = 1$ Ohm's Law is in the same radial region as the previously reported Hall dynamo term. This parallel allows us to draw some intuition from the results of dynamo studies in simulation, which help to justify the comparison of single fluid nonlinear simulation with measurements of the two-fluid Hall term. Specifically, recent two fluid simulations at finite beta have shown that as the ion skin depth is increased relative to the resistive layer, there is a smooth transition from MHD dynamo drive to Hall dynamo drive near a resonant surface [5]. This is an indication that the two fluid drive, $\frac{1}{ne}J \times B - v \times B = v_e \times B$, may be thought of as a generalized case of single fluid $v \times B$ drive; and that we might expect single-fluid and two-fluid simulated plasmas to be qualitatively similar, even in a nonlinear regime.

Though these measurements alone have strong physics implications, it is much more satisfying to measure, or at least get a sense for, the balance of Ohm's law. In an effort to understand the final balance, we have made a preliminary attempt to measure the $v \times B$ term using a spectroscopic probe. Figure 6.7 shows the radial balance of Ohm's law including the linear term $v_{r0} \times B_{t1}$. This term appears to be the dominant applicable term, though more data is required to verify this completely. This data is consistent with a balanced Ohm's law.

6.5 Conclusions

These results highlight an underappreciated feature of magnetic reconnection: In linear reconnection, both $v \times B$ and $J \times B$ are zero at the X-point, leaving only ηJ to balance the electric field, while nonlinear reconnection can have significant contributions to Ohm's law at the X-point from either $v \times B$ as seen in DEBS or from $J \times B$ as observed in the experiment. These nonlinear effects are also intrinsically related to the problem of describing magnetic reconnection in three dimensions: In our measurements, the nonlinear drive comes from core modes which have a different axis of symmetry than the driven mode. Some nonlinear effects, such as the change in shape of the magnetic islands due to overlapping $m = 0$ modes as discussed in Chapter 4, can be captured by a purely 2-D description, but the measured driving term cannot. These Hall effects allow reconnection to be driven directly by the beating of the $n = 6, 7, 8$ core modes, while in DEBS these modes are driven by a "cascade" effect, where core modes beat together and contribute to edge modes, but the $n = 1$ drive is primarily through other edge mode beating ($n = 2, 3, 4$) rather than directly from core mode beating.

The implications of these findings reinforce the need to include Hall physics in future modeling of the RFP, as is the current trend in computational studies, since the subtle effects that Hall terms can have on reconnection may prove to have a global impact on plasma dynamics .

6.6 References

[1] D. R. Nicholson, *Introduction to Plasma Theory.* John Wiley and Sons Inc, 1983.

[2] Y. C. Kim and E. J. Powers, "Digital bispectral analysis and its applications to nonlinear wave interactions," *IEEE Transactions on Plasma Science*, vol. PS-7, p. 120, June 1979.

[3] J. S. Sarff, "Nonlinear coupling of tearing fluctuations in the madison symmetric torus," *Phys. Fluids B*, vol. 5, no. 2540, 1993.

[4] D. D. Schnack *et al. Computer Physics Communications*, vol. 43, no. 17, 1986.

[5] J. King, "Numerical studies of two-fluid tearing and dynamo in a cylindrical pinch," *Bull. Am. Phys. Soc.*, vol. 54, p. TP8.71, November 2009.

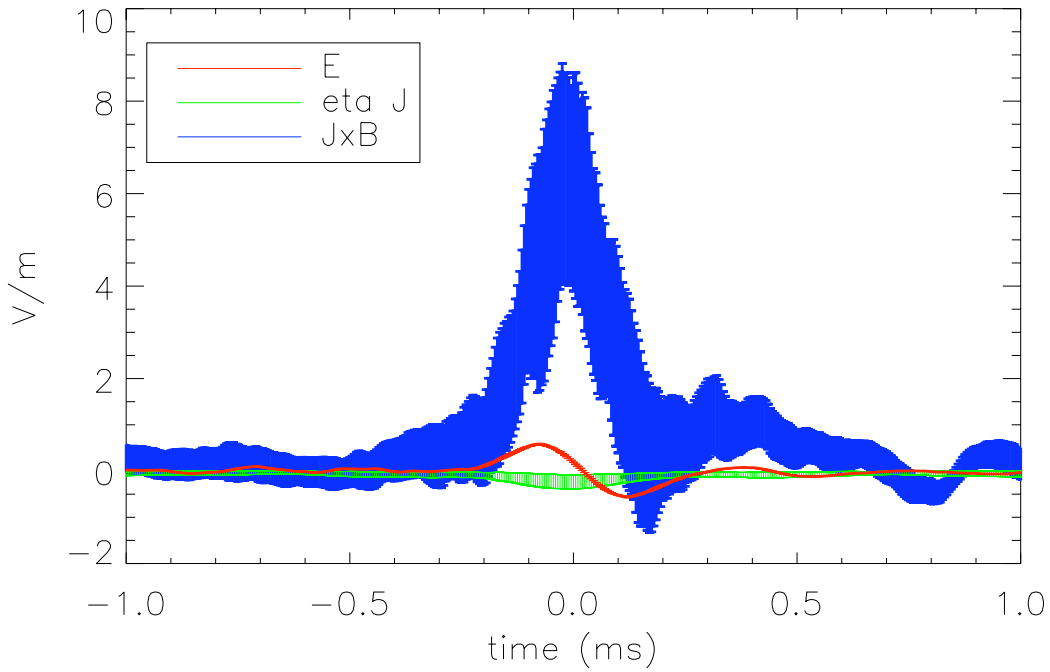

Figure 6.1: Ohm's law terms versus time, evaluated for the $n = 1$ mode at a depth of $7cm$ from the wall and the phase (toroidal angle) associated with the X-point of $n = 1$ reconnection. The sign convention here is $E = \eta J + J \times B +$ unmeasured terms.

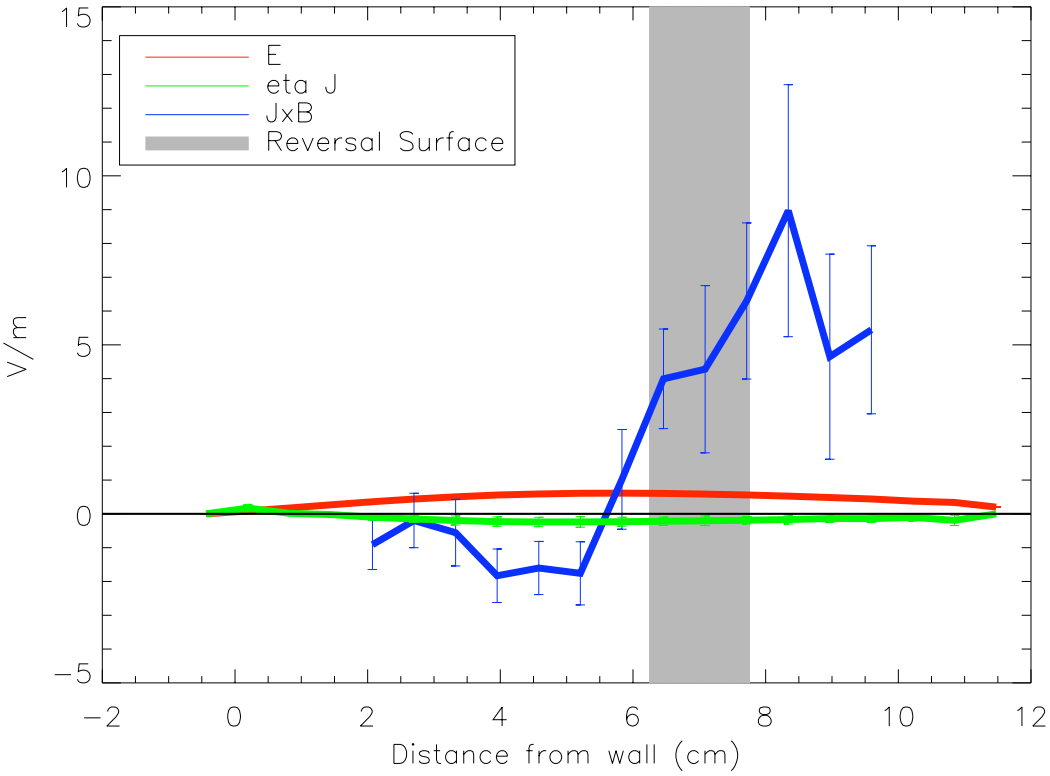

Figure 6.2: Ohm's law terms for the $n = 1$ mode as a function of radius, evaluated at $t = -0.075$ (the approximate time of peak electric field) and the phase (toroidal angle) associated with the X-point of $n = 1$ reconnection. The sign convention here is $E = \eta J + J \times B +$ unmeasured terms.

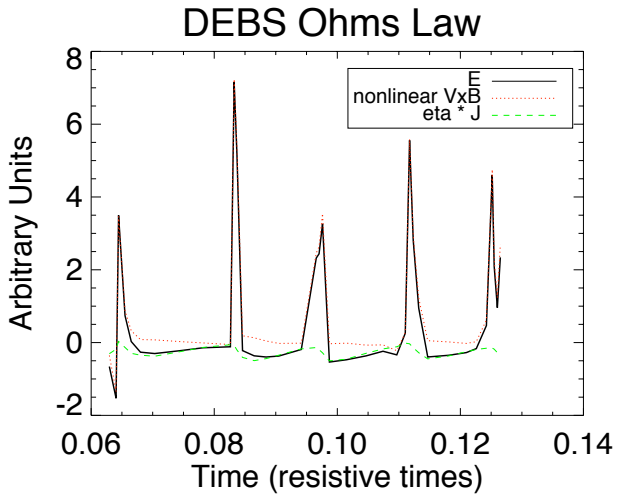

Figure 6.3: Ohm's law terms versus time from DEBS, analogous to Figure 6.1 for data. $v \times B$ (red), ηJ (green), and the the total electric field, $E = \eta J - v \times B$ (black) are plotted for multiple quasi-periodic sawtooth events.

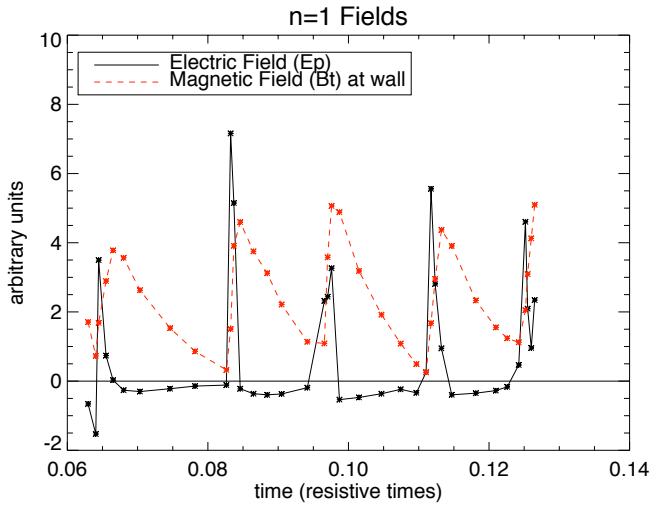

Figure 6.4: DEBS normalized electric field and normalized toroidal field at the wall. It can be seen that the E_p (black) approximately corresponds to the time derivative of B_t (red) as expected.

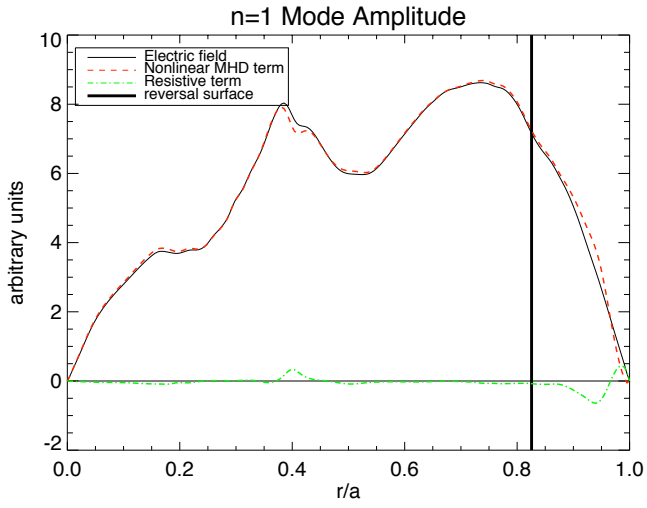

Figure 6.5: Profile of Ohm's law in DEBS at time of peak electric field, analogous to Figure 6.2. The amplitude of the nonlinear $-v \times B$ (red), linear ηJ (green), and total electric field, $E = \eta J - v \times B$ (black) are plotted.

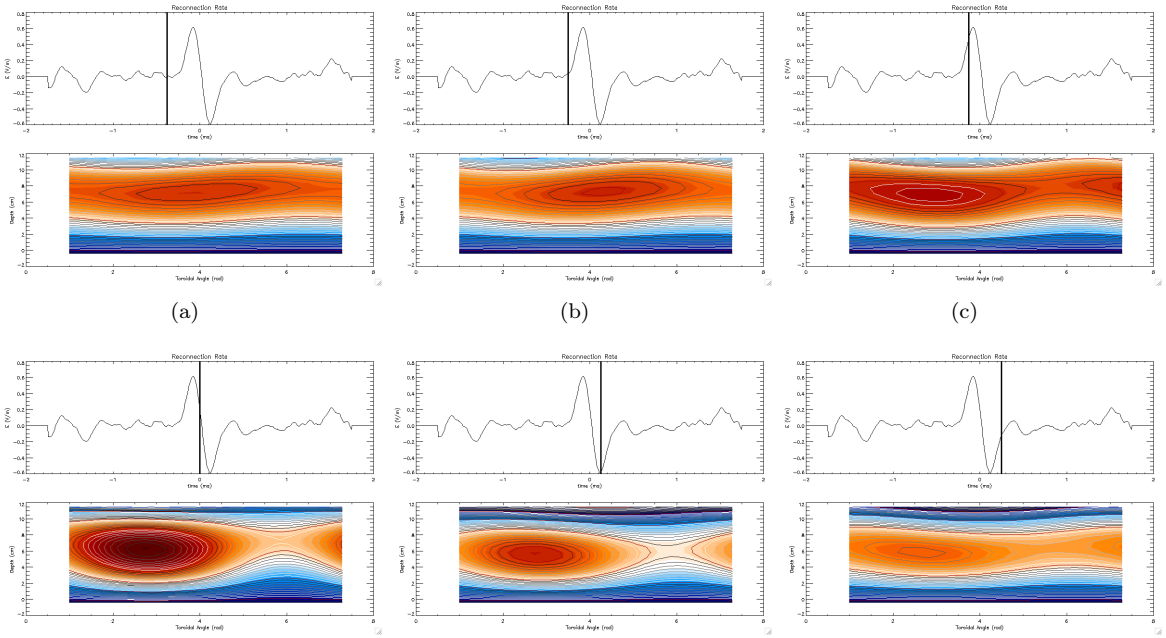

(a) (b) (c)

(d) (e) (f)

Figure 6.6: Snapshots in time of island formation and decay. The top trace of each panel is the $n = 1$ electric field evaluated at the X-point versus time (the same as in Figure 6.1). The lower Figure of each panel is the toroidal flux associated with $n = 1$ (as in Figure 4.4).

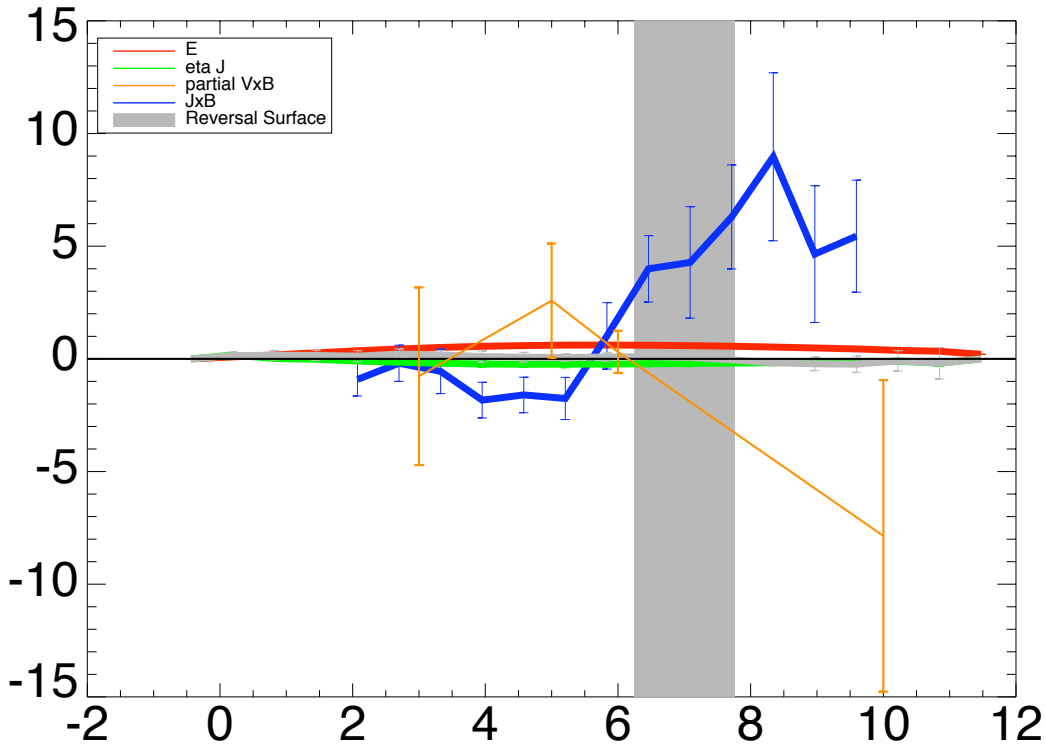

Figure 6.7: Ohm's law versus radius, including a partial measurement of $v \times B$. Experimental verification of the balance of Ohm's law may not be far away. The sign convention here is $E =$ "Partial $v \times B$" $+\eta J + J \times B +$ unmeasured terms.

Chapter 7: Summary

7.1

In summary, I have developed probes and a spatial Fourier mode correlation method to measure the magnetic field associated with reconnection near the reversal surface of the Madison Symmetric Torus. We discovered that nonlinear processes dominate these reconnection events, and that two-fluid physics is important.

7.2 Magnetic Probes

Insertable probes were designed, characterized, and used to measure poloidal and toroidal magnetic fields. The radial component was inferred from $\nabla \cdot B = 0$. A simple probe-perturbation model was developed to understand why the measured $n = 1$ radial field did not behave as expected. The results of this investigation have lead to the development of a new probe which can use the discovered effect to measure local plasma current density.

7.3 Pseudospectrum

I have developed a new correlation method, and I have attempted to describe it using a uniform presentation, clearly identify the intrinsic assumptions, and make contact with previous methods. This pseudospectral analysis uses only spatial domain mode decomposition and treats each time point (relative to the sawtooth crash) independently. It has been tested in detail, and its performance has been characterized.

The method presented has two major shortcomings: the helicity of the mode must be known *a-priori*, and the method can only be applied to data which naturally has a random phase distribution. To address the first shortcoming, it is possible to directly measure the mode helicity using a poloidal and toroidal array in combination; or to use a double Fourier method, in which signals are decomposed in both k-space and frequency to distinguish counter-propagating modes. To address the second

shortcoming, it is possible to develop a weighted average in which sawteeth that contain modes with underrepresented phase values are given more weight; though for simple measurements it is often easier to simply take more data until the phase histogram naturally fills out.

7.4 Magnetic Field Measurements

The magnetic field, measured using probes and pseudospectral analysis, has been compared with linear and nonlinear theory. Comparison with linear theory in both cylindrical and toroidal geometries highlights the stronger than previously expected effects of toroidicity. The next steps on the experimental front lie in taking similar measurements at new θ positions to further verify the toroidal eigenmode calculations.

In both experiment and nonlinear simulation (DEBS), m=0 modes align in an interesting way to produce a coherent structure on the reversal surface. This result suggests interesting reconnection physics may be present, such as current sheet elongation or filamentation and plasmoid development. The details of the separatrix at high n value are not accessible through current experimental methods; however, since there is good agreement with simulation for low n structures, the detailed nature of this reconnection should be investigated further using RFP simulation.

7.5 Dynamo

The Hall dynamo was measured mode-by-mode using the pseudospectrum, which reproduces an old result in a new way. Similarity between the new and old measurements gives a measure of confidence in the applicability of pseudospectral methods. Additionally, it can be seen from the new method that the Hall dynamo is dominated by contributions from core modes. This unanticipated result provides yet another mechanism through which core and edge physics can be coupled and deserves further attention and investigation from the RFP community. This result is consistent with an emerging picture that, in general, $J \times B$ effects behave similarly to $v \times B$ effects, but might be more radially broad, allowing a stronger interaction between radially separated modes.

7.6 Ohm's Law

Ohm's law can be evaluated for a single mode, but the analysis must include contributions from other modes through three-wave interactions. Several of the terms of Ohm's law are evaluated from the magnetic field measurements and supplemental probe measurements. It is seen that the nonlinear Hall term is a large contributor to the balance of Ohm's Law and is a mode-driving term. Further, this term comes primarily from the $n = 6 - 8$ modes, which are resonant in the core, indicating that this is a mechanism through which core modes and edge modes are coupled.

These findings are partially supported by simulation through analogous behavior of the sawtooth modeled in DEBS, though some interesting discrepancies remain. In particular, the $n = 1$ mode in DEBS is driven primarily by $m = 0$ activity, while the Hall term measured in the experiment provides a mechanism for direct $m = 1$ drive. A more complete understanding may be accessible in the future by comparison with nonlinear, two-fluid, toroidal simulation.

7.7 Remarks

It is my hope that the results of this thesis will inspire new ideas and influence future research on MST. Pseudospectral analysis is a powerful tool, with great untapped potential. Until now, it has been difficult to use without a deep understanding and significant "re-invention of the wheel" with each new analysis. I hope that my work will make this tool easier to access for those wishing to study fluctuations. Reconnection in MST is a rich topic, with much left to discover. In the reconnection community there is still a disconnect between accessible reconnection experiments, which are typically single reconnection sites constrained to simple geometries, and the astrophysical reconnection processes, which are free to develop multiple reconnection sites in very complicated geometries. In MST, we have a self-organized plasma, undergoing nature-like nonlinear reconnection in a complicated geometry, but which is also very accessible to measurement and extremely repeatable. This is a rare opportunity to bridge the vast gap between the terrestrial and astrophysical understandings of plasma physics.

Appendix A: User's Guide to Pseudospectra

The *pseudospectrum* is a quantity constructed to reflect the physical fluctuations associated with a measurement. This Appendix is intended help the user calculate the pseudospectrum of his or her signal with relative ease.

Coordinate System

The toroidal array information is recorded using the Left-Handed Coordinate System (see 1.4) . It is easiest to calculate the pseudospectrum in this coordinate system, then transform to the Right-Handed Coordinate System before making any physics calculations. If you are measuring a vector quantity, make sure your signal is recorded in the LHCS.

You will also need to calculate the quantity

$$\Delta_n = n\phi_{probe} + m\left(\theta_{probe} - 241\right).$$

for each mode of interest, using a negative value for m and a positive value for n. The values ϕ_{probe} and θ_{probe} represent the angles associated with whatever port hole you are using for the measurement.

Sawtooth Averaging

You will need to input several quantities into the sawtooth averaging software to calculate the pseudospectrum. These are

- Your signal, X.
- The mode structure, calculated from toroidal array information, and evaluated at your position:

$$\begin{aligned} B_n &\equiv |b_n|\cos(\Delta_n - \delta_{b_n}) \\ B_n^\dagger &\equiv |b_n|\sin(\Delta_n - \delta_{b_n}) \end{aligned}$$

Typically, B_t is used for $m = 0$ modes and B_p is used for $m = 1$ modes. It is possible to separate a given n mode into it's m content by evaluating both: the $m = 1$ content is found from correlation with B_p, while the $m = 0$ content is found by subtracting the $m = 1$ content from the correlation with B_t.

- The mode amplitudes, $|b_n|$. If you want to save computation time, you can leave these out and calculate them afterward from

$$[|b_n|^2] = \sqrt{2}[(b_n \cos(\Delta_n - \delta_b))^2] = \sqrt{2}[(b_n \sin(\Delta_n - \delta_b))^2].$$

  Alternatively, you can calculate all three of these terms and use this relation as a quick check of the validity of the random phase approximation.

- If you intend to add multiple modes together, you will also need the relative phases, constructed here to use $n = 1$ as the reference:

$$\delta_{\text{rel}} \equiv \delta_{n'} - n'\delta_1$$

  Remember that it is *never* useful to find the average of a phase (it is always zero, if the random phase approximation is valid), but rather you should average $\cos\delta_{\text{rel}}$ and $\sin\delta_{\text{rel}}$ then after averaging take

$$\text{average } \delta_{\text{rel}} = \tan^{-1}(- < \sin\delta_{\text{rel}} >, < \cos\delta_{\text{rel}} >)$$

Pseudospectra

Calculate the pseudospectrum, $\mathbf{x}_n$, from

$$\text{Re}(\mathbf{x}_n) = \frac{2[X(point)|b_n|\cos(\Delta_n - \delta_{bn})]}{[|b_n|]}$$

$$\text{Im}(\mathbf{x}_n) = \frac{-2[X(point)|b_n|\sin(\Delta_n - \delta_{bn})]}{[|b_n|]}$$

Remember that you can extract $[AB]$ from dxdxav$[*, a, b]$ with the indices (a and b) in increasing order. If you plan to compare multiple modes, convert everything to the same phase basis: Any

modes calculated by correlating with B_p should be phase shifted by π to agree with the basis of B_t.

Finally, transform your measurement into the Right-Handed Coordinate System before you make any calculations. This means multiplying all poloidal components of vector quantities by -1. If you already converted to the same phase basis, you don't need to do any further phase corrections. In the RHCS, derivatives and physical quantities are evaluated with both m and n positive.

Mode Summation

To get a physical quantity as a function of poloidal and toroidal angle, θ and ϕ, you can take a sum of modes using

$$X(\phi) =< X > + \sum_{n=1}^{N} |\mathbf{x}_n| \cos\left(n\phi + m\theta - \delta_{\mathrm{rel},n} - \mathrm{phase}(\mathbf{x}_n)\right).$$

Here, $\delta_{\mathrm{rel},1} = 0$ since $n = 1$ was used as the reference mode, and $< X >$ is the equilibrium ($n = 0$) component of the measured quantity. This physical quantity in the plasma is referenced the modes such that $\phi = 0$ is defined to be the (moving) location at which B_t is a maximum for the reference mode. In other words, this picture is in the moving reference frame of the $n = 1$ mode, however the other modes are free to rotate with respect to $n = 1$. Experimentally, however, they are often phase-locked to one another such that this reference frame is stationary to all modes.

Comparison with Other Formulations

The great difficulty of pseudospectral analysis comes from developing a uniform presentation in which all sign, amplitude, phase, and complex notation conventions are clearly defined and self-consistent. Nearly every equation in this Chapter can be and has been written with a different convention–I have tried to present a clear and uniform convention, which is also consistent with historical MST conventions, though this is not completely possible since historical MST conventions are *not* self-consistent. In this section, I will try to make contact with some of the common ideas and notation used in the past.

Correlation analysis has a long tradition in MST, and some useful computational tools have been developed. The method presented so far is different from the "standard" method, which uses a software package named st_corr. The fundamental difference is that here we have used the toroidal array and a 90-degree phase shift of each mode in k-space to calculate the fictitious $B^{\dagger}$ quantity introduced on page 23, while the st_corr method uses a 90-degree phase shift of each frequency in a time-based Fourier transform.

In this st_corr method, correlation is done at different frequencies, so instead of directly choosing the sign of n, the frequency of each signal is assigned to be positive. In this case, we assume the wave is of the form

$$\text{perturbation} \sim e^{i\left(\vec{k}\cdot\vec{r}-\omega t\right)}.$$

The sign of ω is chosen to be positive, and the sign of n is then determined by the direction of wave propagation. The wave vector is given by the traditional expression,

$$\vec{k} = \left(\frac{m}{r}\hat{\theta} + \frac{n}{R}\hat{\phi}\right).$$

Overall, the difference in these two formulations is almost trivial, but can lead to great confusion if it isn't understood. Both methods still have the critical shortcoming that they rely on *a priori* knowledge of the helicity of the mode. In order to observe the helicity of the mode directly, we must either use a combination of poloidal and toroidal arrays (whereas these methods use only the toroidal array), or we must use a more involved mathematical analysis in which the spatial and temporal

spectra are combined into a complex double Fourier transform analysis. Both of these analyses have been performed on MST, and the helicity has been verified to be that which is expected, at least in the case of standard plasmas. Highly reversed plasmas are expected to produce edge resonant $m = 1$ modes with helicity opposite to the core modes, and these have been detected in OFCD plasmas using the complex double Fourier analysis.

There are a number of situations in which one might expect the space-domain pseudospectrum to perform better: This method truly processes each time point (relative to the sawtooth crash) independently, while st_corr uses the time behavior in the FFT. Therefore, this method can be used to analyze a non-rotating mode, while st_corr requires mode rotation, and may even formally require that mode rotation be faster than the timescale of the sawtooth dynamics. Nevertheless, numerical comparisons of the two methods give very similar results in terms of outputs and reliability.

A check of the methods can be found by calculating the spectrum using a single toroidal array coil (i.e. using one coil of the toroidal array as the "probe") as we did in section 3.10. It is seen in Figure A.1 that three calculation methods correctly reproduce the average mode amplitude for the $n = 1$ mode for a large ensemble of about 1000 similar sawteeth. Each of these methods employs at least part of the st_corr software. This software package identifies the time at which each sawtooth event peaks, labels this as $t = 0$, and performs ensemble averages at each relative time. Three outputs of note are 1) dxav$[t, i]$, the average of the ith signal as a function of time, 2) dxdxav$[t, i, k]$, the average of signal i times signal k as a function of time, and 3) corr$[t, i, k]$, the correlation of signals i, and k.

The three calculations considered are

1) Average mode amplitude, $<$ n1_mode_amp $>$

2) Pseudospectral mode amplitude, amp($\mathbf{x}_1$)

3) a construction taken from the st_corr outputs,
$\sqrt{2}\left(\sqrt{\text{dxdxav[*,coil,coil]}}\right)$ corr[*, n1_cos, coil]

The first calculation–considered to be the "correct" mode amplitude–is simply the ensemble average of the mode amplitude recorded by the toroidal array. The second is calculated according to Equation 3.5.1. The third method above is the "traditional" method which uses the outputs of the st_corr software.

We can derive the proper construction for method 3 by examining the definition of "correlation." According to previous work on MST[1][2][3][4], correlation is given by

$$\gamma \equiv \frac{\left(< \widetilde{X}\widetilde{Y} >^2 + < \widetilde{X}\widetilde{Y}^\dagger >^2 \right)^{1/2}}{\left\| \widetilde{X} \right\| \left\| \widetilde{Y} \right\|}.$$

For pseudospectral analysis, we are meant to take the correlation of the signal and the mode: $\gamma(\widetilde{X}, \widetilde{Y} = B_{n,\cos})$. Take caution that some authors call this unitless quantity the "pseudospectrum," while this thesis uses a presentation in which the pseudospectrum has the same units as X. The amplitude of the mode is given by the construction

$$\sqrt{2}\gamma \left\| \widetilde{X} \right\| = \frac{2\left(< \widetilde{X}\widetilde{Y} >^2 + < \widetilde{X}\widetilde{Y}^\dagger >^2 \right)^{1/2}}{|\widetilde{Y}|}$$

Here, a factor of $\sqrt{2}$ appears because we switched from the root-mean-square, $\left\| \widetilde{Y} \right\|$, to the amplitude, $|\widetilde{Y}|$, on the right hand side.

It is important to note that the st_corr method has a number of issues that I have not resolved. In particular, the phase reconstruction and sometimes even the amplitude reconstruction are not acceptable for certain ensembles. In principle, it should not matter if you use the cosine or the sine part of the toroidal array signal for correlation because these two terms are supposed to be perfectly correlated. In practice it *does* matter which you use, and the correct choice seems to depend on the toroidal angle of your measurement. If this is not carefully accounted for, *st_ corr produces a poor reconstruction for certain toroidal angles!* (Further, st_corr can occasionally produce a correct reconstruction before correcting for the probe's toroidal location by including Δ_n, but produce a poor reconstruction when this simple correction is added.) This issue may be resolved by using a combination of sine and cosine terms to find a reconstruction, or may have been resolved by others in

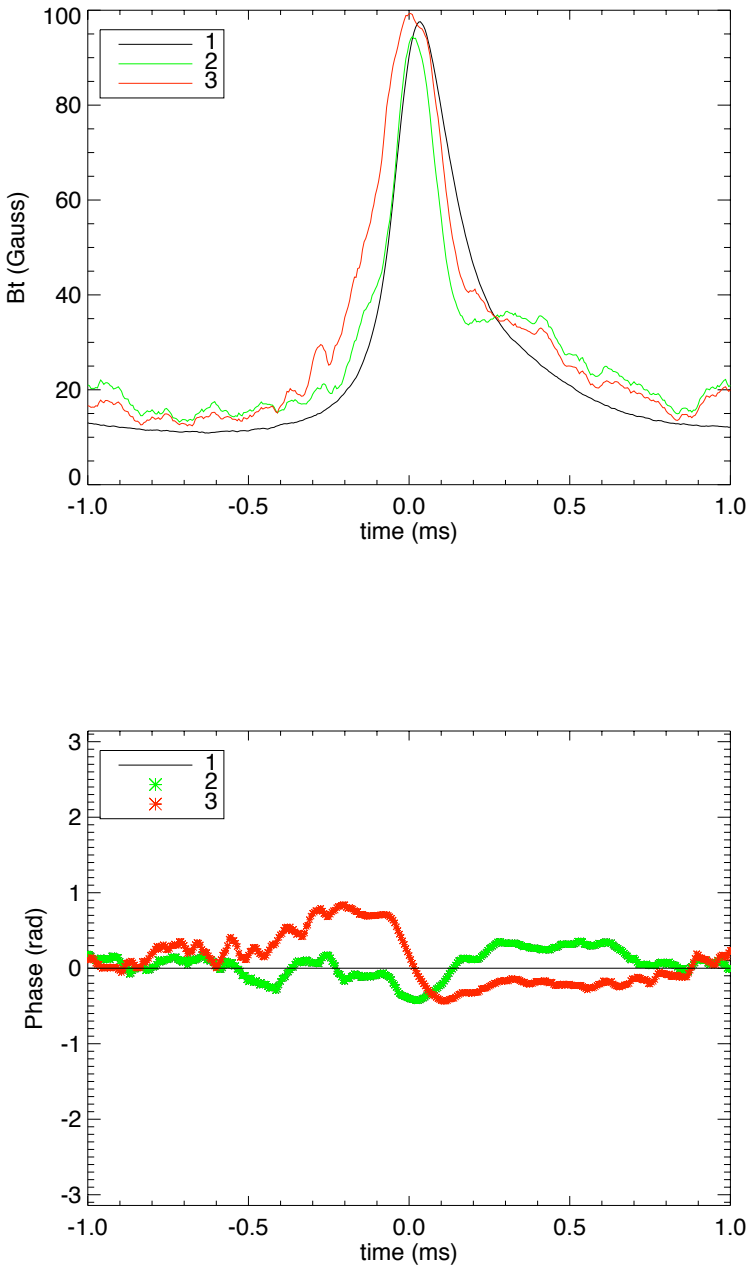

Figure A.1: Comparison of the three methods for $n = 1$. For this ensemble, the three amplitudes match relatively well and the phase is close to zero for both the pseudospectrum and st_corr methods.

a different way. This thesis does not use this method to calculate the pseudospectrum, but I mention these issues here for future users who might wish to try.

References

[1] P. W. Fontana, *Ion Dynamics and the Dynamo in the Edge of the Reversed-Field Pinch.* PhD thesis, University of Wisconsin-Madison, 1999.

[2] A. Almagri and H. Ji, "Sawteeth averaging procedure." Internal MST documentation, 1995.

[3] D. Craig, "Magnetic mode analysis in mst." Internal MST documentation, 2005.

[4] D. Craig, "User's guide to sawtooth ensemble routines." Internal MST documentation, 2002.

Appendix B: Comprehensive set of Magnetic Profiles

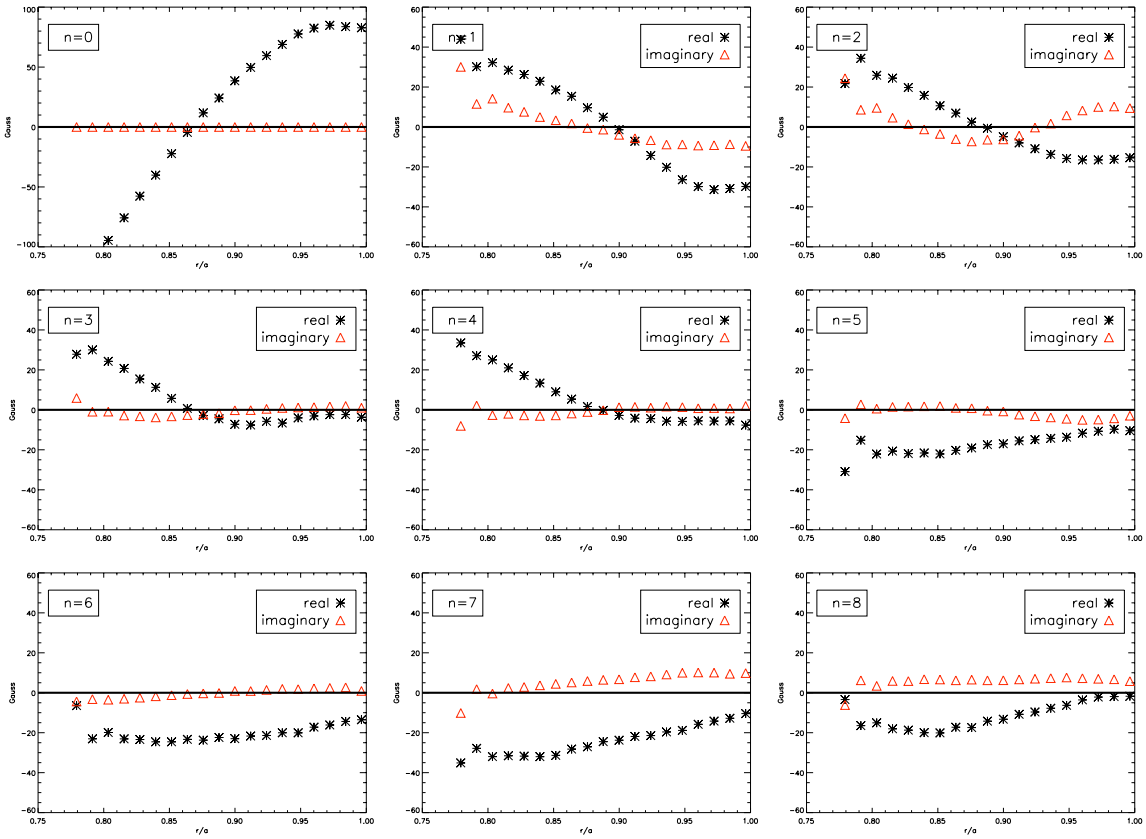

Figure B.1: Toroidal Field, B_ϕ

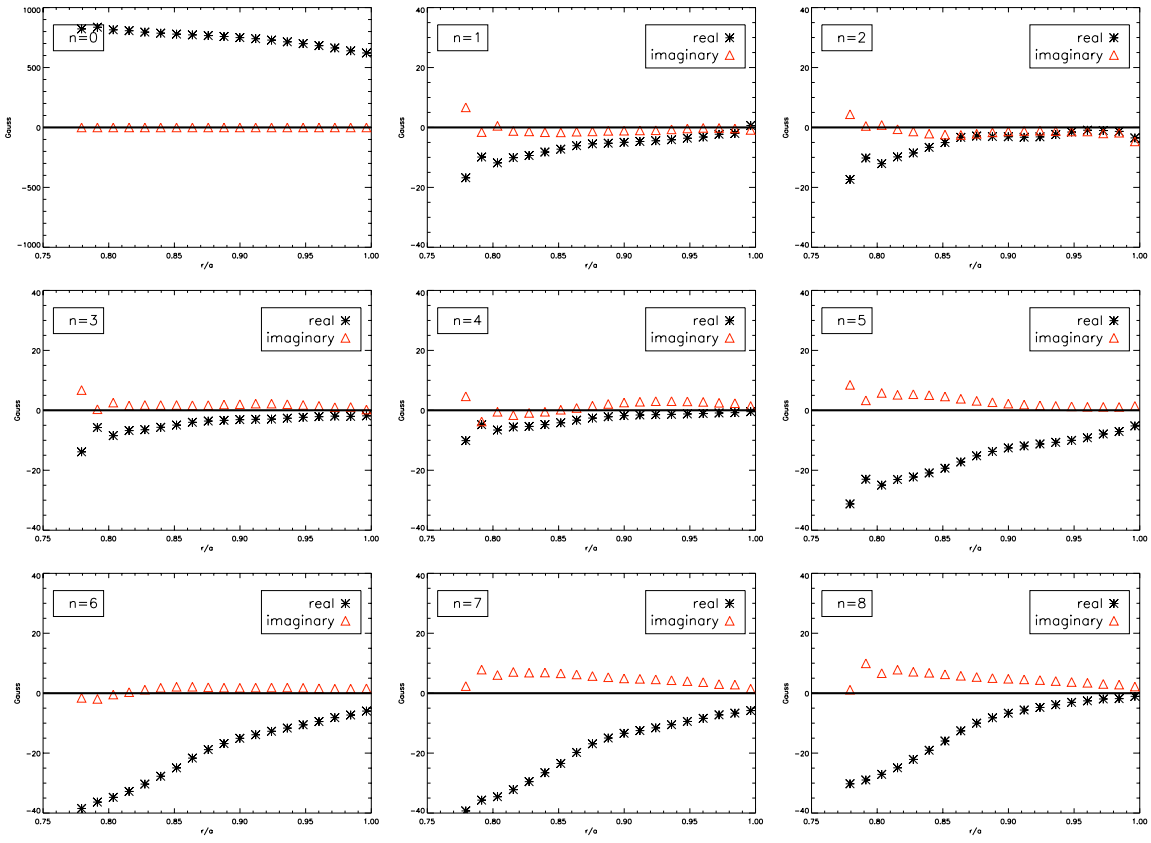

Figure B.2: Poloidal Field, B_θ

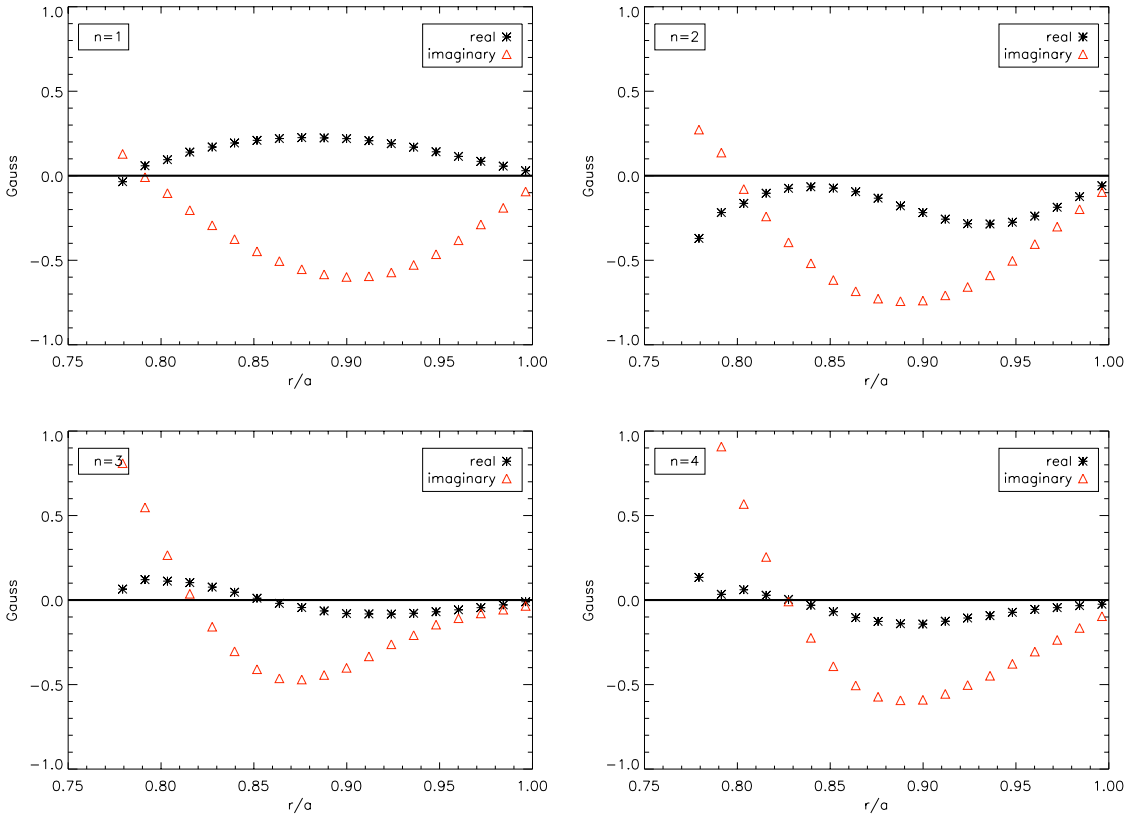

Figure B.3: Radial Field, B_r, for m=0 modes, B_ϕ, calculated from $\nabla \cdot B = 0$.

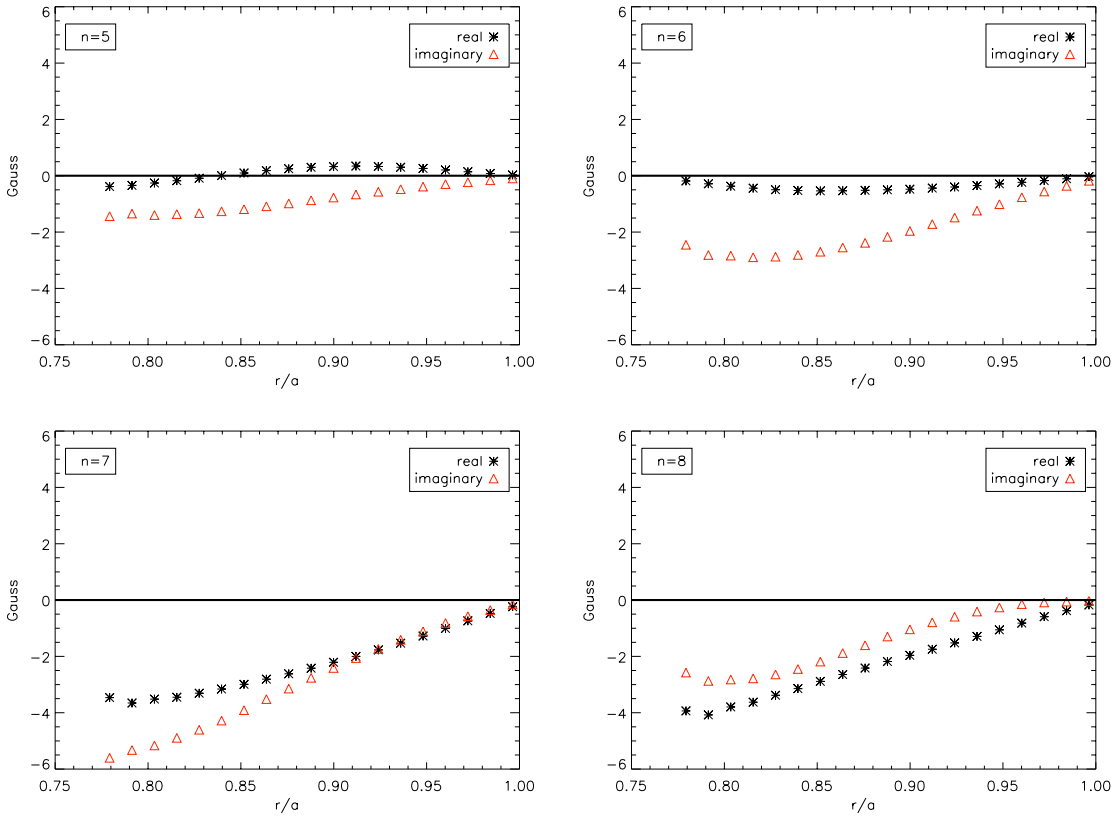

Figure B.4: Radial Field, B_r, for m=1 modes, B_ϕ, calculated from $\nabla \cdot B = 0$.

Appendix C: Supplemental Derivations

C.1 Measuring the effective area of a magnetic coil

The voltage on a coil of wire subjected to a magnetic field is given by Faraday's Law,

$$V = -\frac{d\Phi}{dt},$$

where $\Phi = \vec{B} \cdot \vec{A}$ is the magnetic flux through the coil. To measure the effective area, A, of the magnetic probe coil, it is placed inside a Helmholtz coil which is driven sinusoidally at a particular frequency.

$$B(t) = B_0 \sin(\omega t)$$

We measure the current driven through the Helmholtz coil, I_0, by measuring the voltage drop across a resistor in series with the Helmholtz coil windings. The Helmholtz coil has a known characteristic constant which relates this current to the magnetic field produced,

$$k = \frac{B_0}{I_0},$$

which can be calculated from the geometry of the Helmholtz coil, or measured directly with a Hall probe. The Helmholtz coil used for calibration has the following characteristics:

k	0.56 G / A
R	100 Ω
positive V_r	B is in $+\hat{z}$ direction

To ensure that the B_r pickup coil has the correct polarity, it is set up to measure positive field, and the voltage waveforms are verified to have the property that V_c is the negative derivative of V_r.

By measuring the two voltages involved, V_r across the resistor and V_c across the pickup coil, we can calculate the effective area as follows.

$$\begin{aligned} B(t) &= B_0 \sin(\omega t) \\ &= kI \sin(\omega t) \\ &= k\left(\frac{V_r}{R}\right)\sin(\omega t) \end{aligned}$$

$$\begin{aligned} V_c &= -\frac{d\Phi}{dt} \\ &= -A\dot{B} \\ &= -A\omega B_0 \cos(\omega t) \\ &= -A\omega k\left(\frac{V_r}{R}\right)\cos(\omega t) \end{aligned}$$

Therefore, we plot

$$\frac{V_c}{V_r} = \frac{Ak}{R}\omega = \frac{Ak}{R}2\pi f$$

as a function of frequency. The effective area is given by its slope, m:

$$\begin{aligned} \frac{V_c}{V_r} &= mf \\ A &= \frac{mR}{2\pi k}. \end{aligned}$$

C.2 Calibrating a magnetic probe triplet

To calibrate the relative alignments of a magnetic triplet, we use the magnetic field of MST with the probe in place, and take three specific calibration shots:

- Bt only shot
- Bt only shot with probe rotated 90 degrees
- Plasma shot

In this section, we use the following notation:

$$
\begin{aligned}
B_\phi &= \text{True toroidal B} \\
B_\theta &= \text{True poloidal B} \\
\text{Bt0} &= \text{Bt coil measurement in Bt only shot} \\
\text{Bp0} &= \text{Bp coil measurement in Bt only shot} \\
\text{Bt90} &= \text{Bt coil measurement in Bt only shot with 90 degree rotation} \\
\text{Bp90} &= \text{Bp coil measurement in Bt only shot with 90 degree rotation} \\
\text{Bt\_plasma} &= \text{Bt coil measurement in plasma shot} \\
\text{Bp\_plasma} &= \text{Bp coil measurement in plasma shot}
\end{aligned}
$$

We assume that the coils start with the following polarity. These assumptions must be verified before the alignment matrix is calculated.

Bt0	positive
Bp90	negative
Bp_plasma	negative

If the data is not of the correct polarity for Bt0 or Bp_plasma, we multiply it by -1 to put it in the correct (right-handed) coordinate system. This calibration is derived for the probe rotation (± 90) which results in a negative Bp90, but an equivalent derivation could be done using the opposite probe rotation.

The coordinate system is defined according to the following diagram.

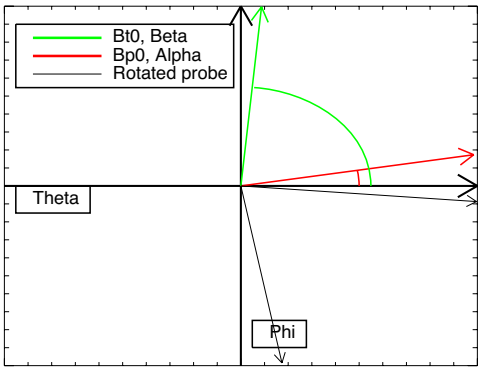

We can make the following statements based on geometry:

$$\begin{aligned} Bt0 &= \sin(\beta)B_\phi \\ Bt90 &= \sin(\beta - 90)B_\phi = -\cos(\beta)B_\phi \\ Bp0 &= \sin(\alpha)B_\phi \\ Bp90 &= \sin(\alpha - 90)B_\phi = -\cos(\alpha)B_\phi \end{aligned}$$

Next, we find α and β. Since $\cos^{-1}$ has principle values between 0 and π, we'll use this to find β. On the other hand, $\sin^{-1}$ has principle values between $-\pi/2$ and $\pi/2$, so we'll use that for α.

$$\begin{aligned} \beta &= \cos^{-1}\left(\frac{-Bt90}{B_\phi}\right) \\ \alpha &= \sin^{-1}\left(\frac{Bp0}{B_\phi}\right) \end{aligned}$$

Now that we have the angles, we calculate the appropriate corrections. During a real shot,

$$\begin{aligned} \text{Bt\_plasma} &= B_\phi \sin\beta + B_\theta \cos\beta \\ \text{Bp\_plasma} &= B_\phi \sin\alpha + B_\theta \cos\alpha \end{aligned}$$

Or, in matrix form:

$$\begin{pmatrix} \text{Bt\_plasma} \\ \text{Bp\_plasma} \end{pmatrix} = \begin{pmatrix} \sin\beta & \cos\beta \\ \sin\alpha & \cos\alpha \end{pmatrix} \begin{pmatrix} B_\phi \\ B_\theta \end{pmatrix}$$

Simply invert the matrix, to find

$$\begin{pmatrix} B_\phi \\ B_\theta \end{pmatrix} = \begin{pmatrix} A_{11} & A_{12} \\ A_{21} & A_{22} \end{pmatrix} \begin{pmatrix} \text{Bt\_plasma} \\ \text{Bp\_plasma} \end{pmatrix}$$

C.3 Total Dynamo

In the particular case of the poloidal component of the hall term, $(J \times B)_\theta$, we can calculate the **total** dynamo. A short derivation follows:

$$\begin{aligned}
\mu_0 < \widetilde{J} \times \widetilde{B} >_\theta &= < (\nabla \times \widetilde{B}) \times \widetilde{B} >_\theta \\
\text{We drop the} \quad &\sim \quad \text{for convenience.} \\
\mu_0 < J \times B >_\theta &= < (\nabla \times B) \times B >_\theta \\
&= - < (\nabla \times B)_r \times B_\phi > \quad + \quad < (\nabla \times B)_\phi \times B_r > \\
&= - < (\frac{\partial}{\partial \theta} B_\phi - \frac{\partial}{\partial \phi} B_\theta) B_\phi > + < \frac{1}{r} \frac{\partial}{\partial r} (r B_\theta - - \frac{\partial}{\partial \theta} B_r) B_r >
\end{aligned}$$

Notice that any quantity which is a complete derivative of θ or ϕ will flux surface average to zero. There are two occurrences of such a quantity,

$$< (\frac{\partial}{\partial \theta} B_r) B_r > = < \frac{1}{2} \frac{\partial}{\partial \theta} B_r^2 > = 0 \qquad \text{and} \qquad < (\frac{\partial}{\partial \theta} B_\phi) B_\phi > = < \frac{1}{2} \frac{\partial}{\partial \theta} B_\phi^2 > = 0$$

Therefore,

$$\mu_0 < J \times B >_\theta \quad = \quad < (\frac{\partial}{\partial \phi} B_\theta) B_\phi > + < \frac{1}{r} \frac{\partial}{\partial r} (r B_\theta) B_r >$$

Notice the following:

$$\begin{aligned}
< B_\theta (\nabla \bullet B) > &= < B_\theta \frac{1}{r} \frac{\partial}{\partial r} (r B_r) > + < B_\theta \frac{\partial}{\partial \theta} \frac{B_\theta}{r} > + < B_\theta \frac{\partial}{\partial \phi} \frac{B_\phi}{R} > \\
&= < B_\theta \frac{1}{r} \frac{\partial}{\partial r} (r B_r) > + < B_\theta \frac{\partial}{\partial \phi} \frac{B_\phi}{R} > \\
\therefore \quad 0 &= < B_\theta \frac{1}{r} B_r > + < B_\theta \frac{\partial}{\partial r} (B_r) > + < B_\theta \frac{\partial}{\partial \phi} \frac{B_\phi}{R} >
\end{aligned}$$

$$< B_\theta(\nabla \bullet B) > + \mu_0 < J \times B >_\theta \;=\; < (\frac{\partial}{\partial \phi} B_\theta) B_\phi > + < \frac{1}{r} \frac{\partial}{\partial r} (r B_\theta) B_r > + < B_\theta \frac{1}{r} B_r > + < B_\theta \frac{\partial}{\partial r} (B_r) > + < B_\theta \frac{\partial}{\partial \phi} \frac{B_\phi}{R} >$$

The first and last terms combine to form $< \frac{1}{R} \frac{\partial}{\partial \phi} (B_\phi B_\theta) >= 0$.

$$\begin{aligned} < B_\theta(\nabla \bullet B) > + \mu_0 < J \times B >_\theta &= < \frac{1}{r} \frac{\partial}{\partial r} (r B_\theta) B_r > + < B_\theta \frac{1}{r} B_r > + < B_\theta \frac{\partial}{\partial r} (B_r) > \\ &= < \frac{1}{r} (B_\theta) B_r > + < \frac{\partial}{\partial r} (B_\theta) B_r > + < B_\theta \frac{1}{r} B_r > + < B_\theta \frac{\partial}{\partial r} (B_r) > \\ &= < \frac{2}{r} B_\theta B_r > + < \frac{\partial}{\partial r} (B_\theta B_r) > \\ &= (\frac{2}{r} + \frac{\partial}{\partial r}) < (B_\theta B_r) > \end{aligned}$$

$$\therefore \quad < \widetilde{J} \times \widetilde{B} >_\theta = \frac{1}{\mu_0} \left(\frac{\partial}{\partial r} + \frac{2}{r} \right) < (\widetilde{B}_\theta \widetilde{B}_r) > \tag{C.3.1}$$

This method was used to calculate the Hall dynamo term in Figure 5.1.

C.4 Field Lines from Toroidal Flux

For the case of two dimensional reconnection in the r, ϕ plane, we can visualize the magnetic fieldlines through a plot of the toroidal flux. To see why, consider

$$\begin{aligned}\vec{B} &= \nabla \times \vec{A} = \begin{vmatrix} \hat{x} & \hat{y} & \hat{z} \\ \partial_x & \partial_y & \partial_z \\ A_x & A_y & A_z \end{vmatrix} \\ &= \hat{x}\left(\partial_y A_z - \partial_z A_y\right) - \hat{y}\left(\partial_x A_z - \partial_z A_x\right) + \hat{z}\left(\partial_x A_y - \partial_y A_x\right)\end{aligned}$$

We consider a system with symmetry in the y direction, $\partial_y = 0$. If we can find a function ψ such that $\vec{B} \cdot \nabla\psi = 0$, then contours of constant ψ will be everywhere parallel to $\vec{B}$, and thus will be a visualization of the magnetic field lines.

$$\vec{B} \cdot \nabla\psi = -\partial_z A_y \partial_x \psi + 0 + \partial_x A_y \partial_z \psi = 0$$

This is satisfied by $\psi = CA_y$ where C is any constant.

Near the edge, toroidal flux is given by

$$\Phi = \int B_\phi r d\theta dr \approx 2\pi a \int B_\phi dr,$$

which has the properties

$$\begin{aligned}\frac{\partial}{\partial r}\Phi &= (2\pi a) B_\phi \\ \frac{\partial}{\partial \phi}\Phi &= (2\pi a)\frac{in}{R}\int B_\phi dr = -(2\pi a) B_r\end{aligned}$$

Where the last equality comes from

$$\nabla \cdot \vec{B} = \frac{\partial}{\partial r} B_r + \frac{in}{R}\int B_\phi = 0$$

$$\therefore B_r = -\int \frac{in}{R} B_\phi dr$$

Choosing $\psi = \frac{1}{2\pi a}\Phi$,

$$\vec{B} \cdot \nabla\psi = B_\phi(-B_r) + B_r(B_\phi) = 0$$

Therefore, contours of toroidal flux represent magnetic field lines.

Equating toroidal flux to A_θ, the relationship between the electric field and reconnection can be expressed in these terms as well.

$$\begin{aligned} \nabla \times \vec{E} &= -\frac{\partial}{\partial t}\vec{B} \\ &= -\frac{\partial}{\partial t}\left(\nabla \times \vec{A}\right) = \nabla \times \left(-\frac{\partial}{\partial t}\vec{A}\right) \\ \therefore \vec{E} &= -\frac{\partial}{\partial t}\vec{A} + \nabla\Phi_{ES} \end{aligned}$$

where Φ_{ES} is any arbitrary function. If we choose to evaluate $\vec{A}$ in the Coulomb gauge, Φ_{ES} can be identified as the electrostatic potential. (This choice means $\nabla \cdot \vec{A} = 0$, which puts constraints on the in-plane components of $\vec{A}$, but these components are unused in this presentation anyway.)

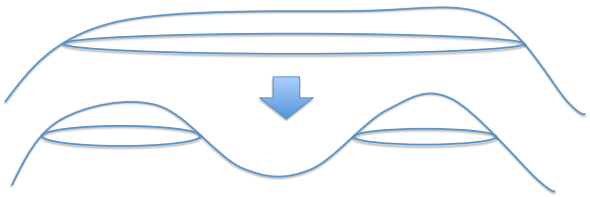

Figure C.1: Cartoon of fieldlines breaking with new local minimum of A_θ

Since fieldlines can be expressed as contours of A_θ, there must exist a new topology when-

ever A_θ has a new local minimum. Therefore, in the absence of an electrostatic field ($\Phi_{ES} = 0$) reconnection occurs wherever E_θ has an instantaneous local maximum (see Figure C.1).

C.5 Supplemental Dynamo information

Examination of the $m = 1$ radial profiles in Figure C.2 hints at the reason for the radial shape of the Hall dynamo contribution. The measured dynamo can be traced back to the details of the B_θ profiles of the modes which dominate this measurement, $n = 7$ and $n = 8$. (Curiously, $n = 6$ is smaller than these two.) The dynamo is comprised of two terms in opposing directions. Breaking these down into the terms which dominate the spatial structure,

$$\begin{aligned}
\text{Dynamo} &= J_t B_r - J_r B_t \\
&\sim iJ_t - J_r \qquad (B_r \text{ and } B_t \text{ are relatively flat}) \\
&\sim i\frac{\partial}{\partial r}B_p - \frac{in}{R}B_p \qquad (B_r \text{ is small}) \\
&\sim \frac{\partial}{\partial r}B_p - B_p \qquad (\text{phase doesn't matter})
\end{aligned}$$

Looking at the Bp profiles in Figure C.2, it can be seen that the derivative peaks around r/a=.85, but always has the same sign. Adding this slightly peaked profile to an opposing term that is increasing in the core gives a pronounced peak in the total hall dynamo term, right on the reversal surface.

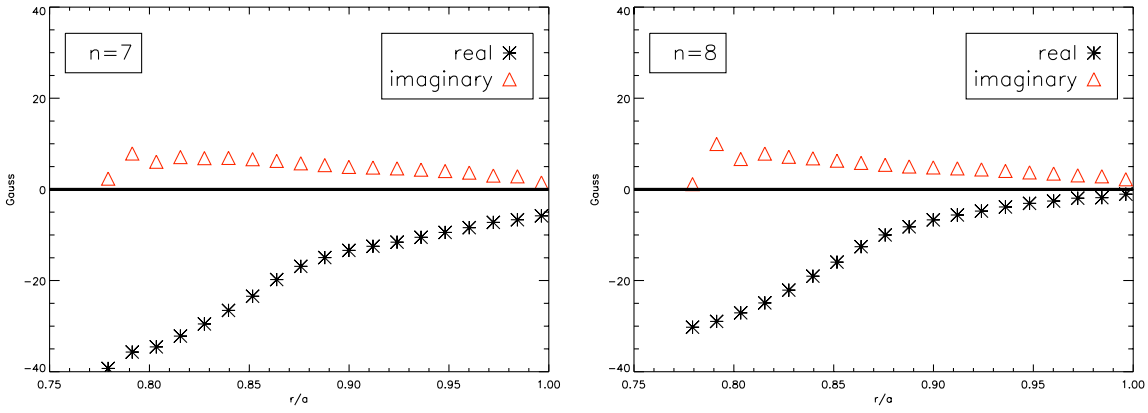

Figure C.2: Poloidal Field, B_θ

Appendix D: Full Bibliography

[1] Abdul Almagri and Hantao Ji. Sawteeth averaging procedure. Internal MST documentation, 1995.

[2] A.F. Almagri, S. Assadi, S.C. Prager, J.S. Sarff, and D.W. Kerst. Locked modes and magnetic field errors in the madison symmetric torus. *Phys. Fluids B*, 4(12):4080–4085, December 1992.

[3] Julius S. Bendat and Allan G. Piersol. *Random Data:Analysis and Measurement Procedures*. Wiley-Interscience, 3rd Edition, 2000.

[4] A. Bhattacharjee. Impulsive magnetic reconnection in the earth's magnetotail and solar corona. *Annu. Rev. Astron. and Astrophys.*, 42:365–384, 2004.

[5] J. Birn, J. E. Borovsky, and M. Hesse. Properties of asymmetric magnetic reconnection. *Phys. Plasmas*, 15(032101), 2008.

[6] J. Birn, J.F. Drake, M. A. Shay, B. N. Rogers, R. E. Denton, M. Hesse, M. Kuznetsova, Z.W. Ma, A. Bhattacharjee, A. Otto, and P.L. Pritchett. Gem magnetic reconnection challenge. *Journal of Geophysical Research*, 106(A3):3737–3750, March 2001.

[7] Dieter Biskamp. *Nonlinear Magnetohydrodynamics*. Cambridge University Press, 1993.

[8] H. A. B. Bodin and A. A. Newton. Reversed-field-pinch research. *Nuclear Fusion*, 20(10):1255–1324, 1980.

[9] A. H. Boozer. *Phys. Fluids*, 24(1999), 1981.

[10] D. L. Brower, W.X. Ding, S. D. Terry, J. K. Anderson, T. M. Biewer, B.E. Chapman, D. Craig, C.B. Forest, S. C. Prager, and J. S. Sarff. Measurement of the current-density profile and plasma dynamics in the reversed-field pinch. *Phys. Rev. Lett.*, 88(18):185005, May 2002.

[11] M.R. Brown, C.D. Cothran, and J. Fung. Two fluid effects on three-dimensional reconnection in the swarthmore spheromak experiment with comparisons to space data. *Phys. Plasmas*, 13(056503), 2006.

[12] P.A. Cassak and M. A. Shay. Scaling of asymmetric magnetic reconnection: General theory and collisional simulations. *Physics of Plasmas*, 14(102114), 2007.

[13] P.A. Cassak and M. A. Shay. Scaling of asymmetric hall magnetic reconnection. *Geophysical Research Letters*, 35(L19102), October 2008.

[14] B.E. Chapman, A. Almagri, M. Cekic, D.J.Den Hartog, S. C. Prager, and J.S. Sarff. Sawteeth and energy confinement in the madison symmetric torus reversed-field pinch. *Phys. Plasmas*, 3(3):709–711, March 1996.

[15] James Tharp Chapman. *Spectroscopic Measurements of the MHD Dynamo in the MST Reversed Field Pinch.* PhD thesis, September 1998. pp. 100 - 127.

[16] Seung-Ho Choi. *Origin of Tearing Mode Excitation in the MST Reversed Field Pinch.* PhD thesis, University of Wisconsin-Madison, 2006.

[17] Seung-Ho Choi, D. Craig, F. Ebrahimi, and S. C. Prager. Cause of sudden magnetic reconnection in a laboratory plasma. *Phys. Rev. Lett.*, 96(145004), 2006.

[18] J. W. Conner, S.C. Cowley, R. J. Hastie, T. C. Hender, A. Hood, and T. J. Martin. Tearing modes in toroidal geometry. *Phys. Fluids*, 31(3):577, 1988.

[19] Steve Cowley. Frozen field lines and diffusion. CMSO/CMPD Winter School notes, January 2006.

[20] D. Craig. User's guide to sawtooth ensemble routines. Internal MST documentation, 2002.

[21] D. Craig. Magnetic mode analysis in mst. Internal MST documentation, 2005.

[22] N. A. Crocker, G. Fiksel, S. C. Prager, and J. S. Sarff. Measurement of the current sheet during magnetic reconnection in a toroidal plasma. *Phys. Rev. Lett.*, 90(3):035003, January 2003.

[23] W. Daughton, V. Roytershteyn, B. J. Albright, H. Karimabadi, L. Yin, and Kevin J. Bowers. Transition from collisional to kinetic regimes in large-scale reconnection layers. *Physical Review Letters*, 103(065004), August 2009.

[24] R. N. Dexter, D. W. Kerst, T. W. Lovell, and S. C. Prager. The madison symmetric torus. *Fusion Technology*, 19:131–139, January 1991.

[25] W.X. Ding, D. L. Brower, D. Craig, B.H. Deng, G. Fiksel, V. Mirnov, S. C. Prager, J. S. Sarff, and V. Svidzinski. Measurement of the hall dynamo effect during magnetic reconnection in a high-temperature plasma. *Phys. Rev. Lett.*, 93(4):045002, July 2004.

[26] F. Ebrahimi, V.V. Mirnov, and S.C. Prager. Momentum transport from tearing modes with shear flow. *Phys. Plasmas*, (15):055701, 2008.

[27] Paul W. Fontana. *Ion Dynamics and the Dynamo in the Edge of the Reversed-Field Pinch*. PhD thesis, University of Wisconsin-Madison, 1999.

[28] P.W. Fontana, D.J.Den Hartog, G. Fiksel, and S. C. Prager. Spectroscopic observation of fluctuation-induced dynamo in the edge of the reversed-field pinch. *Phys. Rev. Lett.*, 85(3):566–569, July 2000.

[29] H. Furth, J. Killeen, and M. Rosenbluth. Finite resistivity instabilities of a sheet pinch. *The Physics of Fluids*, 6(4):459–484, April 1963.

[30] R. G. Giovanelli. A theory of chromospheric flares. *Nature*, 158:81–82, July 1946.

[31] D.J.Den Hartog, J.T. Chapman, D. Craig, G. Fiksel, P.W. Fontana, S. C. Prager, and J. S. Sarff. Measurements of core velocity fluctuations and the dynamo in a reversed-field pinch. *Physics of Plasmas*, 6(5):1813–1821, May 1999.

[32] Y. L. Ho and G. G. Craddock. Nonlinear dynamics of field maintenance and quasiperiodic relaxation in reversed-field pinches. *Physics of Fluids B: Plasma Physics*, 3(3):721–734, 1991.

[33] S. Hokin et al. Global confinement and discrete dynamo activity in the mst reversed-field pinch. *Phys. Fluids B*, 3(8):2241–2246, August 1991.

[34] S. Hokin et al. Reversed-field pinch studies in the madison symmetric torus. *Journal of Fusion Energy*, 12(3):281–287, 1993.

[35] R.B. Howell, J.C. Ingraham, G.A. Wurden, P.G. Weber, and C.J. Buchenauer. Asymmetric magnetic flux generation, m=1 activity, and edge phenomena on a reversed-field pinch. *Phys. Fluids*, 30(6):1828–1838, June 1987.

[36] I. H. Hutchinson. *Principles of Plasma Diagnostics*. Cambridge University Press, 2 edition, 2002.

[37] T.P. Intrator, X. Sun, G. Lapenta, and I. Furno. Experimental onset threshold and magnetic pressure pile-up for 3d reconnection. *Nature Physics*, May 2009.

[38] John David Jackson. *Classical Electrodynamics*. John Wiley and Sons Inc, 3 edition, 1999.

[39] H. Ji, S.C. Prager, and J.S. Sarff. Conservation of magnetic helicity during plasma relaxation. *Phys. Rev. Lett.*, 74(15):2945–2948, April 1995.

[40] Hantao Ji, Masaaki Yamada, Scott Hsu, and Russel Kulsrud. Experimental test of the sweet-parker model of magnetic reconnection. *Phys. Rev. Lett.*, 80(15):3256–3259, April 1998.

[41] Young C. Kim and Edward J. Powers. Digital bispectral analysis and its applications to nonlinear wave interactions. *IEEE Transactions on Plasma Science*, PS-7(2):120, June 1979.

[42] Jacob King. Numerical studies of two-fluid tearing and dynamo in a cylindrical pinch. *Bull. Am. Phys. Soc.*, 54(15):TP8.71, November 2009.

[43] A. Kuritsyn, D. Craig, G. Fiksel, Matt Miller, D. Cyliner, and Masaaki Yamada. Local measurements of plasma ion dynamics with optical probes. *Rev. Sci. Instr.*, 77(10F112), 2006.

[44] A. Kuritsyn, G. Fiksel, A.F. Almagri, S.C. Prager, J. S. Sarff, and T.D. Tharp. Measurements of the hall dynamo in the reversed field pinch edge during reconnection events. *16th IEEE International Pulsed Power Conference*, 1:20–23, 2007.

[45] N.F. Loureiro, A.A. Schekochihin, and S. C. Cowley. Instability of current sheets and formation of plasmoid chains. *Phys. Plasmas*, 14(100703), 2007.

[46] Leonid Malyshkin, Timur Linde, and Russel Kulsrud. Magnetic reconnection with anamalous resistivity in tow-and-a-half dimensions. 1. quasistationary case. *Phys. Plasmas*, 12(102902), 2005.

[47] V.V. Mirnov, C.C. Hegna, S.C. Prager, C.R. Sovinec, and H. Tian. Two fluid dynamo and edge-resonant m=0 tearing instability in reversed field pinch. *Proc. of the 21th IAEA Fusion Energy Conference (IAEA-CN-149)*, TH:3–18, 2006.

[48] Dwight R. Nicholson. *Introduction to Plasma Theory.* John Wiley and Sons Inc, 1983.

[49] S. Ortolani and D. D. Schnack. *Magnetohydrodynamics of Plasma Relaxation.* World Scientific, Singapore, 1993.

[50] E. N. Parker. Sweet's mechanism for merging magnetic fields in conducting fluids. *J. Geophys. Res.*, 62(4):509–520, December 1957.

[51] P. Piovesan, A. Almagri, B.E. Chapman, D. Craig, L. Marrelli, P. Martin, S.C. Prager, and J.S. Sarff. Filamentary structures observed in the madison symmetric torus with extended arrays of fast magnetic probes. *Nuclear Fusion*, 48(095003), September 2008.

[52] S.C. Prager, A. Almagri, M. Cekic, J. Chapman, D.J.Den Hartog, G. Fiksel, C. Hegna, H. Ji, J.S. Sarff, J.R. Drake, S. Mazur, P. Nordlund, and H.E.Saetherblom. Plasma rotation, dynamo, and nonlinear coupling in the reversed-field pinch. *Plasma Phys. Control. Fusion*, 37:A303–A311, 1995.

[53] S.C. Prager, A.F. Almagri, S. Assadi, J.A. Beckstead, R. N. Dexter, D.J.Den Hartog, G. Chartas, S.A. Hokin, T.W. Lovell, T.D. Rempel, J.S. Sarff, W. Shen, C.W. Spragins, and J.C. Sprott. First results from the madison symmetric torus reversed field pinch. *Phys. Fluids B*, 2(6):1367–1371, June 1989.

[54] T.D. Rempel, C.W. Spragins, S. C. Prager, S. Assadi, D.J.Den Hartog, and S. Hokin. Edge electrostatic fluctuations and transport in a reversed-field pinch. *Phys. Rev. Lett.*, 67(11):1438–1441, September 1991.

[55] Yang Ren, Masaaki Yamada, Stefan Gerhardt, Hantao Ji, Russell Kulsrud, and Aleksey Kuritsyn. Experimental verification of the hall effect during magnetic reconnection in a laboratory plasma. *Phys. Rev. Lett.*, (95):055003, 2005.

[56] Ch. P. Ritz, E. J. Powers, and R. D. Bengtson. Experimental measurement of three-wave coupling and energy cascading. *Phys. Fluids B*, 1(1):153–163, January 1989.

[57] J. S. Sarff, S. A. Hokin, H. Ji, S.C. Prager, and C. R. Sovinec. Fluctuation and transport reduction in a reversed field pinch by inductive poloidal current drive. *Phys. Rev. Lett.*, 72(23):3670–3673, June 1994.

[58] John S. Sarff. Nonlinear coupling of tearing fluctuations in the madison symmetric torus. *Phys. Fluids B*, 5(2540), 1993.

[59] J.S. Sarff et al. Transport reduction by current profile control in the reversed-field pinch. *Phys. Plasmas*, 2(6):2440–2446, June 1995.

[60] D. D. Schnack et al. *Computer Physics Communications*, 43(17), 1986.

[61] G. Serianni, A. Murari, G. Fiksel, V. Antoni, M. Bagatin, D. Desideri, E. Martines, and L. Tramontin. Magnetic fluctuations and energy transport in rfx. *Plasma Phys. Control. Fusion*, (43):919–927, 2001.

[62] W. Shen, R. N. Dexter, and S.C. Prager. Current-density fluctuations and ambipolarity of transport. *Phys. Rev. Lett.*, 68(9):1319–1322, March 1992.

[63] W. Shen and S.C. Prager. The fluctuation-induced hall effect. *Phys. Fluids B*, 5(7):1931–1933, July 1993.

[64] Earl Skime et al. Ion heating and magnetohydrodynamic dynamo fluctuations in the reversed-field pinch. *Phys. Fluids B*, 4(12):4062–4071, 1992.

[65] C. R. Sovinec et al. Nonlinear magnetohydrodynamics simulation using high-order finite elements. *Journal of Computational Physics*, 195(355), 2004.

[66] R.L. Stenzel. A new probe for measuring small electric fields in plasmas. *Rev. Sci. Instr.*, 62(1):130–139, 1991.

[67] R.L. Stenzel, W. Gekelman, and N. Wild. Magnetic field line reconnection experiments 4. resistivity, heating, and energy flow. *Journal of Geophysical Research*, 87(1):111–117, January 1982.

[68] Curt Suplee. *The Plasma Universe*. Cambridge University Press, 2009.

[69] V. A. Svidzinski, G. Fiksel, V. V. Mirnov, and S. C. Prager. Modeling of ion heating from viscous damping of reconnection flows in the rfp. *Phys. Plasmas*, 15(062511), 2008.

[70] P.A. Sweet. Electromagnetic phenomena in cosmical physics. *International Astronomical Union Symposium*, 6, 1958.

[71] P.A. Sweet. Mechanisms of solar flares. *Annu. Rev. Astron. and Astrophys.*, 7:149–176, 1969.

[72] John R. Taylor. *An Introduction to Error Analysis*. University Science Books, 2 edition, 1997.

[73] Vytenis M. Vasyliunas. Theoretical models of magnetic field line merging, 1. *Reviews of Geophysics and Space Physics*, 13(1):303–336, February 1975.

[74] N. Vianello, E. Martines, et al. Transport mechanisms in the outer region of rfx-mod. *Nuclear Fusion*, 49(4):045008, 2009.

[75] S. von Goeler, W. Stodiek, and N. Sauthoff. Studies of internal disruptions and m=1 oscillations in tokamak discharges with soft-x-ray techniques. *Phys. Rev. Lett.*, 33(20):1201–1203, November 1974.

[76] R. G. Watt and E.M. Little. Rfp energy evolution and containment in the presence of giant sawteeth. *Phys. Fluids*, 27(4):784–786, April 1984.

[77] R. G. Watt and R. A. Nebel. Sawteeth, magnetic disturbances, and magnetic flux regeneration in the reversed-field pinch. *Phys. Fluids*, 26(5):1168–1170, May 1983.

[78] K.A. Werley, R. A. Nebel, and G.A. Wurden. Transport description of the rise time of sawtooth oscillations in reversed-field pinches. *Phys. Fluids*, 28(5):1450–1453, May 1985.

[79] G.A. Wurden. Soft x-ray array results on the zt-40m reversed-field pinch. *Phys. Fluids*, 27(3):551–554, March 1984.

[80] Masaaki Yamada. Progress in understanding magnetic reconnection in laboratory and space astrophysical plasmas. *Physics of Plasmas*, 14(058102), 2007.

[81] Masaaki Yamada, Hantao Ji, Scott Hsu, Troy Carter, Russel Kulsrud, and Fedor Trintchouk. Experimental investigation of the neutral sheet profie during magnetic reconnection. *Physics of Plasmas*, 7(5):1781–1787, May 2000.

[82] Masaaki Yamada, Russel Kulsrud, and Hantao Ji. Magnetic reconnection. Technical Report PPPL-4457, PPPL, June 2009.

[83] Paolo Zanca and David Terranova. Reconstruction of the magnetic perturbation in a toroidal reversed field pinch. *Plasma Phys. Control. Fusion*, 46:1115–1141, 2004.

[84] Ellen G. Zweibel and Masaaki Yamada. Magnetic reconnection in astrophysical and laboratory plasmas. *Annu. Rev. Astron. and Astrophys.*, 47:291–332, 2009.